

**Characterization of the Boundary Diffusion Mechanism
for the Helix-Coil Transition in Peptides by
Triplet-Triplet Energy Transfer**

Dissertation
zur Erlangung des
Doktorgrades der Naturwissenschaften (Dr. rer. nat.)

der

Naturwissenschaftlichen Fakultät I – Biowissenschaften –

der Martin-Luther-Universität
Halle-Wittenberg,

vorgelegt

von Herrn Stefan Wicht

geboren am 08.08.1985 in Berlin

Erstgutachter: Prof. Dr. Thomas Kiefhaber
Zweitgutachter: Prof. Dr. Mike Schutkowski
Drittgutachter: Prof. Dr. Ralf Seidel

Tag der öffentlichen Verteidigung: 04. März 2019

Table of Content

Symbols and Abbreviations	3
1 Introduction.....	5
1.1 Protein Folding	5
1.1.1 The Unfolded and the Native State	5
1.1.2 Thermodynamics of Protein Folding.....	8
1.1.3 Kinetics of Protein Folding	11
1.1.4 Frictional Effects in Protein Folding.....	15
1.2 α -Helices.....	18
1.2.1 α -Helix Stability	19
1.2.2 The Helix-Dipole and Capping Motifs.....	21
1.2.3 Statistical Mechanical Models of the Helix-Coil Transition.....	22
1.2.4 Dynamics of the Helix-Coil Transition.....	25
1.3 Triplet-Triplet Energy Transfer (TTET).....	27
1.3.1 TTET in Unfolded Polypeptides	29
1.3.2 TTET in Folded Peptides and Proteins.....	31
2 Aim of Research.....	39
3 Materials and Methods.....	41
3.1 Peptide Synthesis and Purification	41
3.2 Peptide Modifications	42
3.3 Sample Preparation and Concentration Determination	42
3.4 Laser Flash Photolysis	43
3.5 Circular Dichroism Spectroscopy.....	44
3.6 Determination of the Average Position of the Helix-Coil Boundary	44
4 Results and Discussion	47
4.1 Determination of the Diffusion Coefficient for Boundary Diffusion in α -Helices .	47
4.1.1 Effect of the Diffusion Distance on the Diffusion Coefficient for Boundary Diffusion.....	47
4.1.2 Effect of Peptide Length on Helix Folding and Unfolding Dynamics with $i,i+2$ Spacing	50
4.1.3 Comparison of the Diffusion Coefficient for Boundary Diffusion with $i,i+2$ and $i,i+6$ Spacing.....	56
4.2 Energetics of the Boundary Diffusion Mechanism	59
4.2.1 Effect of Solvent Viscosity on Boundary Diffusion.....	59

4.2.2	Effect of Temperature on Boundary Diffusion.....	67
4.2.3	Internal and Solvent Friction in Boundary Diffusion.....	75
4.3	Characterization of the Third Kinetic Phase.....	77
4.4	Effect of Capping Motifs on Boundary Diffusion.....	79
4.4.1	Effect of Capping Motifs on Stability and Dynamics in the Helix Center.....	79
4.4.2	Effect of Capping Motifs on the Diffusion Coefficient for Boundary Diffusion	83
4.4.3	Effect of Capping Motifs on the Diffusion Distance from the Helix-Coil Boundary to the Helix Center.....	89
4.4.4	Effect of Capping Motifs on the Activation Energy for Boundary Diffusion..	93
4.4.5	Contribution from Charges to the Effect of Capping Motifs on Helix Stability	99
5	Summary and Outlook.....	103
6	Appendix.....	107
7	References.....	119
8	Acknowledgement.....	139
9	Curriculum Vitae.....	141
10	Eidesstattliche Erklärung.....	143

Symbols and Abbreviations

% (v/v)	volume percent
% (w/v)	weight per volume percent
α	exponent of the solvent viscosity dependence $\eta^{-\alpha}$
η	solvent viscosity
k_B	Boltzmann constant
R	universal gas constant
$\langle l^2 \rangle$	squared average diffusion distance
T	absolute temperature
aa	amino acids
Ac	N-terminal acetyl group
Ac ₂ O	acetic anhydride
ACN	acetonitrile
Aea	C-terminal 2-aminoethylamide group
CD	circular dichroism
CO	peptide backbone carbonyl group
EDA	ethylenediamine
D	diffusion coefficient
DBU	1,8-diazabicyclo(5.4.0)undec-7-ene
DCM	dichloromethane
DIPEA	<i>N,N</i> -diisopropylethylamine
DMF	<i>N,N</i> -dimethylformamide
DMSO	dimethyl sulfoxide
Dpr	α,β -L-diaminopropionic acid
E_a	activation energy
ESI	electrospray ionization
<i>et al.</i>	et altera
f_{int}	internal friction
Fmoc	fluorenylmethoxycarbonyl
FMP	4-formyl-3-methoxy phenoxyethyl
FRET	förster resonance energy transfer
f_{solv}	solvent friction
GdmCl	guanidinium chloride
H-bond	hydrogen bond

HBTU	2-(1H-benzotriazole-1-yl)- <i>N,N,N',N'</i> -tetramethyluronium hexafluorophosphate
HPLC	high performance liquid chromatography
IDP	intrinsically disordered protein
ISC	intersystem crossing
LR	Lifson-Roig
MALDI-TOF	matrix-assisted laser desorption ionization-time of flight
MC	Monte Carlo
MD	molecular dynamics
Mtt	<i>N</i> -methyltrityl
N	native state
NaCl	sodium chloride
Nal	naphthalene or 1-L-naphthylalanine
NH	peptide backbone amine group
NH ₂	C-terminal amide group
NH ₃ ⁺	free, positively charged N-terminus
NMM	<i>N</i> -methylmorpholine
NMP	<i>N</i> -methyl-2-pyrrolidon
NMR	nuclear magnetic resonance
RAM	rink amide
REFERs	rate equilibrium free energy relationships
SASA	solvent accessible surface area
Suc	N-terminal succinyl group
TFA	trifluoroacetic acid
TIPS	triisopropylsilane
TTET	triplet-triplet energy transfer
TS	transition state
TST	transition state theory
U	unfolded state
UV	ultraviolet
Vis	visual
Xan	xanthone or 9-Oxoxanthen-2-carboxylic acid

1 Introduction

1.1 Protein Folding

Proteins are the most abundant and diverse class of biomolecules found in living cells. They are essential for the structural stability of the cell but also participate in a wide variety of cellular processes including metabolism, DNA replication, transcription and translation as well as signaling and transport. Proteins are linear polymers of amino acids linked by amide bonds, which is usually termed as peptide bond. The amino acid sequence of proteins is genetically encoded. There are 21 different α -L-amino acids with a similar composition of the backbone but distinct side chains of different properties and reactivities. *In vivo*, proteins are synthesized at the ribosome. In higher organisms, proteins can be post-translationally modified with sugars, lipids or other chemical groups leading to a diversified function and regulation (1).

In order to fulfill the required function, proteins have to adopt a well-defined three-dimensional structure. The transition from an unstructured polypeptide chain (unfolded state) to a highly ordered molecule with a specific three-dimensional structure (native state) is referred to as protein folding. The structure of proteins in solution is fully encoded in their amino acid sequence and is stabilized by several non-covalent interactions (2). Protein folding occurs spontaneously during translation or can be assisted by isomerases and chaperones (3-5). However, a significant fraction of proteins are intrinsically disordered (IDP) and lack a well-defined structure under physiological conditions. In these proteins, structure formation is mostly coupled to ligand binding (6, 7). In contrast, systematic misfolding and aggregation of proteins is related to a number of neurodegenerative diseases like Alzheimer's and Parkinson's disease (8, 9).

1.1.1 The Unfolded and the Native State

The unfolded state (U) of proteins is difficult to characterize as it is heterogeneous in conformation and rarely populated under physiological conditions. Low pH, high temperature and pressure or denaturants can be used to populate the unfolded state (Eq. 1.3). However, the unfolded state might be sensitive towards these perturbations and is not equivalent to an unfolded protein in water.

The unfolded state plays a crucial role in the folding process since it serves as the starting point of the folding reaction. Moreover, the stability of the native structure is quantified relative to the unfolded state and thus represents a reference state (10, 11). The unfolded

state of a protein comprises a large ensemble of different conformations, which rapidly interconvert through temperature driven Brownian motion (12). Starting from this ensemble of unfolded conformations a polypeptide chain has to search for energetically favorable interactions in order to reach the native state (N). The rate at which a folding polypeptide chain can explore conformational space is limited by intrachain diffusion processes, i.e. interaction of two points along the chain (13, 14). The configurational properties of the unfolded state influence intrachain diffusion and thus the folding speed. The simplest description of the unfolded state of a protein is the idealized view of a random coil (15-17). In a random coil no specific interactions between residues or chain segments persist and a large conformational space is populated (freely jointed chain) (18, 19). However, folding from a random coil is very improbable as it takes an enormously long time (Levinthal's paradox) and additionally is energetically unfavorable because of the high entropy cost (20).

It is now widely accepted that the description of the unfolded state as a complete random coil is not accurate. In polypeptide chains, neighboring segments influence each other and restrict torsional backbone angles by steric repulsions leading to a reduction of conformationally allowed space. These torsional potentials are captured by the well-known Ramachandran map (21, 22) (Fig. 1.1). In this plot only a broad β -region and the α -regions are sterically allowed. In addition, it has been shown that local steric effects in polypeptides extend beyond nearest-neighbor interactions leading to a significantly restricted conformational space for the unfolded state compared to a dipeptide (23). Adding hydrogen bonding constraints to these steric restrictions in the Ramachandran plot eliminates another substantial region of backbone conformations in the unfolded state (24) (Fig. 1.1). Moreover, there is evidence for a conformational bias in the unfolded state to some secondary structural elements (25-29). The observed residual structure ranges from local secondary structure propensities to persisting hydrophobic clusters with native-like or non-native like topology. Previous studies proposed that poly-proline II (PPII) helices contribute substantially to unfolded populations for a variety of systems including homopolymers, peptide fragments and proteins (30-35). A theoretical approach has also shown, that an energy bias against unfavorable conformations in the unfolded state can reduce folding times down to observed values (36).

Thus, most conceivable states are inaccessible in the unfolded state, which reduce the effective conformational space and promotes organization in unfolded proteins. This in

turn reduces the conformational entropy in the unfolded state and makes folding to the native structure more favorable.

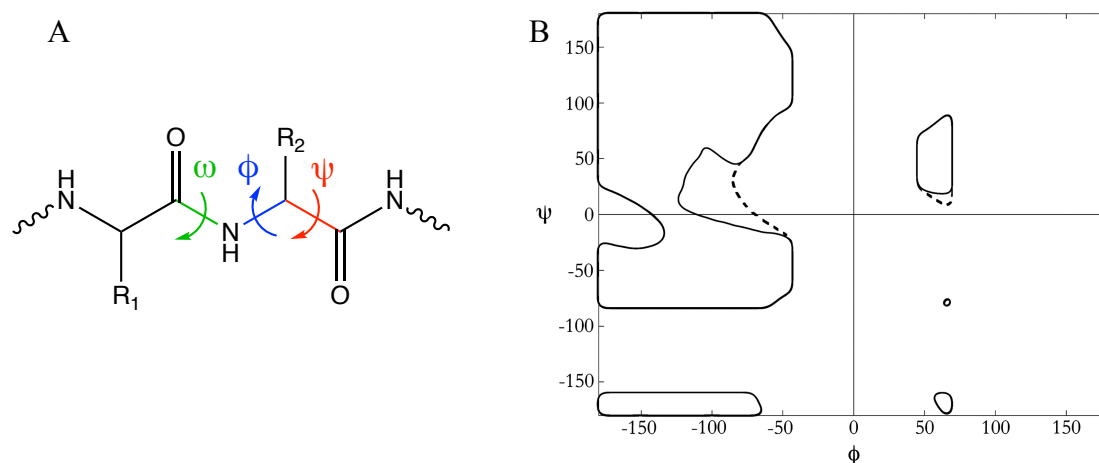


Figure 1.1: Sterically allowed peptide backbone conformations. (A) Peptide backbone dihedral angles ϕ , ψ and ω . Due to the planarity of the peptide bond, ω is restricted to 180° (*trans*) and 0° (*cis*). (B) Ramachandran plot of an alanine dipeptide. Sterically allowed regions are located within the dashed lines. The β -region is in the top left quadrant and is connected to the α -region (right-handed) over a bridge. The bridge region is restricted when hydrogen bonding constraints are taken into account (solid line). Figure adapted from Porter & Rose (24).

The native state (N) is the preferred state of a protein under physiological conditions with a specific three-dimensional structure. The structure is related to a unique cellular function of the respective protein although in some functionally active proteins a well-defined structure is lacking under physiological conditions and structure formation is coupled to ligand binding. The advantage of intrinsically disordered proteins (IDPs) might be the capacity to bind multiple partners and to fold into alternative conformations (7, 37-40). However, results also demonstrated a dynamic heterogeneity in the native state of proteins clarifying that the structure of proteins does not have a rigid topology. The conformational dynamics in the native state are of fundamental importance for protein folding and function and range from small thermal fluctuations in the picoseconds to femtoseconds time range to global motions of whole domains on the microseconds to milliseconds timescale (41-45).

The structure of proteins is a complex interplay of different non-covalent interactions and the overall stability is rather small due to compensating stabilizing and destabilizing energetic contributions within the protein or between protein and solvent. The native state can be divided into four levels of organization. The primary structure is simply the linear amino acid sequence without any three-dimensional structure. Upon folding, secondary

structural elements are formed locally and in absence of tertiary interactions, which are mainly stabilized by intramolecular backbone hydrogen bonds or local side chain interactions to compensate the enthalpy loss of protein-solvent interactions (46). Common types of secondary structure are α -helices, β -sheets and turns. Pauling postulated these secondary structures simply by considering a maximum number of internal satisfied backbone hydrogen bonds and steric effects (47, 48). The three-dimensional arrangement of different secondary structural elements stabilized by short-range and long-range interactions such as electrostatic interactions, *van-der-Waals* interactions, hydrogen bonds and the hydrophobic effect is referred to as the tertiary structure (49-52). The hydrophobic effect is a significant driving force for protein folding since it minimizes the entropy loss of ordered water molecules around hydrophobic groups (formation of hydration shell) upon burial and partially compensates the loss in conformational entropy upon folding (49, 52). The tertiary structure represents the basic unit of proteins and can be divided into different domains with a hydrophobic core and a hydrophilic surface each. Domains are stable and autonomously folding units of the tertiary structure. However, the majority of proteins in higher organisms are oligomeric, multi-domain proteins (53). Such proteins are composed of several identical (homo) or non-identical (hetero) tertiary structures (monomers), which is referred to as the quaternary structure of a protein.

1.1.2 Thermodynamics of Protein Folding

Most small, single-domain proteins exhibit a simple two-state transition between a fully folded, native state (N) and a fully unfolded state (U) separated by a free-energy barrier (Eq. 1.1, Fig. 1.2). This implies a fully reversible reaction with a single cooperative transition between U and N and intermediates are not populated at equilibrium (54).



U and N represent equilibrium distributions of many conformational states that rapidly equilibrate prior to complete folding (k_f) or unfolding (k_u). Thus, both conformational ensembles and especially the broad unfolded state ensemble can be considered as thermodynamic states (55, 56). The relative concentrations of N and U reveal the equilibrium constant K_{eq} which relates the difference in the Gibbs free energy (ΔG^0) between the two states (Eq. 1.2).

$$\Delta G^0 = -RT \cdot \ln K_{eq} = \Delta H^0 - T\Delta S^0 \text{ with } K_{eq} = \frac{[N]_{eq}}{[U]_{eq}} = \frac{k_f}{k_u} \quad (1.2)$$

The native state of a protein in water is the most stable conformation with the deepest global minimum in free energy relative to the unfolded state (Fig. 1.2) (2). Exceptions represent intrinsically disordered proteins (IDPs) and aggregated proteins such as prion proteins (8). The thermodynamic stability of a protein is a result of compensating stabilizing and destabilizing effects in entropy and enthalpy. Consequently, the overall stability of the native state is rather small between -10 to -60 kJ mol⁻¹ (57). Thus, protein stability can be easily affected by different perturbations. According to the Gibbs fundamental equation, folding equilibria can be perturbed by a change in pressure p , temperature T or solvent composition n (Eq. 1.3).

$$d\Delta G^0 = \Delta V^0 dp - \Delta S^0 dT + \sum_i \Delta\mu_i^0 dn_i \quad (1.3)$$

Each perturbation gives information on different thermodynamic parameters of the system. A change in pressure enables a direct measurement of the reaction volume ΔV^0 between U and N whereas a variation in temperature yields information about the reaction entropy ΔS^0 and reaction enthalpy ΔH^0 according to van't Hoff (Eq. 1.4).

$$\frac{d \ln K_{eq}}{d1/T} = -\frac{\Delta H_{v.H}^0}{R} \quad (1.4)$$

ΔS^0 and ΔH^0 are temperature-dependent because the unfolded state has a larger heat capacity than the folded state ($\Delta C_p^0 \neq 0$) (54). This is because buried hydrophobic side chains in the folded state are solvent exposed in the unfolded state (58). Consequently, the stability of a protein has a maximum at a certain temperature and both heat and cold denaturation can occur. Adding destabilizing or stabilizing co-solutes such as urea, guanidinium chloride (GdmCl) or sarcosin and trimethylamine N-oxid (TMAO) changes the chemical potential $\Delta\mu^0$. Denaturants (urea, GdmCl) shift the equilibrium towards U whereas stabilizing co-solutes (TMAO, glycerol) shift the equilibrium towards N. The molecular mechanism of this effect is still not well understood. But it is suggested that

denaturants unfold proteins by either improving the solvation of the polypeptide chain (good solvent) (15, 17, 59, 60) or direct binding (61-64). In contrast, it is assumed that stabilizing co-solutes stabilize proteins by preferential hydration and exclusion from the protein surface (bad solvent) (65, 66). The resulting change in ΔG^0 with the molar concentration $[C]$ is linearly related (61, 67, 68) and simplifies equation 1.3 to

$$d\Delta G^0 = \Delta V^0 dp - \Delta S^0 dT + m_{eq} d[C]. \quad (1.5)$$

Adding denaturants provides information on the change in solvent accessible surface area ($\Delta SASA$) upon unfolding, since the m_{eq} -value directly correlates with the difference in solvent accessible surface area between U and N (Fig. 1.2) (69).

However, a two-state folding mechanism as discussed above might be an oversimplification for small, single-domain proteins but gives good estimates.

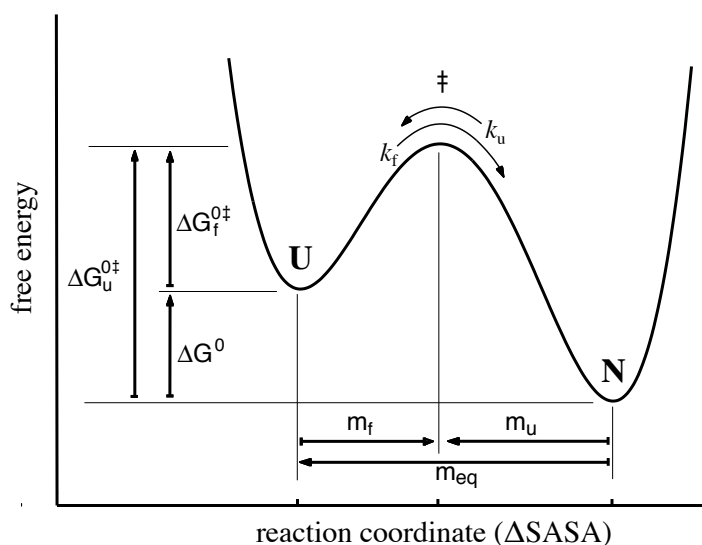


Figure 1.2: Free energy profile for a two-state protein folding reaction. The ground states U and N are separated by a free energy barrier with the transition state (TS) as the highest point in free energy. The activation free energies for passing the barrier from U or N, $\Delta G_f^{0‡}$ and $\Delta G_u^{0‡}$, respectively, are reflected in the microscopic rate constants k_f or k_u (Eq. 1.7). The sensitivity of the reactions to changes in denaturant concentration is reflected by the proportionality constants, m_u and m_f , respectively (Eq. 1.20). The kinetic m -values are believed to reflect the changes in solvent accessible surface area ($\Delta SASA$) between U and TS (m_f) and N and TS (m_u), since the m_{eq} -values were shown to be proportional to $\Delta SASA$ upon unfolding (69). Figure taken from (70).

1.1.3 Kinetics of Protein Folding

Protein folding from the unfolded state ensemble to the native state by a random search of the conformational space would take an astronomical amount of time (20). Nevertheless, proteins can fold in seconds or less because of an energy bias towards unfavorable conformations in the unfolded state (36). Moreover, it has been shown that transient high-energy intermediates exist in apparent two-state folders and accelerate folding reactions by further constraining the conformational space (71-73).

Protein folding reactions are extremely heterogeneous and occur on different time scales ranging from microseconds up to several seconds or hours and involve various degrees of motions (43, 57, 74-76). Local bond or side chain rotations occur within picoseconds, loop motions on the nanoseconds timescale and large-scale motions of whole domains in the microseconds time range (13, 14, 77-79). Rate-limiting steps such as prolyl *cis-trans* isomerization or disulfide bridge formation slow down protein folding reactions significantly and can lead to complex folding kinetics (3, 80, 81).

In the simplest case, for small proteins which fold according to a two-state model, the folded and unfolded states are separated by a high free energy transition state (TS) located on the barrier top (Fig. 1.2). The transition state represents the rate-limiting step in the folding reaction and knowledge about its structure and energetics is essential for understanding protein folding. The kinetics of two-state folders can be described by a reversible first order reaction with one experimentally observed rate constant λ (Eq. 1.6). The apparent rate constant λ is given by the sum of the folding (k_f) and unfolding (k_u) rate constants.

$$\lambda = k_f + k_u \quad (1.6)$$

Typically, the logarithm of k_f and k_u depend linearly on denaturant concentration $[D]$ ($m_{f,u} = \partial \Delta G^{0\ddagger} / \partial [D]$) (17). Thus, the microscopic rate constants for folding and unfolding can be determined with a denaturant dependence of unfolding and refolding reactions in a chevron plot ($\ln(\lambda)$ vs. $[denaturant]$) by extrapolating both folding and unfolding limbs to zero denaturant (15). The free energy for folding ΔG^0 can be determined from the equilibrium constant K_{eq} by using the folding and unfolding rate constants (Eq. 1.2). Thus, an apparent two-state folding mechanism can be confirmed when thermodynamic and kinetic data yield similar free energies (ΔG^0) (82).

When a reversible two-state assumption is valid, the transition state theory (TST) of Eyring and Evans and Polanyi can be applied in order to obtain information on the energy landscape of the folding and unfolding reaction (83, 84). In the Eyring formalism a reaction rate depends on the height of the free energy barrier ($\Delta G^{0\dagger}$) between the transition state and the ground states and on the pre-exponential factor k_0 (Eq. 1.7) (Fig. 1.2).

$$k = k_0 \cdot e^{-\Delta G^{0\dagger}/RT} = k_0 \cdot e^{\Delta S^{0\dagger}/R} \cdot e^{-\Delta H^{0\dagger}/RT} \quad (1.7)$$

The pre-exponential factor k_0 is the maximum rate constant for a reaction in absence of any free energy barriers and is specific for each reaction. The proper treatment of the pre-exponential factor is a central question in protein folding and chemical physics to obtain accurate values for ΔG^0 and $\Delta G^{0\dagger}$ (Eq. 1.2, Eq. 1.7). Originally, k_0 reflects the frequency of a single bond vibration where κ represents the transmission coefficient and h is the Planck constant (Eq. 1.8) (82-84).

$$k_0 = \kappa \frac{k_B T}{h} \approx 6 \cdot 10^{12} \text{ s}^{-1} \text{ at } 25^\circ\text{C} \quad (1.8)$$

However, the Eyring pre-exponential factor k_0 is not an appropriate description for protein folding reactions since it is based on the formation or breakage of covalent interactions in the gas phase. In contrast, protein folding involves changes of many weak, non-covalent interactions in solution and is limited by intrachain diffusion processes. Intrachain diffusion represents the first basic step during protein folding and is the maximum rate at which two points in a polymer chain can make contact. Intrachain diffusion is specific for a particular protein and depends on the amino acid sequence and the position within the chain. This value was recently determined and is in the order of $10^7 - 10^8 \text{ s}^{-1}$ (13, 14, 78, 85).

Smoluchowski could show that diffusion sets the upper limit for bimolecular reactions in solution. Here, the pre-exponential factor depends on the sum of the individual diffusion coefficients D and contact radii R between the reacting molecules and is in the range of $5 \cdot 10^9 \text{ M}^{-1} \text{ s}^{-1}$ (Eq.1.9) (86).

$$k_0 = 4\pi DR \approx 5 \cdot 10^9 \text{ M}^{-1} \text{ s}^{-1} \text{ at } 25^\circ \text{C} \quad (1.9)$$

However, the Smoluchowski limit was derived for reacting molecules with isotropic reactivity and is not realistic for reactions with orientational constraints.

On the other hand, when the pre-exponential factor is completely unknown the empirical van't Hoff-Arrhenius law can be applied to obtain information on the barrier height (Eq. 1.10).

$$k = A \cdot e^{-E_a/RT} \quad (1.10)$$

Here, E_a is the activation energy and A the pre-exponential factor which depends on the maximum rate constant for the elementary reaction k_0 and on an entropic contribution $\Delta S^{0\dagger}$ (Eq. 1.11). The activation energy E_a is almost identical to the enthalpy of activation $\Delta H^{0\dagger}$ with a small contribution from the thermal energy RT .

$$A = k_0 \cdot e^{(\Delta S^{0\dagger} + R)/R} \quad \text{and} \quad E_a = \Delta H^{0\dagger} + RT \quad (1.11)$$

The properties of transition barriers can be analyzed by using rate equilibrium free energy relationships (REFERs) (87). The changes in activation free energy ($\Delta G^{0\dagger}$) of the TS induced by different perturbations (∂x) correlate with the change in equilibrium free energy (ΔG^0) of the ground states by the proportionality constant α (Eq. 1.12).

$$\alpha_x = \frac{\partial \Delta G^{0\dagger} / \partial x}{\partial \Delta G^0 / \partial x} \quad \text{with } 0 \leq \alpha_x \leq 1 \quad (1.12)$$

The α -value can be used to obtain structural and thermodynamic information on the transition state along a reaction coordinate. A change in ΔG^0 solely caused by a change in $\Delta G_f^{0\dagger}$ indicates that the transition state has native-like properties with respect to the perturbation ($\alpha_x = 1$). But the transition state has the same properties as the unfolded state when the change in ΔG^0 is fully caused by a change in $\Delta G_u^{0\dagger}$ ($\alpha_x = 0$). Therefore, REFERs is a powerful tool to investigate the mechanism of protein folding reactions and to characterize free energy barriers (29, 70, 71).

Various perturbations can be used to derive information on changes in volume $\Delta V^{0\dagger}$,

entropy $\Delta S^{0\ddagger}$, enthalpy $\Delta H^{0\ddagger}$ and solvent exposure ($\Delta C_p^{0\ddagger}$, $m_{f,u}$) between the transition state and the ground state by applying the Gibbs fundamental equation to the transition state (Eq. 1.13) (58, 69).

$$d\Delta G_{f,u}^{0\ddagger} = \Delta V_{f,u}^{0\ddagger} dp - \Delta S_{f,u}^{0\ddagger} dT + m_{f,u} d[D] \quad (1.13)$$

The corresponding REFERS of the respective perturbation (Eq. 1.12) reveal the position of the transition state along the reaction coordinates and can elucidate the mechanism of protein folding reactions. It has been found that transition states are usually compact and partially solvent accessible with a native-like topology (70, 88, 89). Moreover, it was shown for small proteins that folding occurs in at least two sequential steps with an enthalpic and entropic barrier (70-72).

Structural information on interactions in the transition state can also be obtained by the effect of single mutations that are quantified by a Φ -value analogous to the α -value (Eq. 1.14) (70).

$$\alpha_s = \Phi_f = \frac{\partial G^{0\ddagger} / \partial \text{Structure}}{\partial G^0 / \partial \text{Structure}} \quad (1.14)$$

Results from comprehensive analyses revealed that the transition state is a distorted native state and the formation of native interactions is either homogeneously (diffuse TS) or heterogeneously (polarized TS) distributed over the protein (70, 89).

The mechanism of protein folding from the unfolded to the native state is still not fully understood. There are several models proposing the folding pathway. The nucleation-growth model assumes that the tertiary structure propagates rapidly from an initial nucleus of local secondary structure (90). However, this model is rather unlikely as it predicts the absence of folding intermediates (91, 92). The framework or diffusion-collision model suggests that several marginally stable preformed secondary structural elements collide to the native state by diffusion (93, 94). The hydrophobic collapse model suggests a compaction of the protein by a hydrophobic collapse that drives folding due to a reduction of conformational space (49, 95, 96). The recent nucleation condensation model unites features of both the hydrophobic collapse and diffusion-collision model. It proposes that hydrophobic interactions are formed in the transition state and stabilize the otherwise weak secondary structural elements (97, 98). However, a unifying description

of protein folding is still under investigation and the exact mechanism remains unknown (99).

1.1.4 Frictional Effects in Protein Folding

The dependence of several protein folding reactions on viscosity suggested that diffusional processes contribute to the kinetics of protein folding (100-102). An alternative TST formalism specifically for unimolecular reactions in solution provides Kramers' reaction rate theory (103). According to Kramers, a barrier-crossing event can be described as a diffusional process in a one-dimensional energy landscape which is thermally activated and limited by friction. In the case of strong friction, the average rate k of barrier crossing is

$$k = \frac{\omega_0 \omega_{\ddagger}}{2\pi \cdot \gamma} \cdot e^{-\Delta G^{\ddagger}/k_B T} \quad (1.15)$$

where the pre-exponential factor is composed of the frequencies of the motions in the starting well ω_0 and at the barrier top ω_{\ddagger} and the friction coefficient γ . The friction coefficient γ is proportional to the viscosity η of the medium according to the Stokes-Einstein law (Eq. 1.29). Consequently, in the limit of strong friction the overall rate in Kramers' theory decreases inversely with the solvent viscosity $k \propto 1/\eta$ and depends directly on the shape of the free energy barrier A (A depends on ω_0 and ω_{\ddagger}) in contrast to Eyring (Eq. 1.8).

$$k = \frac{A}{\eta} \cdot e^{-\Delta G^{\ddagger}/k_B T} \quad (1.16)$$

Kramers introduced the concept of solvent friction in TST where he assumed that the time scale of solvent relaxation is faster than the time scale of barrier crossing. Thus, solvent friction acts instantaneously or constantly along the reaction coordinate because the solvent is able to equilibrate at each point to the new conformation of the protein. Experimental findings revealed a strong viscosity dependence of protein folding dynamics with a perfect $1/\eta$ dependence as predicted by Kramers indicating that barrier-crossing is fully controlled by solvent motions for some proteins (101, 102, 104, 105). However,

several studies of predominantly small peptides and fast folding proteins have shown a noticeably weaker viscosity dependence than $1/\eta$ which were more consistent with a fractional power law dependence $k \propto \eta^{-\alpha}$. Studies on dynamics in native proteins found α -values between 0.4 – 0.8 associated with energy barriers between 36 – 15 kJ mol⁻¹ (106–108). Jas *et al.* investigated the effect of solvent viscosity on the dynamics of secondary structural elements and found a $1/\eta$ dependence ($\alpha = 1.07$) for β -hairpins and $\alpha = 0.64$ for α -helices with an energy barrier of 21 kJ mol⁻¹ (109). Experiments on chain dynamics in unfolded peptides exhibited a $1/\eta$ dependence ($\alpha = 1$) only for long and flexible peptides but a weaker viscosity dependence for shorter or stiffer peptides with α as low as 0.75 (13, 64, 85) (Fig. 1.11).

The deviation from the Stokes law ($k \propto 1/\eta$) can be explained by a breakdown of Kramers theory. Grote and Hynes predicted a weak solvent viscosity dependence ($\alpha < 1$) when the time scale of barrier crossing is similar to the time scale of solvent motions (memory friction) (110). This is the case for systems where local or narrow energy barriers dominate the dynamics of the folding transition. The Grote-Hynes theory includes a frequency dependent friction that correlates with the local roughness of the energy landscape and leads to a much smaller effective solvent friction in the barrier region as predicted by Kramers. Thus, Kramers constant or memoryless friction approximation can drastically overestimate the impact of solvent motions on barrier crossing (Fig. 1.3).

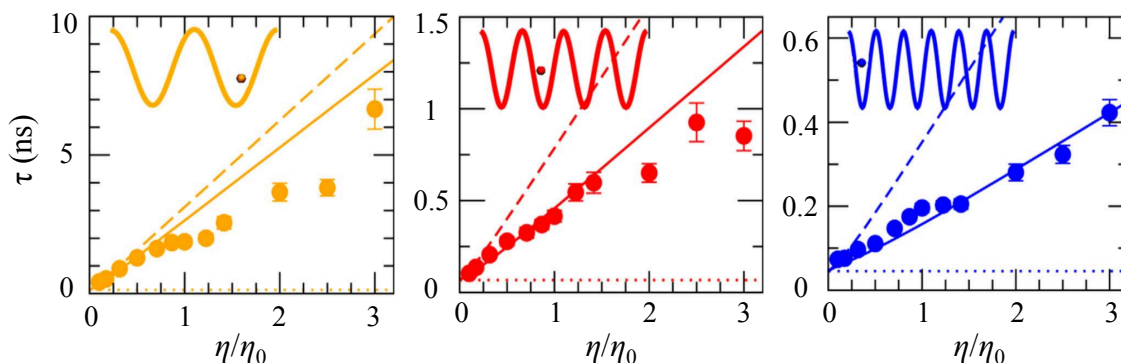


Figure 1.3: Local barrier crossing rates for a particle in explicit water subject to a 1-D external potential. Viscosity-dependent escape times for a particle in potentials with $n = 2, 4$ and 6 minima (left to right). The escape times are results from simulations (filled circles) which are compared with the predictions of different reaction rate theories (lines). Predictions of Grote-Hynes theory with memory friction (solid line), Kramers theory with constant or memoryless friction (dashed line) and transition-state theory where solvent friction is ignored (dotted line). For small n , the Kramers result is a good approximation, but becomes increasingly poor for large n . Figure modified according to de Sancho *et al.* (111).

The weak coupling of protein dynamics and folding reactions to solvent viscosity suggests that, besides solvent friction, internal frictional effects within the protein are important (106-109, 112). A molecular origin of internal friction effects was a long time lacking but recent MD-simulations on dynamics in peptides and proteins interpreted the weak coupling to solvent viscosity due to internal local steric barriers for bond rotations and intramolecular interactions such as hydrogen bonds which is consistent with solvent memory effects (111, 113, 114). This is in agreement with earlier findings by Fleming and co-workers who ascribed the reduced viscosity dependence of photoisomerization rate constants for diphenyl butadiene and DODCI to the presence of barriers for bond rotations during isomerization (115-117). Likewise, the photoisomerization dynamics were better described by the Grote-Hynes theory with memory friction (118).

The concept of internal friction was first discussed in the context of polymer chain dynamics and it was also proposed that internal friction results from sterically restricted bond rotations (119, 120). Later, it was postulated that the total reaction friction is composed of an additive contribution of internal friction to solvent friction (Eq. 1.17) (121-123).

$$f_r = f_{solv} \cdot \left(\frac{\eta}{\eta_0} \right) + f_{int} \quad (1.17)$$

Here, f_r is the friction coefficient, f_{solv} is the solvent friction which depends on the solvent viscosity η and η_0 is the reference solvent viscosity of water at a specific temperature. f_{int} is the internal friction which is independent of the solvent viscosity. Eaton and co-workers also assumed that solvent friction and internal friction of the protein is additive and included it into the Kramers equation (112). Thus, folding time constants with a linear dependence on solvent viscosity ($k \propto 1/\eta$) yield the contribution of internal friction upon extrapolation to vanishing solvent viscosities from the intercept. Based on these assumptions, evidence for internal friction in protein folding and conformational dynamics has been found for various systems (13, 124-129). However, studies with a fractional power law dependence on solvent viscosity ($k \propto \eta^{-\alpha}$) did not confirm the evidence for internal friction in protein folding and conformational dynamics (109, 111, 113, 114, 130). MD-simulations have shown that internal friction arises when local steric barriers for bond rotations or the making/breaking of intramolecular interactions dominate

the barrier crossing process which suggests that internal friction is related with the barrier height as predicted by Grote and Hynes (110, 111, 114).

However, until now it was not clearly demonstrated whether internal friction adds to solvent friction or whether it is related with the activation energy of local barriers and hence modulates the effect of solvent viscosity on protein dynamics and folding reactions.

1.2 α -Helices

The elementary step in protein folding reactions is the formation of intramolecular interactions to explore the conformational allowed space. Contact formation is limited by intrachain diffusion processes which represent the maximum speed limit at which two points in a polymer chain can make contact and is about 5 – 20 ns (13, 14). These interactions may lead to the formation of local and marginally stable secondary structural elements such as loops, β -hairpins and α -helices (Fig. 1.4).

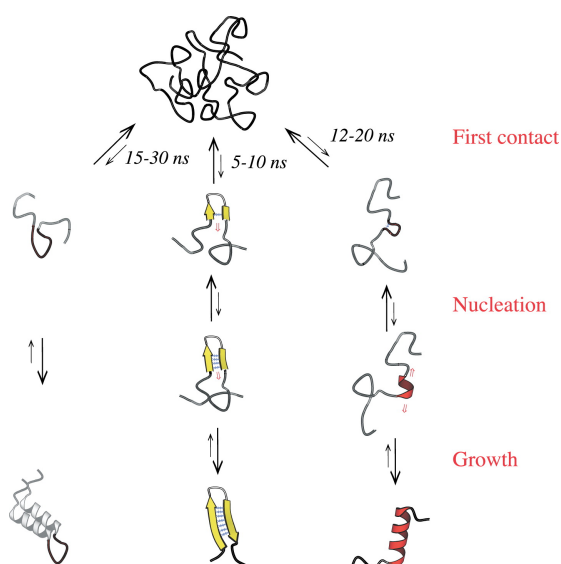


Figure 1.4: Intramolecular contact formation as elementary step to form secondary structural elements in peptides and proteins. Figure according to Krieger *et al.* (14).

The α -helix is the most abundant secondary structural element in proteins (131, 132). The structure of the α -helix was first postulated by Pauling, Corey and Branson in 1951 and later discovered in myoglobin by Kendrew and co-workers (47, 133). α -helices can form independent of the tertiary structure since they are stabilized by local interactions (46, 134). Thus, isolated α -helices are frequently found in peptides and protein folding intermediates (46, 135-139). The average length of α -helices in proteins is 10 amino acids (132). The α -helix is typically a right-handed twisted structure with 3.6 amino acid residues per turn which results in a linear translation of 5.4 Å per turn with a rise of 1.5 Å

per amino acid (Fig 1.5). Consequently, the helix is mainly stabilized by an iterated $i,i+4$ hydrogen bonding pattern of the backbone amine (NH) and carbonyl (CO) groups which leads to unsatisfied hydrogen bond donor and acceptor groups at the ends (Fig. 1.5). Usually the first four NH donor and last four CO acceptor groups of a helix lack intrahelical hydrogen bonds. Only a narrow region of the backbone dihedral angles ϕ and ψ are sterically allowed in α -helices (-57° , -47°) which results in an almost linear geometry of hydrogen bonds with an optimal distance of 2.8 Å between NH donor and CO acceptor (132, 134, 140). The side chains of the amino acids point tangential outward from the helix and slightly directed towards the N-terminus.

The narrower 3_{10} -helix is stabilized by an $i,i+3$ hydrogen bonding pattern of the backbone and is frequently found as N- or C-terminal extension of α -helices. Most 3_{10} -helices are short with an average length of three to four amino acids (140).

The broad π -helix is stabilized by $i,i+5$ hydrogen bonds and is only rarely found in proteins.

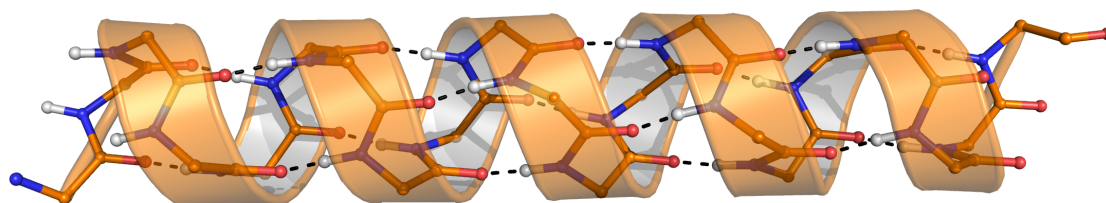


Figure 1.5: Structure of a right-handed α -helix in cartoon and ball and stick representation. The $i,i+4$ hydrogen bonds are displayed by black dashed lines and atoms are shown as coloured balls (nitrogen in blue, hydrogen in white and oxygen in red). Side chains are omitted for clarity (pictured by MacPyMOL).

1.2.1 α -Helix Stability

The α -helix is primarily stabilized by internal backbone hydrogen bonds. John Schellman predicted in 1955 that isolated α -helices are only marginally stable in water and that α -helix formation is enthalpically driven by the formation of internal backbone hydrogen bonds which compensate the loss of conformational entropy of the backbone (134). However, significant helix formation in short, helical peptides of different proteins failed in water at room temperature until Brown and Klee first reported partial helix formation in C-peptide, a modified peptide fragment of ribonuclease A (135, 141, 142). Later, it became apparent that specific side chain interactions such as ion pair and charge-helix dipole interactions were important for helix stability in the C-peptide (46, 143-146) (see section 1.2.2).

The discovery that alanine-based peptides form stable helices in water enabled to study α -helix formation and stability in absence of tertiary interactions and yielded information on intrinsic helix properties (147). Many studies on side chain interactions have been performed and several types of stabilizing interactions were found including salt bridges, hydrogen bonds, hydrophobic interactions, basic-aromatic interactions and polar-nonpolar interactions (146, 148-157). The most stabilizing side chain interactions were found between histidine and aspartate or arginine and glutamate with an $i,i+4$ spacing (152, 155). Covalent side-chain interactions like disulfide bonds can be stabilizing by as much as 2.1 kJ mol^{-1} with a correct spacing (158). Moreover, it was shown that side chain modifications such as phosphorylation of serine stabilize α -helices predominantly at the N-terminus but destabilize at the C-terminus and interior positions due to electrostatic interactions with the helix macro-dipole (159) (see section 1.2.2).

Despite stabilizing side chain interactions, backbone hydrogen bonds make a significant contribution to helix stability. Scholtz *et al.* measured the enthalpy of helix formation in alanine-based peptides by using differential scanning calorimetry (DSC) and found a value of ΔH of about -4.2 kJ mol^{-1} per residue (160). This value is in agreement with Schellman ($\Delta H = -6.3 \text{ kJ mol}^{-1}$ per hydrogen bond) who also predicted that helix formation is enthalpically driven (134). A recent study showed that ΔH does not depend significantly on temperature indicating that the heat capacity change (ΔC_p^0) on helix formation is small (161).

The preferences of amino acids vary for different types of secondary structure. Some amino acids like alanine or leucine are more frequently found in α -helices whereas proline and glycine are rare. Different approaches have been used to determine the intrinsic helix-forming propensity of individual amino acids (140). However, helix propensities are best evaluated in alanine-based peptides where side chain interactions are absent and the effect of a single residue on helix stability can be studied in isolation. Table 1.1 lists the helix propensities of all 20 amino acids. Alanine has the highest helix propensity followed by arginine, lysine and leucine (162). Proline and glycine, in contrast, have the lowest helical propensity which is consistent with previous studies where amino acid preferences for specific positions within the helix were analyzed (163-165). It was found that hydrophobic residues are more abundant at interior positions whereas charged residues are predominantly found at the helix ends. Moreover, glycine is distinctly found outside of the helix at the C-terminal end whereas proline is dominant at both ends outside of the

helix. Consequently, positional preferences of certain amino acids were considered as helix termination signals (164-167).

Glycine substitutions in alanine-based peptides revealed that the destabilizing effect of glycine is more pronounced in central positions than at the helix termini (168). The results indicate that the helix is most stable in the center and least stable at the ends which is in agreement with NMR and other experimental studies (169-171). However, statistical mechanical models were applied in order to understand the helix-coil transition thermodynamically.

1.2.2 The Helix-Dipole and Capping Motifs

The backbone dihedral angles in a helix enable an iterated $i,i+4$ backbone hydrogen bonding between the amide hydrogen donor (NH) and the carbonyl oxygen acceptor (CO). This pattern results in a regular orientation of the amide bond along the helix axis and leads to unsatisfied hydrogen bond donor and acceptor groups at the ends. The amide group is polarized with a partially negatively charged oxygen pointing to the C-terminus and a partially positively charged hydrogen pointing to the N-terminus (Fig. 1.6A). The alignment of several dipoles in the same direction along the helix generates an electrostatic potential at the helix termini with a partial positive charge at the N-terminus and a partial negative charge at the C-terminus (172) (Fig. 1.6). Due to the macro-dipole of the helix, negatively charged residues are often found at the helix N-terminus while positively charged residues are frequently found at the C-terminus (163-167, 173). Helix termini flanking residues stabilize helical conformations by acting as alternative H-bonding partner with the initial four NH and final four CO groups of the backbone which otherwise lack intrahelical H-bond partners, by hydrophobic interactions or by electrostatic interactions with the helix dipole (charge-helix dipole interactions) (134, 144, 167, 173-176). The term helix capping has been used to describe such alternative interactions. Helix capping motifs are usually located at the N', N-cap, N1, N2, N3 or C3, C2, C1, C-cap, C' position of the helix where N1 to C1 are helix interior positions and the primed residues are helix exterior positions. Residues at the N-cap and C-cap position are unique since they participate in hydrogen bonding but have non-helical ψ , ϕ angles. Proline and glycine, which are known to initiate and terminate helices, were often found at the N-cap and C-cap position (164-166, 176).

The effect of capping motifs on helix stability is thermodynamically quite well understood. The biggest effect on stability is at the N-cap and C-cap position where both

electrostatic interactions and hydrogen bonding may occur (166, 173, 177-180). Smaller effects on stability are observed at helical positions (N1, N2), where mostly a charge-helix dipole interaction is dominating or at least hydrogen bonding is geometrically unfavorable (181-185). The best N-caps are aspartate, asparagine, serine and threonine which can accept hydrogen bonds from N2 and N3 NH groups or interact favorably with the helix-dipole (140, 166, 173, 176, 179). Chemical groups at the N-terminus such as acetyl or succinyl were also proven to be stabilizing (143, 144, 176, 186). Preferences at the C-cap position are diverse and less pronounced because of a different helical geometry of side-chain to backbone hydrogen bonds compared to the N-terminus. However, good C-caps are arginine, glutamine, lysine and an amidated C-terminus (140, 166, 176).

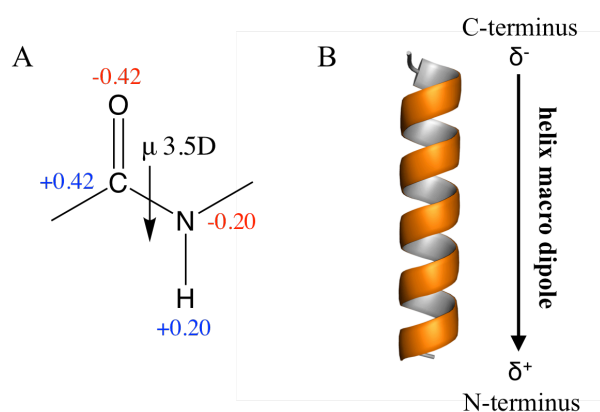


Figure 1.6: The α -helix macro dipole. (A) The charge distribution of the peptide bond produces a dipole moment μ of 3.5 Debye according to Hol *et al.* (174). (B) The alignment of several dipoles in the same direction along the helix axis generates an electrostatic potential at the helix termini with a partial positive charge at the N-terminus and a partial negative charge at the C-terminus (172).

1.2.3 Statistical Mechanical Models of the Helix-Coil Transition

Helix formation can be divided into two steps. Helix nucleation represents the formation of the first helical turn and can occur at any position within a sequence. However, helix nucleation is rare and energetically unfavorable due to the entropic cost of fixing four consecutive residues in a helical conformation in order to form a single hydrogen bond. Helix propagation, in contrast, is energetically favorable because adding single residues at either end of a helical segment results in an additional hydrogen bond. Thus, helix growth is faster and more probable than nucleation and conformations with multiple helical segments are expected to be rare in short peptides (single sequence approximation). The entropy loss that originates from the restriction of backbone dihedral angles ϕ and ψ in a helical conformation is compensated by the gain in enthalpy of hydrogen bonding in

helical segments. However, helical residues close to the helix-coil boundary remain energetically unfavorable, because they are only partially involved in $i, i+4$ hydrogen bonding and lack either hydrogen bond donor or acceptor groups. Hence, the state of a residue depends on the conformation of neighboring residues. Due to this, isolated helices show a low cooperativity with the highest helix probability in the center and the lowest at the ends. Thus, isolated α -helices in solution do not follow a simple two-state equilibrium between a fully folded and fully unfolded state. Instead, the thermodynamics of the helix-coil transition are more complex and have to be treated as multi-state transition (140, 168-171, 187-189).

Based on the linear Ising model two statistical mechanical models were introduced by Zimm and Bragg and by Lifson and Roig to describe the helix-coil transition in polypeptides quantitatively (187, 188, 190).

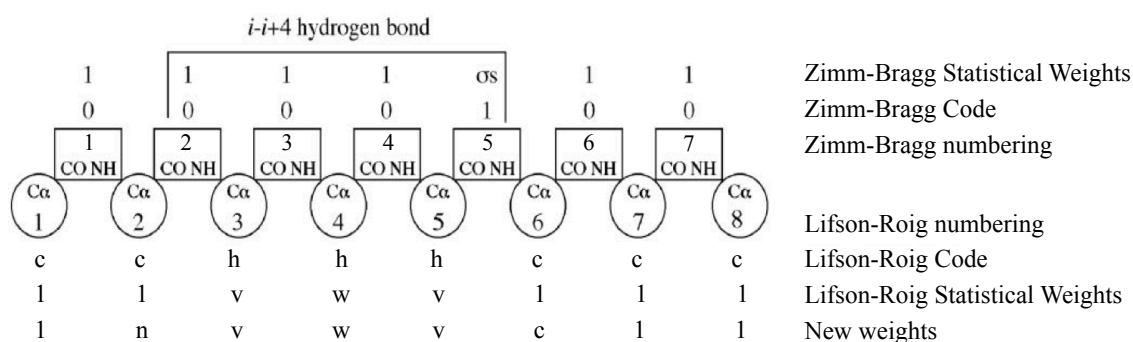


Figure 1.7: Numberings, codes and statistical weights for the Zimm-Bragg and Lifson-Roig models. Figure modified according to Qian & Schellman (189) and Doig *et al.* (178).

In the Zimm-Bragg model (ZB) amino acids are considered as helical (1) or coil (0) on the basis of whether their peptide NH group participates in hydrogen bonding within the helix or not (Fig. 1.7). Based on this, there are three different statistical weights. Helix propagation has a statistical weight of s , helix nucleation has a statistical weight of σs whereas coil or non-hydrogen bonded peptide groups have a statistical weight of 1. The propagation parameter s can be interpreted as an equilibrium constant between a residue in the coil and in the helical state and was determined experimentally for all 20 amino acids (Tab. 1.1). Helix nucleation, in contrast, is energetically unfavorable and is paid only once for each helix. Thus, the nucleation parameter σ is very small and similar for all 20 amino acids (140, 187).

In the Lifson-Roig model (LR) amino acid residues are considered as helical (h) or coil (c) on the basis of their backbone dihedral angles ϕ and ψ (Fig. 1.7). The LR model gives

each residue a statistical weight depending on their conformations and the conformations of surrounding residues of a triplet (Tab. 1.1). Residues in a helical segment have a statistical weight of w . The propagation parameter w can be interpreted as an equilibrium constant analogous to the s -value from the ZB model. Coil residues are used as a reference and have a weight of 1. Helical residues at the helix-coil boundary are assigned weights of v . The nucleation parameter v is analogous to the σ -value from the ZB model (140, 188). The ratio of w and v gives the approximate effect of hydrogen bonding ($1.7:0.036$ for Ala or $-RT \ln(1.7/0.036) = -2.1 \text{ kcal mol}^{-1}$ or 8.8 kJ mol^{-1}) (162). N- and C-capping preferences were also included into the model to account for capping effects at the helix ends by assignment of statistical weights n and c (162, 176, 178) (Fig. 1.7, Tab. 1.1). Also weights for the N1, N2 and N3 position ($n1$, $n2$, $n3$) and side chain interactions were introduced to improve theoretical predictions on helices (140, 191, 192).

Table 1.1: Helix propagation and capping propensities of all natural amino acids.

amino acid	s -value	w -value	n -value	c -value
Ala	1.64	1.70	1.00	1.00
Arg	1.10	1.14	1.00	2.10
Lys	0.97	1.00	0.72	1.10
Leu	0.84	0.87	2.06	1.20
Met	0.63	0.65	1.31	1.60
Gln	0.60	0.62	0.12	2.40
Glu	0.52	0.54	2.06	0.41
Tyr	0.46	0.48	4.90	1.00
Ile	0.44	0.46	1.57	1.00
Ser	0.39	0.40	3.90	0.21
Asp	0.37	0.38	6.60	0.66
His	0.35	0.36	1.31	1.40
Cys	0.31	0.32	5.40	1.00
Asn	0.28	0.29	6.80	0.78
Trp	0.28	0.29	3.60	1.00
Phe	0.26	0.27	2.06	1.00
Val	0.24	0.25	0.96	0.21
Thr	0.17	0.18	2.23	1.00
Gly	0.05	0.048	8.85	0.88
Pro	<0.001	<0.001	1.35	1.00

The w -value at 273 Kelvin of the Lifson-Roig model (162) is converted to the corresponding s -value of the Zimm-Bragg model with $v = 0.036$ (Eq. 1.18). The N- and C-capping propensities are given as n - and c -values according to Rohl *et al.* and Doig & Baldwin (162, 176). However, the helix and capping propensities of Trp, Tyr and Phe residues are error-prone due to the aromatic contributions to the CD-signal at 222 nm (193).

The LR model is more widely used than the ZB model since it is easier to handle conceptually. The parameters w and v are assigned to individual residues and therefore a substitution changes only the w - and v -values at that position (140). However, the statistical weights of the two models are related by (189)

$$s = \frac{w}{1+v} \text{ and } \sigma = \frac{v^2}{(1+v)^4} \quad (1.18)$$

The complete helix-coil equilibrium of every conformation is obtained by the partition function (Z). The partition function is the sum of statistical weights of every possible conformation which is calculated by using matrix methods. The probability of each conformation is given by the statistical weight of that conformation ($v^2 w^{N-2}$ with N residues) divided by the partition function (140, 187, 188).

1.2.4 Dynamics of the Helix-Coil Transition

The kinetic mechanism of the helix-coil transition has long been under debate and was mainly investigated by perturbation-induced methods in different solvents. Dielectric relaxation and ultrasonic absorption techniques revealed mean relaxation times for helix unfolding on the hundreds of nanoseconds to microsecond time scale (194-196). The theory of Schwarz relates these relaxation times to helix growth reactions and a maximum rate constant for helix elongation of $k_1 = 10^{11} - 10^{10} \text{ s}^{-1}$ was obtained (194).

Nanosecond temperature-jump techniques combined with fluorescence, UV resonance Raman or infrared (IR) spectroscopy revealed relaxation times for helix unfolding on the hundreds of nanoseconds in alanine-based peptides with apparent activation energies of $\sim 34 \text{ kJ mol}^{-1}$ and similar rate constants for helix elongation of $k_1 = 10^8 \text{ s}^{-1}$ (197-203). However, isolated α -helices do not follow a simple two-state transition and consequently an interpretation of relaxation rate constants in terms of local folding and unfolding dynamics is difficult. Another problem is associated with the probing reaction itself, which often reports on global changes.

The multi-state character of α -helices was confirmed in a recent study, which applied intramolecular triplet-triplet energy transfer (TTET) to investigate local folding and unfolding dynamics at different positions within a helix of 21 amino acids (170) (see section 1.3). The results revealed a position-dependent rate constant for helix

unfolding with slower unfolding kinetics in the helix center ($1/k_u = 1.4 \mu\text{s}$) compared with the helix ends ($1/k_u = 250 \text{ ns}$). In contrast, helix formation is independent of the position with a time constant of $1/k_f = 400 \text{ ns}$. Consequently, the helix is most stable in the center and least stable at the ends, which is in agreement with previous results (168, 169, 171) (see section 1.3.2).

1.3 Triplet-Triplet Energy Transfer (TTET)

Triplet-triplet energy transfer (TTET) is able to directly monitor site-specific interactions in peptides and proteins. TTET is a two-electron transfer process (Dexter mechanism) that is based on *van-der-Waals* contact or orbital overlap between a triplet donor and triplet acceptor (204). Thus, TTET is a short-range energy transfer and the rate of energy transfer k_{ET} was shown to decay exponentially with the distance R_{DA} separating donor and acceptor (Eq. 1.19).

$$k_{ET} = A \cdot e^{-\frac{2R_{DA}}{L}} \quad (1.19)$$

Here, A denotes a factor that depends on the photophysical properties of donor and acceptor and L is the average *van-der-Waals* radius of donor and acceptor (204). The strong distance dependence of TTET is an important difference to Förster resonance energy transfer (FRET). Here, energy transfer occurs through space by dipole-dipole interactions (Förster mechanism) and does not require *van-der-Waals* contact of donor and acceptor (205). Consequently, FRET is a long-range energy transfer and the rate of energy transfer decays with $1/R_{DA}^6$ of the distance separating donor and acceptor.

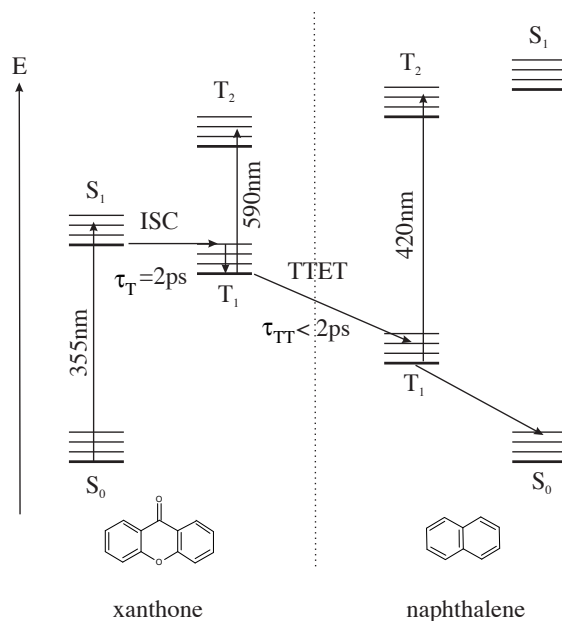


Figure 1.8: Jablonski diagram for triplet-triplet energy transfer (TTET) between xanthone (Xan) as donor and naphthalene (Nal) as acceptor. Xan is excited to its singlet state S_1 by a short laser pulse at 355 nm from where it undergoes intersystem crossing (ISC) to its triplet state T_1 (internal conversion of $^3n\pi^*$ to $^3\pi\pi^*$) (206, 207). The irreversible triplet transfer is enabled by *van-der-Waals* contact between Xan and Nal. The triplet state of Xan and Nal can be monitored by absorbance at 590 nm and 420 nm (T_1 - T_2 transition). The triplet state of Nal undergoes internal conversion to the singlet ground state S_0 in the absence of quencher. Figure according to Fierz & Kiefhaber (18).

A well-suited triplet donor-acceptor pair in aqueous solution is xanthone (Xan) and naphthalene (Nal). Xan is excited to its singlet state S_1 by a short laser pulse at 355 nm, from where it undergoes fast intersystem crossing (ISC) to the triplet state T_1 (~ 2 ps) with a quantum yield of $\Phi_T \sim 99\%$ (Fig. 1.8) (206, 207). The triplet state of Xan is relatively long-lived with a lifetime of 50 – 100 μs because the relaxation to the singlet ground state S_0 is spin-forbidden. The transfer of the triplet state between Xan and Nal is fast (< 2 ps) with a reactive boundary of 4.4 \AA and irreversible since the triplet state of Nal is lower in energy than the triplet state of Xan (13, 14, 206, 208). The triplet states of Xan and Nal have characteristic absorbance bands at 590 nm and 420 nm respectively, and therefore TTET can be monitored by time-resolved absorbance spectroscopy (Fig. 1.8, 1.9) (18).

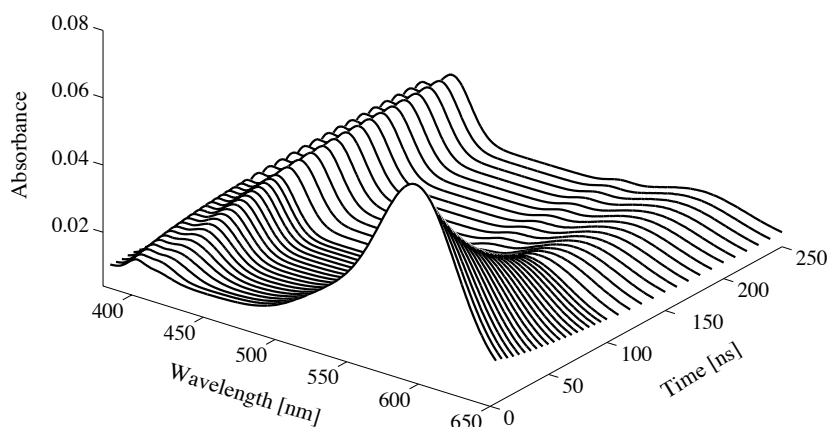


Figure 1.9: Time-resolved absorbance spectroscopy of triplet-triplet energy transfer (TTET) between xanthone and naphthalene. The triplet state absorbance decay of Xan and concomitant absorbance rise of Nal can be monitored at 590 nm and 420 nm. Figure according to Krieger *et al.* (14).

Experiments under pseudo-first order conditions have shown that the triplet transfer reaction between Xan and Nal is diffusion-controlled with a bimolecular transfer rate constant of $k_{ET} = 4 \cdot 10^9 \text{ M}^{-1} \text{ s}^{-1}$ (14, 206). It was also shown that the rate constant for TTET is inversely proportional to solvent viscosity ($k_{ET} \propto 1/\eta$) with an activation energy of zero ($E_a = 0$) as expected for a diffusion-controlled reaction (13, 14, 18). Thus, each encounter complex leads to efficient electron transfer. The time resolution of this method is set by the photophysics of triplet formation and triplet transfer which is within picoseconds and the upper time limit of processes that can be monitored by TTET is given by the triplet lifetime of Xan. Hence, TTET between Xan and Nal allows measurements of absolute rate constants for contact formation k_c for processes slower than 10 – 20 ps up to 50 – 100 μs . When the triplet donor and acceptor groups are attached to polypeptides, the

TTET kinetics are dominated by the dynamics and conformational properties of the polypeptide chain.

1.3.1 TTET in Unfolded Polypeptides

Introducing the TTET labels in unfolded model peptides such as poly(Gly-Ser) and poly(Ser) yields information on global and local dynamics of loop formation in unstructured polypeptides. However, this depends on the label spacing and position within the peptide (14, 78). The transfer of the triplet state requires *van-der-Waals* contact of the TTET labels and occurs through loop formation of the peptide (Fig. 1.10) (13, 14). The observed TTET kinetics reflect the rate of intramolecular contact formation, which is limited by intrachain diffusion processes and can be described by a single exponential process. Single exponential kinetics indicate that interconversion between all different conformations in the unfolded ensemble is faster than contact formation k_c and that only a small fraction of molecules forms contact. This is in accordance with the theory of Szabo, Schulten and Schulten who treated the loop closure reaction as a mean first passage time of end-to-end diffusion of the polymer (209).

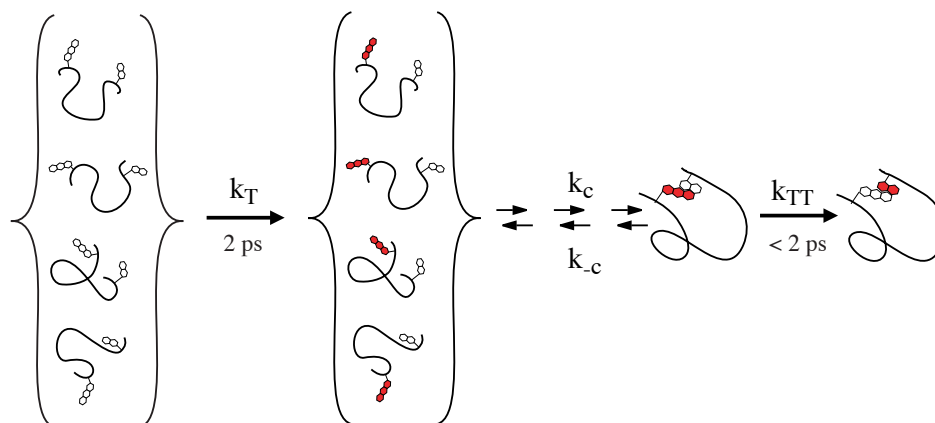


Figure 1.10: Intramolecular triplet-triplet energy transfer (TTET) between xanthone and naphthalene to monitor loop formation in unfolded polypeptide chains. The red labels indicate groups that are in triplet state. Triplet formation k_T of Xan and triplet transfer k_{TT} between Xan and Nal are within 2 ps. However, intramolecular contact formation k_c between Xan and Nal depends on the dynamics and conformational properties of the polypeptide chain. Figure according to Krieger *et al.* (210).

Previous results have shown that end-to-end contact formation k_c depends on the loop size and amino acid sequence (13, 14, 79, 85). Over short distances, k_c is almost independent of the chain length with a maximum value of 5 – 12 ns which is due to chain stiffness limiting dynamics (Fig. 1.11A). However, over longer distances contact formation is

dependent on the chain length and decreases with $N^{-1.7 \pm 0.1}$ (N = number of peptide bonds) which is in agreement with a Gaussian chain with excluded volume effects. (14). The effect of amino acids on contact formation is less pronounced. Glycine and proline (*cis* conformation) show the fastest rate constant for contact formation because of increased flexibility or close end-to-end distances, respectively. In contrast, proline in *trans* conformation leads to a dramatic decrease in k_c (85).

The dynamics of loop formation additionally depend on the position within a peptide chain. Internal positions are intrinsically less flexible and more coupled to motions of other chain segments than external positions and consequently leads to slower loop formation (78). Moreover, it was shown that formation of long loops in flexible chains is inversely related with the solvent viscosity ($k_c \propto 1/\eta$, $\alpha = 1$) with low activation energies as expected for a diffusion-controlled reaction (Fig. 1.11B, C). However, formation of short loops is not fully diffusion-controlled with a fractional solvent viscosity dependence ($\alpha < 1$) and activation energies up to 20 kJ mol⁻¹ (78, 85, 211, 212).

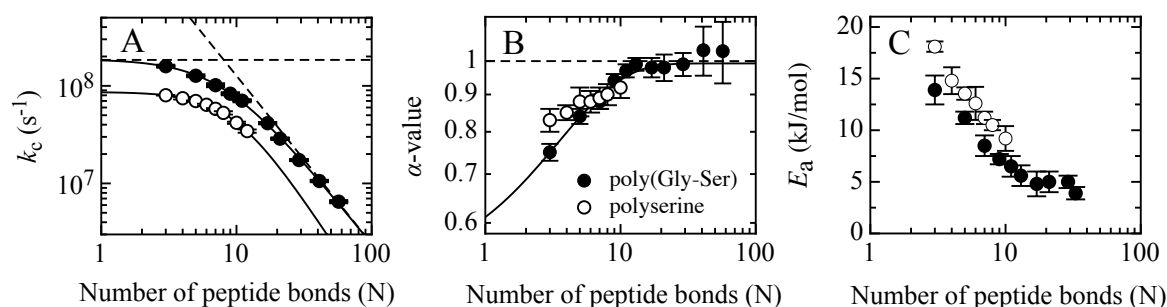


Figure 1.11: Effect of increasing chain length on conformational dynamics in unfolded polypeptide chains. (A) Effect of increasing chain length (N) on the rate constant for intramolecular contact formation k_c in poly(Gly-Ser) (filled circles) and poly(Ser) (open circles) peptides measured by TTET. The solid line represents a fit of the equation $k_c = 1/(1/k_0) + (1/k_1 N^m)$ to the data. (B) Effect of increasing chain length (N) on the viscosity-dependence (α) of intramolecular contact formation k_c in unfolded polypeptides. (C) Effect of increasing chain length (N) on the activation energy E_a for intramolecular contact formation k_c . Figure modified according to Krieger *et al.* (14) and (211, 212).

The effect of denaturants such as urea or GdmCl on the logarithm of loop formation $\ln k_c$ is linearly related by the m -value (Eq. 1.20) (64, 69).

$$\ln k_c = \ln k_c^0 - \frac{m[D]}{RT} \quad (1.20)$$

Here, k_c^0 is the rate constant for loop formation at zero denaturant and k_c is the rate constant for loop formation at the respective denaturant concentration [D]. Loop formation is decreased with increasing denaturant concentration and this linear dependence is a result of two additive non-linear effects. One effect results from increased solvent viscosity and the other from decreased chain dynamics due to denaturant binding to the backbone. The different efficiency of GdmCl and urea in slowing down chain dynamics is based on their different affinities to the polypeptide backbone (64).

1.3.2 TTET in Folded Peptides and Proteins

TTET can also be applied to monitor conformational dynamics in folded peptides and proteins. Therefore, the irreversible TTET reaction is coupled as a probing reaction to a folding and unfolding equilibrium of helical peptides or proteins in order to yield the microscopic rate constants for folding k_f and unfolding k_u under equilibrium conditions (Eq. 1.21) (170, 213).



Here, N represents the folded state, U the unfolded or partially unfolded state with separated labels and U* is the unfolded state with labels in *van-der-Waals* contact and enabled triplet transfer to Nal. One prerequisite for the application of TTET is that triplet transfer between the labels is prevented in the folded state and enabled in the unfolded state by loop formation. Moreover, TTET have to be on a similar timescale or even faster than the folding-unfolding equilibrium and both states U and N of the equilibrium have to be populated to detectable amounts to unravel conformational dynamics.

The villin headpiece subdomain (HP35) is a perfect model for studying conformational fluctuations in the native state of proteins because of its small size and rapid folding. TTET experiments at different positions within the protein revealed a native-state heterogeneity in HP35 (213). TTET in natural sequences is more difficult since the triplet state might be quenched by aromatic amino acids. It was shown in a previous study that methionine, tryptophan, tyrosine and histidine quench Xan triplets very efficiently whereas cysteine or the free N-terminus (NH_3^+) quench rather inefficiently (210).

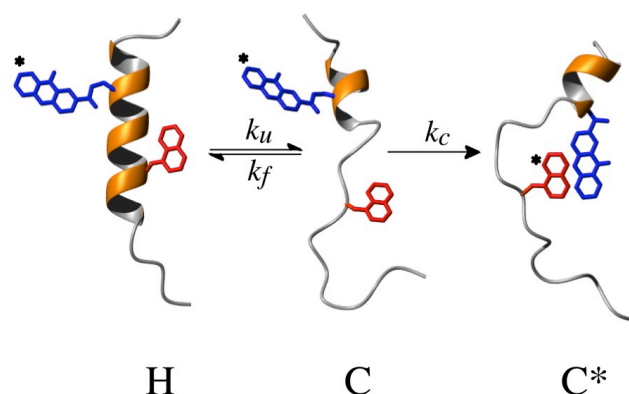


Figure 1.12: Schematic representation of TTET coupled to a helix-coil equilibrium. The triplet labels xanthone (Xan, blue) and naphthalene (Nal, red) are placed in the helix with an $i,i+6$ spacing. Figure according to Neumaier *et al.* (186).

Conformational dynamics of α -helices were investigated in alanine-based model peptides. In order to probe helix-coil dynamics, the triplet donor Xan and acceptor Nal were attached in an $i,i+6$ spacing within helical peptides (Fig. 1.12). This places the labels on opposing sides of the helix and prevents TTET in the folded helical state (H). Helix unfolding or at least partial unfolding between the labels (C) is required to enable the transfer of the triplet state by contact formation (C*) (170, 186). A previous study applied TTET to investigate local folding and unfolding dynamics at different positions within a helix of 21 amino acids (aa) (170). The TTET experiments revealed slower unfolding kinetics in the helix center ($1/k_u = 1.4 \mu\text{s}$) compared with the helix ends ($1/k_u = 250 \text{ ns}$) and position-independent helix formation kinetics ($1/k_f = 400 \text{ ns}$) (Fig. 1.13). Consequently, the helix is most stable in the center and least stable at the ends, which is in agreement with previous results (168, 169, 171).

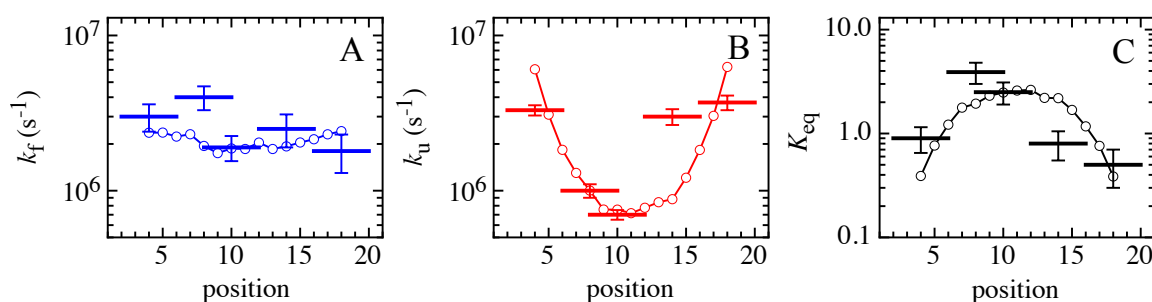
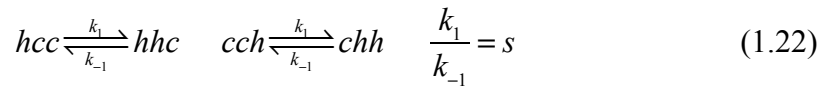


Figure 1.13: Position dependence of local helix-coil dynamics and stability. The horizontal bars indicate the regions of helix probed in the different peptides. The microscopic rate constants for helix formation k_f (blue bars) (A) and helix unfolding k_u (red bars) (B) obtained from a global fit of the TTET kinetics are shown in addition to the equilibrium constant K_{eq} (black bars) (C). For comparison, the results from the simulations using the kinetic Ising model (open circles). Figure modified according to Fierz *et al.* (170).

Monte Carlo simulations based on a kinetic version of the linear Ising model reproduced the experimentally observed dynamics of helix folding and unfolding which demonstrated that the linear Ising model is also able to describe the dynamics of the helix-coil transition (Fig. 1.13). The statistical weights of the Zimm-Bragg model were used and only the state of neighboring residues in a triplet were considered for their simulations (187). Based on this, three types of elementary reactions of the helix-coil transition can be distinguished:

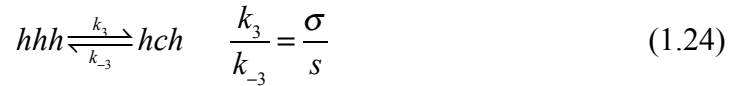
Helix elongation:



Helix nucleation:



Coil nucleation:



The kinetic extensions of the model introduced by Schwarz were also included to allow for additional kinetic effects on nucleation (γ_i) reactions relative to elongation (194).

$$\begin{aligned} k_2 &= \gamma_h \cdot \sigma \cdot k_1 & k_{-2} &= \gamma_h \cdot k_{-1} \\ k_3 &= \gamma_c \cdot \sigma \cdot k_2 & k_{-3} &= \gamma_c \cdot k_1 \quad \text{with} \quad 1 \leq \gamma \ll \frac{1}{\sqrt{\sigma}} \end{aligned} \quad (1.25)$$

The simulations indicated that equilibrium helix-coil dynamics are governed by a diffusive process of the helix-coil boundary along the peptide backbone, whereas helix and coil nucleation events are extremely rarely observed. The helix-coil boundary is more frequently located near the ends than at the center (168, 170). Thus, the boundary takes on average longer to reach the helix center which leads to the observed position-dependence of helix unfolding (Fig. 1.13B). However, helix growth is a local folding process and is consequently independent of the position within the helix which is in agreement with their experimental data (Fig. 1.13A). Based on the simulations, the rate constant of the elementary step for helix elongation $k_1 = 2.1 \cdot 10^7 \text{ s}^{-1}$ ($1/k_1 = 48 \text{ ns}$) and helix unfolding $k_{-1} = 1.6 \cdot 10^7 \text{ s}^{-1}$ ($1/k_{-1} = 63 \text{ ns}$) was obtained. In the TTET experiments a region of five

residues was probed because of an $i,i+6$ spacing of the labels. The simulation assumed that contact is prevented if at least four residues between the TTET labels are helical (170).

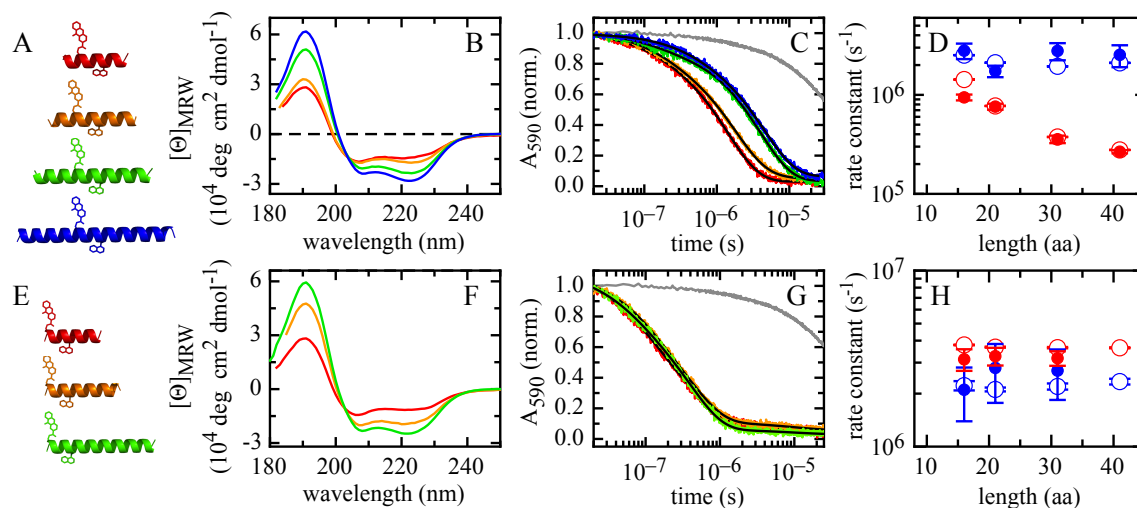


Figure 1.14: Effect of peptide length on local helix-coil dynamics and stability. Peptides of different length with central (A-D) or N-terminal TTET labels (E-H). Far-UV CD spectra (B, F) and triplet absorbance decay curves of xanthone monitored at 590 nm (C, G). The colors in the plots correspond to the colors of the helical peptides in A and E. The grey line in C and G represents the triplet lifetime of the donor-only reference and the black lines represent double exponential fits to the kinetics. A global fit of the urea dependence data using the analytical solution of the three-state model yielded the rate constant for helix folding k_f (blue circles) and unfolding k_u (red circles) (D, H). The experimental data (filled circles) agree well with results from Monte Carlo simulations (open circles) based on the linear Ising model. Figure according to Neumaier *et al.* (186).

In further TTET experiments, Neumaier *et al.* analyzed whether helix-coil dynamics follow a one-dimensional diffusing boundary mechanism (186). The predictions of the linear Ising model suggest that helix unfolding is slowed down in the helix center with increasing helix length due to an increased distance from the helix-coil boundary to the center. Therefore, the effect of peptide length on helix folding and unfolding dynamics was analyzed in polyalanine-based peptides with central or N-terminal TTET labels (Fig. 1.14). In agreement with the prediction from the linear Ising model they showed that helix unfolding in the center is slowed down with increasing length of the peptides, whereas helix unfolding at the N-terminus is length-independent (Fig. 1.14 D, H). Helix folding, in contrast, is independent of peptide length at both central and N-terminal positions, which can be described by a one-dimensional diffusion mechanism of the helix-coil boundary.

Diffusion is the random motion of molecules or small particles in a fluid arising from thermal fluctuations (Brownian motion). Einstein and Smoluchowski could show that the

mean-square displacement (MSD) of Brownian particles in a liquid is directly related to the diffusion coefficient (Eq. 1.26) (214, 215).

$$\langle x^2 \rangle = 2Dt \quad (1.26)$$

Here, $\langle x^2 \rangle$ is the MSD of a particle with respect to the original position after a specific time t and D is the one-dimensional diffusion coefficient. Hence, the diffusion distance of the helix-coil boundary is proportional to the square root of the diffusion time when the conformational dynamics of α -helices follow a classical one-dimensional diffusion law. For a classical 1-D diffusion mechanism with diffusion from two sides, the survival probability S for the helix in the center can be approximated by a single exponential function (Eq. 1.27) which results in a modified Einstein equation (Eq. 1.28) (186).

$$S \approx e^{-\frac{4Dt}{\langle l^2 \rangle}} = e^{-k_u t} \quad (1.27)$$

$$\langle l^2 \rangle \approx \frac{4D}{k_u} \quad (1.28)$$

Here, D is an upper limit for the diffusion coefficient of one boundary, $\langle l^2 \rangle$ is the average distance from the helix-coil boundary to the helix center and $1/k_u$ is the required unfolding time of both boundaries to reach the helix center. They assumed an average position of the boundary at position 2 and $n-1$. In order to test whether boundary diffusion follows a classical 1-D diffusion law, the effect of the diffusion distance $\langle l^2 \rangle$ on the observed time constant for helix unfolding $1/k_u$ in the center of each peptide was analyzed (Fig. 1.15). The relationship of $\langle l^2 \rangle$ vs. $1/k_u$ was linear which demonstrates that helix-coil boundary diffusion can be described by a classical, Einstein-type, 1-D diffusion process with a diffusion coefficient of $D = 2.7 \cdot 10^7$ (amino acids)² s⁻¹ or $6.1 \cdot 10^{-9}$ cm² s⁻¹ (186).

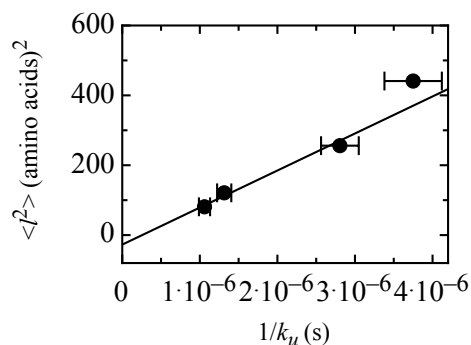


Figure 1.15: Correlation between the distance of boundary diffusion and the time constant for helix unfolding. The average diffusion distance, l , of the boundaries were calculated between position 2 and the C-terminal label (Nal) for diffusion from the N-terminus and between position $n-1$ and the N-terminal label (Xan) for diffusion from the C-terminus (given as numbers of amino acids). The plot of $\langle l^2 \rangle$ vs. $1/k_u$ is linear with a slope of $1.1 \cdot 10^8$ aa² s⁻¹ indicating that boundary diffusion can be described by equation 1.27. The solid line represents a fit of equation 1.28 to the data for the three shortest helices and yields $D = 2.7 \cdot 10^7$ aa² s⁻¹ or $6.1 \cdot 10^{-9}$ cm² s⁻¹. Figure modified according to Neumaier *et al.* (186).

With this approach it is possible to characterize the boundary diffusion mechanism in more detail. According to the Stoke-Einstein law, diffusion is driven by thermal energy and limited by frictional forces (Eq. 1.29) (214, 216).

$$D = \frac{k_B T}{f_r} \quad \text{with} \quad f_r = 6\pi \cdot \eta \cdot r_s \quad (1.29)$$

Consequently, the diffusion coefficient is directly proportional to the thermal energy ($D \propto k_B T$), where k_B is the Boltzmann constant and T the absolute temperature, and inversely proportional to the frictional coefficient f_r which is related to the viscosity of the medium η ($D \propto 1/\eta$) and the hydrodynamic radius r_s for spherical particles according to Stokes (216). The viscosity and temperature dependence of the diffusion coefficient for boundary diffusion therefore gives information about the rate-limiting step of the boundary diffusion mechanism.

However, in these TTET experiments a region of 5 residues between the labels was probed ($i, i+6$). This spacing leads to some uncertainties in defining a reliable diffusion distance $\langle l^2 \rangle$ since it is not known how many residues between the labels have to be unfolded to enable TTET. The diffusion coefficient D depends on the diffusion distance that is considered and inaccurate diffusion distances results in an unreliable diffusion coefficient. Thus, a TTET label spacing approach is required which reduce the uncertainty in the diffusion distance $\langle l^2 \rangle$ and enable to determine a more reliable diffusion

coefficient D . An accurate diffusion coefficient enables to characterize whether boundary diffusion is purely diffusion-controlled or limited by activation energies.

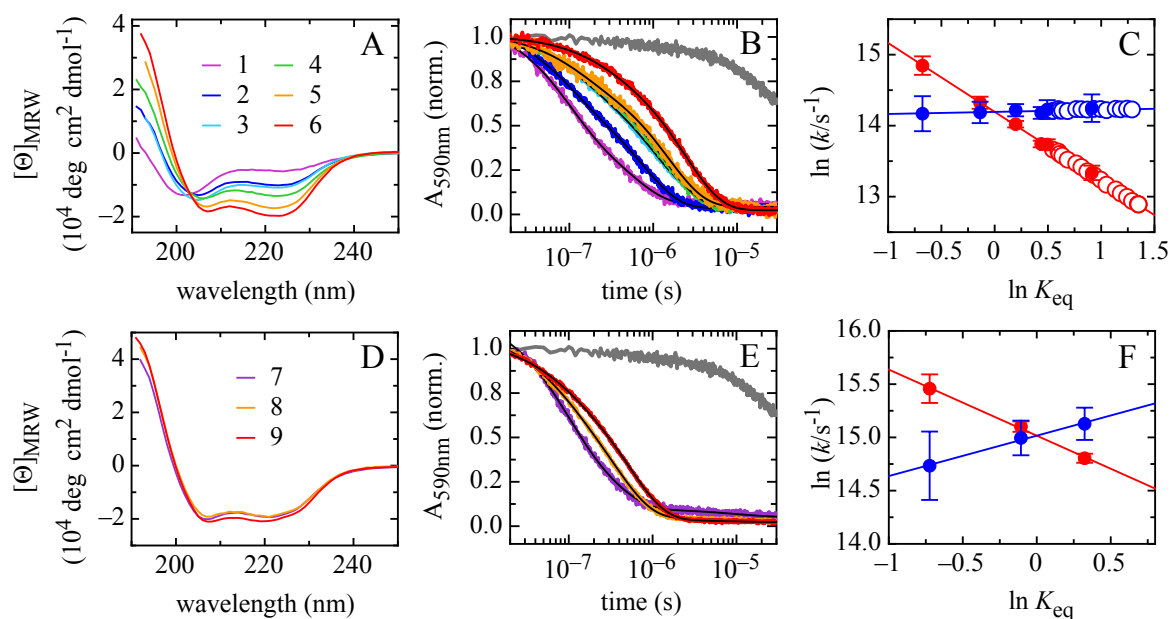


Figure 1.16: Effect of different capping motifs on helix stability and dynamics. (A-C) Effect of different end-capping motifs on helix stability and dynamics in the center of a 21 aa peptide. Free N-terminus and amidated C-terminus (C-cap) (1), free N-terminus/N-Thr and C-cap (2), N-acetyl and free C-terminus (3), N-acetyl/N3-Serine and C-cap (4), N-acetyl and C-cap (5), N-succinyl and C-cap (6). (D-F) Effect of different N-capping motifs on helix stability and dynamics at the N-terminus of a 21 aa peptide. Free N-terminus and C-cap (7), N-acetyl and C-cap (8) and N-succinyl and C-cap (9). Far-UV CD spectra (A, D) and xanthone triplet absorbance decay monitored at 590 nm (B, E). The grey line in B and E represents the triplet lifetime of the donor-only reference and the black lines represent double exponential fits to the data. Leffler plots (C, F) of helix growth k_f (blue) and helix unfolding k_u (red). The experimental data (filled circles) are compared with results from Monte Carlo simulations (open circles). Figure modified according to Neumaier *et al.* (186).

The effect of N- and C-capping motifs on the dynamics of helix folding and unfolding is not fully understood. Recent results revealed that stabilizing or destabilizing the ends of the helix by charged groups affects helix unfolding k_u but not refolding k_f in the center with $\Phi_u = 0.97$ and $\Phi_f = 0.03$ (186) (Fig. 1.16). Thus, helix stability in the center is changed remote from the region of stabilization or destabilization and the molecular origin of this non-local effect is still unknown. A potential explanation of this non-local effect might be attributed either to an impact on the diffusion coefficient D for boundary diffusion or to different diffusion distances $\langle l^2 \rangle$ from the helix-coil boundary to the center. However, this requires a method to determine reliably and accurately the diffusion coefficient for boundary diffusion. Locally, capping motifs have an impact on both helix folding ($\Phi_f = 0.35$) and unfolding rate constants ($\Phi_u = 0.65$) suggesting that these

interactions are already present in the transition state of helix formation which gives rise to an impact of capping motifs on the energy barrier encountered by boundary diffusion (Fig. 1.16).

2 Aim of Research

Experimental and theoretical work on α -helices have shown that a linear Ising model is able to describe thermodynamic and kinetic properties of the helix-coil transition (134, 160, 168-170, 187-190, 194-196, 217). Moreover, previous TTET studies demonstrated that equilibrium helix-coil dynamics are governed by a diffusion of the helix-coil boundary along the peptide backbone and that boundary diffusion follows a classical, Einstein-type, 1-D diffusion law with a diffusion coefficient of $D = 2.7 \cdot 10^7$ (amino acids)² s⁻¹ or $6.1 \cdot 10^{-9}$ cm² s⁻¹ (170, 186, 194).

However, in these TTET experiments a region of 5 residues between the labels was probed (i,i+6 spacing) (186). Since it is unknown how many segments between the labels have to unfold in order to enable TTET there is some uncertainty in defining the diffusion distance $\langle l^2 \rangle$. The diffusion coefficient D depends on the diffusion distance that is considered and an imprecise diffusion distance results in an unreliable diffusion coefficient.

The aim of the present study is to decrease the uncertainty in the diffusion distance and thus to determine a more reliable diffusion coefficient. An i,i+2 spacing should enable a more exact determination of the diffusion distance because there is a defined position of the boundary when TTET occurs. On the basis of a more accurate determination of the diffusion coefficient, it is possible to characterize the boundary diffusion mechanism of α -helices in more detail. A purely diffusion-controlled reaction scales inversely with the solvent viscosity ($D \propto 1/\eta$) and directly with the temperature ($D \propto RT$) with an activation energy close to zero ($E_a = 0$). Thus, we can analyze the effect of solvent viscosity η and temperature T on the diffusion coefficient D for boundary diffusion to determine whether solvent friction or energy barriers are rate-limiting. This is investigated by TTET in alanine-based peptides of different length and central TTET labels under various conditions.

Based on these experiments, we want to study whether internal friction is related with local energy barriers. We assume that boundary diffusion is limited by the formation and breakage of hydrogen bonds and by steric barriers for bond rotations. Thus, internal friction effects should exist in the diffusing boundary mechanism and should correlate with the activation energy E_a . Grote and Hynes predicted a weak solvent viscosity dependence ($\alpha < 1$) for systems with local, narrow energy barriers (110). Hence, the sensitivity of boundary diffusion to solvent viscosity α should correlate with the activation energy E_a encountered by boundary diffusion according to Grote-Hynes-theory. This will

be compared with recent results on local chain dynamics in different unstructured polypeptides. Moreover, we want to test whether friction is composed of an additive contribution of internal friction to solvent friction as was proposed in the literature (121-123).

With this TTET label spacing approach we also want to investigate the effect of capping motifs on helix stability and dynamics in the center. Recently, it was shown that stabilizing the ends of the helix by capping motifs affects helix unfolding but not refolding in the center (186). Up to date, it is unknown whether this non-local effect on helix stability in the center is attributed to an impact on the diffusion coefficient D for boundary diffusion, i.e. by increasing the activation energy, or due to different diffusion distances $\langle l^2 \rangle$ from the helix-coil boundary to the center. Hence, we aim to investigate the effect of stabilizing and destabilizing capping motifs at the N-cap and C-cap position on the diffusion coefficient for boundary diffusion and diffusion distances by TTET with an $i, i+2$ spacing of the labels. The results will be compared with calculations from Lifson-Roig (LR) theory for the helix-coil transition including N- and C-capping preferences. The LR model is additionally applied to predict the average diffusion distance in the different peptides more accurately.

3 Materials and Methods

All chemicals and solvents were purchased from Carl Roth (Karlsruhe, Germany), Sigma-Aldrich (St. Louis, MO, USA) or Merck (Darmstadt, Germany) if not stated otherwise. Urea was purchased from Gerbu Biotechnik GmbH (Heidelberg, Germany). Fmoc-protected amino acids were purchased from Novabiochem (Hohenbrunn, Germany) or Iris Biotech (Marktredwitz, Germany). Resins for solid phase peptide synthesis were purchased from Rapp Polymers (Tübingen, Germany) or Iris Biotech (Marktredwitz, Germany).

3.1 Peptide Synthesis and Purification

All peptides were synthesized by solid-phase peptide synthesis using standard fluorenylmethoxycarbonyl (Fmoc) chemistry on an Applied Biosystems 433A (ThermoFisher, Foster City, CA, USA) or Intavis MultiPep CF (Intavis, Cologne, Germany) synthesizer. Couplings were performed with 2-(1H-benzotriazole-1-yl)-*N,N,N',N'*-tetramethyluronium hexafluorophosphate (HBTU) and *N,N*-diisopropylethylamine (DIPEA) on a Tentagel R RAM resin (Rapp Polymers, Tübingen, Germany) in a 0.1 mmol scale. Double couplings were performed with a 10-fold excess of amino acid in *N*-methyl-2-pyrrolidone (NMP). Single couplings with a 5- or 10-fold excess were performed for the non-natural amino acids 1-L-naphthylalanine (Nal) and α,β -L-diaminopropionic acid (Dpr). Peptides with stabilizing end-capping motif (Suc, Aea) were synthesized on a Tentagel S FMP resin (Iris Biotech, Marktredwitz, Germany) preloaded with ethylenediamine (EDA) in a 0.1 mmol scale. Resin loading was achieved by reductive amination with a 10-fold excess of *tert*-butyloxycarbonyl-protected EDA and sodium cyanoborohydride (NaBH₃CN) in *N,N*-dimethylformamide (DMF) for 4 h at 25°C. Succinylation was done with a 10-fold excess of mono-*tert*-butyl succinate and HBTU/DIPEA as coupling reagents.

Deprotection of Fmoc was done in 20 % (v/v) piperidine in NMP or with 18 % (v/v) piperidine, 2 % (v/v) 1,8-diazabicyclo(5.4.0)undec-7-ene (DBU), 48 % (v/v) dimethyl sulfoxide (DMSO) in DMF. Fmoc deprotection was monitored by UV absorbance at 301 nm.

Preparative cleavage of the peptide from the resin was performed with 2.5 % (v/v) triisopropylsilane (TIPS) and 2.5 % (v/v) water in trifluoroacetic acid (TFA) for 3 hours at room temperature. The peptide was precipitated in ice-cold *tert*-butyl methyl ether and finally filtered (frit pore size 4). For purification 20 – 25 mg of the peptide pellet was

dissolved in < 1 mL pure TFA and diluted in 5 mL acetonitrile/water mixture. All peptides were purified to >95 % purity by reversed-phase HPLC (1200 series from Agilent Technologies, Santa Clara, CA, USA) in an acetonitrile/water gradient with 0.1 % (v/v) TFA on a RP-18 column (Phenomenex Kinetex XB-C18, 250 x 21 mm, 5 μ m or Merck LiChrospher 100, 250 x 25 mm, 4 μ m). Mass and purity of all peptides was verified by analytical HPLC and matrix-assisted laser desorption ionization-time of flight (MALDI-TOF) or electrospray ionization (ESI) mass spectrometry. Pure fractions were pooled, lyophilized and stored at -20 °C.

3.2 Peptide Modifications

Amidation of the peptide C-terminus was achieved by using Rink Amide (RAM) resins (Rapp Polymers, Tübingen, Germany). Acetylation of the peptide N-terminus was done on the resin three times for 10 minutes by 10 % (v/v) acetic anhydride (Ac₂O) and 10 % (v/v) DIPEA in DMF.

Succinylation of the N-terminus was obtained with a 10-fold excess of mono-*tert*-butyl succinate and HBTU/DIPEA as coupling reagents whereas a C-terminal 2-aminoethylamide was achieved by reductive amination of a Tentagel S 4-formyl-3-methoxy phenoxyethyl (FMP) resin with EDA (Iris Biotech, Marktredwitz, Germany).

Introduction of the TTET labels was performed by incorporation of the non-natural amino acids α,β -L-diaminopropionic acid (Dpr) and 1-L-naphthylalanine (Nal). 9-Oxoxanthen-2-carboxylic acid (Xan) was synthesized as described and attached to the β -amino group of Dpr after selective removal of the *N*-methyltrityl (Mtt) group with 2 % (v/v) TFA and 2 % (v/v) TIPS in dichloromethane (DCM) for 10 minutes (218). Mtt deprotection was repeated at least 3 times. Coupling of Xan was performed for 1 hour with a 3-fold excess and HBTU/*N*-methylmorpholine (NMM) as coupling reagents in DMF.

3.3 Sample Preparation and Concentration Determination

All measurements were performed in 10 mM potassium phosphate buffer, pH 7.0. All buffers and samples were filtered with a pore size of 0.2 μ m. The peptide concentration was determined by absorbance of xanthone on a diode array absorbance spectrometer (Agilent technologies, Santa Clara, CA, USA and Analytik Jena AG, Jena, Germany) with an extinction coefficient of $\epsilon_{343\text{nm}} = 3900 \text{ M}^{-1} \text{ cm}^{-1}$.

Urea concentrations were determined by the refractive index in the presence n_D and absence n_0 of denaturant on a automatic refractometer AR7 Series (Reichert, Depew, NY, USA) according to Pace (10) (Eq. 3.1).

$$c_{urea} = (n_D - n_0) \cdot 117.66 \frac{mol}{L} + (n_D - n_0)^2 \cdot 29.753 \frac{mol}{L} + (n_D - n_0)^3 \cdot 185.56 \frac{mol}{L} \quad (3.1)$$

Solvent viscosities and density were determined with a rolling-ball microviscometer Lovis 2000 M/ME (Anton Paar, Graz, Austria) at 5 °C.

3.4 Laser Flash Photolysis

TTET measurements were performed on a Laser Flash Reaction Analyzer (LKS.60) from Applied Photophysics (Leatherhead, Surrey, UK). Xanthone as triplet donor was excited to the triplet state selectively by using a Quantel (Les Ulis, France) (354.6 nm, 4 ns pulse of 50 mJ) or InnoLas (Krailling, Germany) Nd:YAG-Laser (354.6 nm, 7 ns pulse of 70 mJ). Transient triplet absorbance data were recorded on an Agilent infinium oscilloscope with 600 MHz and 4 GSa/s (500 MHz and 20 GSa/s) on a logarithmic time base. The transient triplet absorbance decay data of Xan were recorded at 590 nm and 4 – 6 traces were averaged. TTET was controlled by recording transient triplet absorbance rise data of Nal at 420 nm. The kinetics were analyzed using ProFit (Quansoft, Zürich, Switzerland). All measurements were performed in degassed solutions with 10 mM potassium phosphate buffer, pH 7.0 between 5 – 40 °C with a peptide concentration of 50 μ M ($\epsilon_{343nm} = 3900 \text{ M}^{-1} \text{ cm}^{-1}$). All traces were normalized to a peptide concentration of 50 μ M. Xanthonic acid was measured as a reference and all traces were finally normalized to the amplitude of 50 μ M xanthonic acid to compensate for differences in laser energies.

The TTET experiments show double exponential kinetics, which can be described by a three-state model (Eq. 1.21). Accordingly, the analytical solution of the three-state model (Eq. 3.2-3.4) is used to obtain the microscopic rate constants for folding k_f , unfolding k_u and contact formation k_c by using the observable rate constants $\lambda_{1/2}$ and their corresponding amplitudes $A_{1/2}$ (170, 213, 219). An urea dependence of the TTET kinetics is performed and the data are fitted globally to determine the microscopic rate constants more reliably. For the global analysis a linear effect of urea on $\ln k_f$, $\ln k_u$ and $\ln k_c$ was assumed (Eq. 1.20) (14, 64, 68, 220).

$$\lambda_{1,2} = \frac{k_u + k_f + k_c \pm \sqrt{(k_u + k_f + k_c)^2 - 4k_u \cdot k_c}}{2} \quad (3.2)$$

$$A_1 = \frac{1}{\lambda_1(\lambda_1 - \lambda_2)} \left([U]_0 \cdot k_c (k_u - \lambda_1) + [N]_0 \cdot k_u \cdot k_c \right) \quad (3.3)$$

$$A_2 = \frac{1}{\lambda_2(\lambda_1 - \lambda_2)} \left([U]_0 \cdot k_c (\lambda_2 - k_u) - [N]_0 \cdot k_u \cdot k_c \right) \quad (3.4)$$

3.5 Circular Dichroism Spectroscopy

The secondary structure of all peptides was determined by far-UV CD spectroscopy in a 0.1 cm cuvette at 5 °C with a peptide concentration of 50 μM carried out on a AVIV 410 spectropolarimeter (AVIV, Lakewood, NJ, USA). Thermal unfolding transitions were measured between 5 and 95 °C at 222 nm in a 1 cm cuvette with a peptide concentration of ~ 10 μM. The mean residue molar ellipticity $[\Theta]_{MRW}$ was determined by

$$[\Theta]_{MRW} = \frac{100 \cdot \Theta}{c \cdot l \cdot N_{aa}} \left[\text{deg} \cdot \text{cm}^2 \cdot \text{dmol}^{-1} \right] \quad (3.5)$$

where Θ is the CD signal in degree, c the molar concentration in mol/L, l the pathlength in cm and N_{aa} the number of amino acids.

3.6 Determination of the Average Position of the Helix-Coil Boundary

The modifications of the Lifson-Roig theory to include N- and C-capping effects as described by Doig *et al.* was applied to determine the effect of different capping motifs on the average diffusion distance $\langle l^2 \rangle$ from the helix-coil boundary to the helix center (178). The Lifson-Roig parameters for the alanine-based helices were taken from Rohl *et al.* (162) (Tab. 3.1). The capping parameters (n , c) for succinyl and 2-aminoethylamide (Aea) were assumed to be 4-fold and 3-fold increased compared to the capping parameters of acetyl and amide (Tab. 3.1). The propagation parameter w of the TTET labels was assumed to be similar to tryptophan (Nal) and glutamine (Xan) by considering only the number of freely rotating bonds (Tab. 1.1). The matrix products were calculated without any further approximations using MATLAB_R2016b (MathWorks, Natick, MA, USA).

The average position of the helix-coil boundary was the weighted mean of all probabilities (Eq. 3.6).

$$\sum_{i=1}^n p_i \cdot x_i = (p_1 \cdot x_1 + \dots + p_n \cdot x_n) \quad (3.6)$$

Either the shortest diffusion distance to the helix center or the average distance from both termini was considered. For the temperature dependence an enthalpy change of the propagation parameter w with temperature of $\Delta H = 4200 \text{ J mol}^{-1}$ per residue was assumed according to Scholtz *et al.* (160). All other parameters are temperature independent and were not changed.

Table 3.1: Statistical weights for helix propagation, nucleation and capping for all used residues at 273 Kelvin.

amino acid	w -value	ν -value	n -value	c -value
Alanine	1.70	0.036	1.00	1.00
Arginine	1.14	0.036	1.00	2.10
Xanthone	0.60	0.036	1.00	1.00
Naphthylalanine	0.29	0.036	1.00	1.00
Acetyl	1.00	0.036	5.90	1.00
Amide	1.00	0.036	1.00	1.30
Succinyl	1.00	0.036	23	1.00
2-aminoethylamide	1.00	0.036	1.00	4.00

The statistical weights for alanine, arginine, acetyl and amide residues were taken from Rohl *et al.* (162). The c -values were adapted from Doig & Baldwin (176).

4 Results and Discussion

4.1 Determination of the Diffusion Coefficient for Boundary Diffusion in α -Helices

4.1.1 Effect of the Diffusion Distance on the Diffusion Coefficient for Boundary Diffusion

Previous results demonstrated that helix-coil dynamics can be understood as a classical, Einstein-type, 1-D boundary diffusion mechanism which leads to a position- and length-dependent rate constant for helix unfolding k_u (170, 186). The survival probability for the helix in the center is affected by two moving helix-coil boundaries, one boundary from each side of the helical segment, respectively. Thus, the survival probability S for the helix in the center can be approximated by two identical processes at a time with

$$S_2(t) \approx e^{-\frac{4Dt}{l^2}} \quad \text{or} \quad \left(S_1(t) \approx e^{-\frac{2Dt}{l^2}} \right)^2 \quad (4.1)$$

where the index denotes the number of independent moving helix-coil boundaries (186). Consequently, the diffusion coefficient D for one boundary is obtained by a modified Einstein equation which correlates the diffusion distance $\langle l^2 \rangle$ with the required helix unfolding time $1/k_u$ of both boundaries to reach the helix center (Eq. 4.2).

$$\langle l^2 \rangle \approx \frac{4D}{k_u} \quad (4.2)$$

A linear relationship of $\langle l^2 \rangle$ vs. $1/k_u$ demonstrates that helix-coil boundary diffusion follows a classical, 1-D diffusion law (Fig. 4.1). The diffusion coefficient is obtained from the slope and yields $D = 2.7 \cdot 10^7$ (amino acids)² s⁻¹ or $6.1 \cdot 10^{-9}$ cm² s⁻¹ (Eq. 4.2). In this study, the terminal amino acids were considered as coil and an average position of the boundaries at position 2 and $n-1$ was assumed for the calculations (Tab. 4.1).

In these experiments a TTET label spacing of $i, i+6$ was used and it was assumed that four helical segments between the labels in the center have to unfold in order to enable TTET (Fig. 4.2) (186). However, it is not exactly known, how many segments have to be unfolded to enable triplet transfer between Xan and Nal. Consequently, there is an uncertainty in defining the diffusion distance and hence in the diffusion coefficient.

Table 4.1: Sequences and diffusion distances of α -helical peptides of different length with $i,i+6$ TTET label spacing.

Peptide	Sequence (N \rightarrow C)	$\langle l^2 \rangle$
16aa	Ac-AAAAXAAARAZAARAA-NH ₂	81
21aa	Ac-AAAAAXARAAAZRAAAARAA-NH ₂	121
31aa	Ac-AAAAAAAAARAAXARAAAZRAA(AARAA) ₂ -NH ₂	256
41aa	Ac-AAAAAA(AARAA) ₂ XARAAAZRAA(AARAA) ₃ -NH ₂	441

X = xanthone, Z = naphthylalanine, Ac = acetyl, NH₂ = amide. Data according to Neumaier *et al.* (186).

Figure 4.1 illustrates the problem of defining the correct diffusion distance and its effect on the diffusion coefficient. Here, three different possibilities for TTET from the N-terminus are assumed and the last amino acid is considered as coil. The longest diffusion distance (red) represents a complete unfolding to Nal, a mean diffusion distance (orange) for unfolding of three helical segments between the labels and the shortest diffusion distance (green) when unfolding to Xan is sufficient for TTET (Fig. 4.1, Tab. 4.1). Depending on the diffusion distance, the diffusion coefficient is almost doubled from $3.5 \cdot 10^{-9} \text{ cm}^2 \text{ s}^{-1}$ for short distances to $6.1 \cdot 10^{-9} \text{ cm}^2 \text{ s}^{-1}$ for long distances.

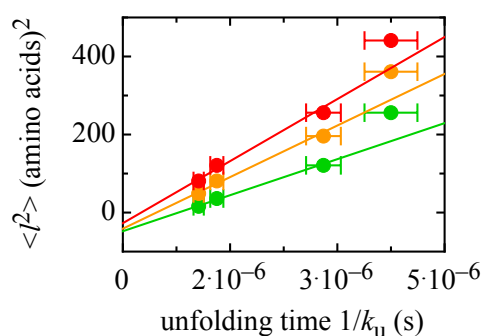


Figure 4.1: Correlation between the distance of boundary diffusion and the time constant for helix unfolding for different diffusion distances. Effect of different diffusion distances $\langle l^2 \rangle$ on the diffusion coefficient D for boundary diffusion in peptides with $i,i+6$ spacing of the TTET labels. The average diffusion distances, l , of the boundaries were calculated between position 2 and the C-terminal label (Nal) given as numbers of amino acids (red), between position 2 and three amino acids after the N-terminal label (Xan) (orange) and between position 2 and the N-terminal label (Xan) (green). The different plots of $\langle l^2 \rangle$ vs. $1/k_u$ are linear, indicating that boundary diffusion can be described by equation 4.1. The solid line represents a fit of equation 4.2 to the data for the three shortest helices with $D = 3.5 \pm 0.5 \cdot 10^{-9} \text{ cm}^2 \text{ s}^{-1}$ (green), $D = 5.0 \pm 0.7 \cdot 10^{-9} \text{ cm}^2 \text{ s}^{-1}$ (orange) and $D = 6.1 \pm 0.9 \cdot 10^{-9} \text{ cm}^2 \text{ s}^{-1}$ (red) at 5 °C.

Moreover, simulations revealed that unfolding in the central region of the helix contains increasing contributions from coil nucleation with increasing helix length (186). This mechanism occurs in addition to boundary diffusion and increases the observed rate constant for helix unfolding, which is demonstrated by the deviation from linearity at a

helix length of 41 amino acids (aa) (Fig. 4.1). The probability of coil nucleation events in the central region of a helix with 31 aa is about 20 % (186). This makes it rather difficult to suggest an appropriate diffusion distance especially for longer peptides and consequently leads to an error-prone diffusion coefficient. Furthermore, the negative offset on the y-axis indicates that the diffusion distances might be overestimated for longer helices or underestimated for all helices.

For this reason, a different label spacing approach of $i,i+2$ was applied to decrease the uncertainty in the diffusion distance and thus give a more reliable diffusion coefficient for boundary diffusion (Fig. 4.2). Moreover, the labels are still on opposite sides of the helix and prevent TTET in the folded helical state. It is also expected that this spacing has less contribution from coil nucleation events between the labels and thus yield more reliable results on k_u , k_f and the diffusion coefficient for boundary diffusion.

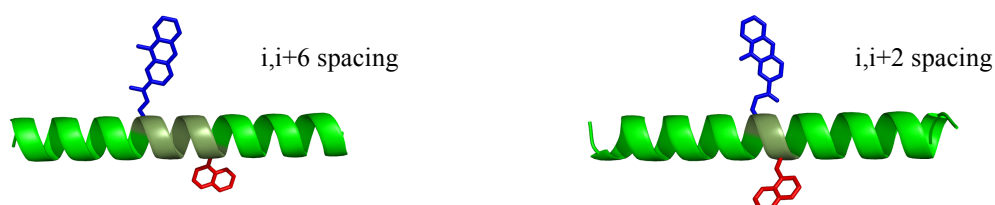


Figure 4.2: Comparison of the $i,i+6$ and $i,i+2$ TTET label spacing. Xanthone is shown in blue and naphthalene in red. In the $i,i+2$ spacing approach is only one amino acid between the labels (dark green) and the peptides are symmetric with same distances on both sides of the labels. This approach is more sensitive to TTET by boundary diffusion than the $i,i+6$ spacing approach which probes a region of five residues between the labels (dark green) (pictured by MacPyMOL).

4.1.2 Effect of Peptide Length on Helix Folding and Unfolding Dynamics with $i,i+2$ Spacing

Helix folding and unfolding dynamics were studied in alanine-based helical peptides of different length between 11 aa and 41 aa with central TTET labels and $i,i+2$ spacing (Fig. 4.3, Tab. 4.2). Compared to the previous study on $i,i+6$ peptides, more peptides between a length of 21 aa and 31 aa were used to provide more data points with less contributions of coil nucleation (186). Arginine residues were introduced with an $i,i+5$ spacing to increase the solubility of the peptides (Tab. 4.2).

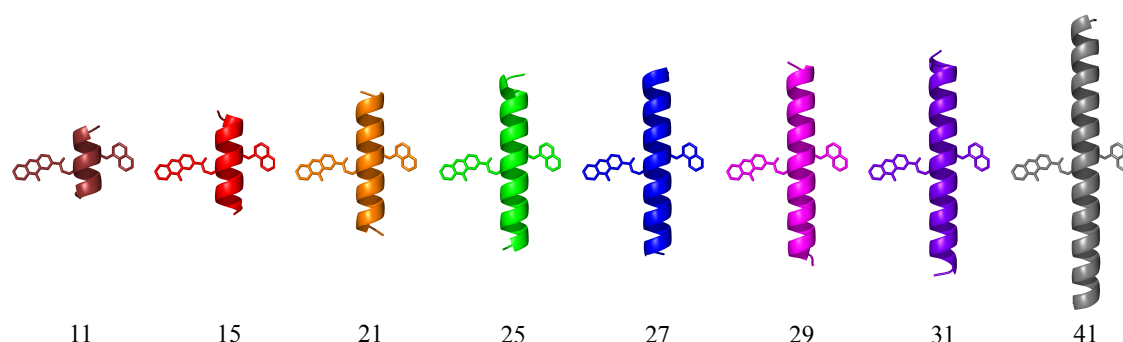


Figure 4.3: Alanine-based helical peptides of different length with central TTET labels. Peptides with $i,i+2$ spacing of the TTET labels were used to determine the diffusion coefficient for boundary diffusion more accurately. The colors in the plots of figure 4.4 correspond to the colors of the peptides.

Table 4.2: Sequences and diffusion distances of α -helical peptides of different length with $i,i+2$ TTET label spacing.

Peptide	Sequence (N \rightarrow C)	$\langle r^2 \rangle$
11aa	Ac-AAARXAZARAA-NH ₂	9
15aa	Ac-AAAAARXAZARAAAA-NH ₂	16
21aa	Ac-AAAAAAARXAZARAAAARAA-NH ₂	81
25aa	Ac-AAAAARAAAARXAZARAAAARAAAA-NH ₂	121
27aa	Ac-AAAAARAAAARXAZARAAAARAAAAR-NH ₂	144
29aa	Ac-AAAAARAAAARXAZARAAAARAAAARA-NH ₂	169
31aa	Ac-AAAAARAAAARXAZARA(AAARA) ₂ A-NH ₂	196
41aa	Ac-AAAA(AAARA) ₂ AAARXAZARA(AAARA) ₃ A-NH ₂	361

$\langle r^2 \rangle$ = diffusion distance, X = xanthone, Z = naphthylalanine, Ac = acetyl, NH₂ = amide.

The secondary structure of all peptides was determined by circular dichroism (CD) spectroscopy (Fig. 4.4). The far-UV CD spectra of almost all peptides show typical helical CD bands indicated by a maximum in ellipticity at 190 nm and minima at 208 nm and 222 nm. Shorter peptides with 11 aa and 15 aa represent rather instable helices as displayed by a minimum at 200 nm (221) (Fig. 4.4A). The TTET labels with an $i,i+2$

spacing in the center potentially destabilize shorter peptides more strongly than longer peptides, which is in agreement with Lifson-Roig theory and previous experiments (168, 186). Although the average helix content in these peptides is low, they still yield reliable results on the rate constants for helix folding k_f and unfolding k_u in the center. A quantitative analysis of the helix content based on the CD signal at 222 nm is not possible due to absorbance of the TTET labels in the far-UV region (170). However, the increase in the CD band at 222 nm with increasing peptide length demonstrates a higher average helical content and consequently implies longer helices in longer peptides. The peptides with $i,i+2$ spacing show a similar helix content as compared with the $i,i+6$ spacing (186). This demonstrates that the $i,i+2$ spacing of the TTET labels in the helix center has no additional destabilizing or stabilizing effect on helicity compared with $i,i+6$ except for short peptides (Fig. 4.4A).

The TTET kinetics were monitored by the triplet absorbance decay of xanthone at 590 nm (Fig. 4.4B). Triplet transfer to naphthalene was verified by the rise of the triplet absorbance band at 420 nm (Fig. A1). All peptides show double exponential kinetics, which is in agreement with the three-state model and indicates that both the helical and coil state are populated to significant amount at equilibrium (Eq. 1.21). There is an additional kinetic phase with less than 10 % in amplitude more frequently observed in longer helices, which potentially arise from aggregated peptides or a folded subpopulation (Fig. A1) (see section 4.3). This fraction of peptides was not included into the global analysis.

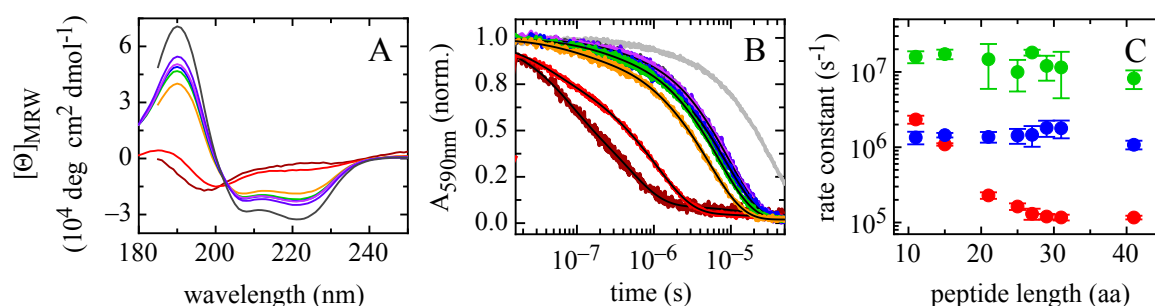


Figure 4.4: Effect of peptide length on helix-coil dynamics and stability in the helix center. The colors in the plots correspond to the colors of the peptides in figure 4.3. (A) Far-UV CD spectra of the different peptides. (B) TTET kinetics monitored by the triplet absorbance of xanthone at 590 nm. The grey line represents the triplet lifetime for a donor-only peptide as reference. The black lines represent triple-exponential fits to the kinetics. (C) A global fit of the urea dependence data using the analytical solution of the three-state model yielded the rate constant for helix folding k_f (blue), unfolding k_u (red) and contact formation k_c (green). All experiments were performed at 5 °C.

Figure 4.4B shows that TTET in the central region of the helix becomes slower with increasing length of the peptide but is still faster than the spontaneous triplet decay of the donor (grey trace). Moreover, smaller amplitudes of the TTET kinetics are observed especially in short, instable peptides with respect to donor-only traces (Tab. 4.3, Fig. A1). This missing amplitude is caused by a fraction of unfolded peptides that already have *van-der-Waals* contact between Xan and Nal within laser excitation. This effect is taken into account in the global analysis by addition of the missing amplitude to the amplitude of the fast TTET process which mainly represents TTET from the unfolded state [U_0] (Eq. 3.2-3.4) (186). The urea dependence of the TTET kinetics of each peptide were fitted globally using the analytical solution of the three-state model to obtain the rate constant for helix unfolding k_u , helix folding k_f and contact formation k_c (Eq. 3.2-3.4, Fig 4.5) (64, 170, 186, 219). For the global analysis a linear effect of urea on $\ln k_f$, $\ln k_u$ and $\ln k_c$ was assumed (Eq. 1.20) (14, 64, 68, 220) (see section 3.4). The corresponding plot of the rate constant for helix folding k_f , unfolding k_u and contact formation k_c with respect to helix length is shown in figure 4.4C. The rate constants for helix unfolding and folding in the helix center show the same length-dependence as already observed with $i,i+6$ (186). The rate constant for helix unfolding is length-dependent and decreases with the length of the helix from $1/k_u = 430$ ns to $9 \mu\text{s}$ whereas the rate constant for helix folding is length-independent with $1/k_f = 650$ ns which is in agreement with a 1-D boundary diffusion mechanism (186). However, above a helix length of 29 aa k_u becomes length-independent as well suggesting a change in the rate-limiting step for helix unfolding. Consequently, the peptide stability in the center K_{eq} increases with increasing length until a helix length of 31 aa (Tab. 4.3). This increase in stability was also observed by thermal unfolding transitions monitored by CD spectroscopy at 222 nm which, in contrast to TTET, probes the global helix content (Fig. A5). The rate constant for contact formation in the center also decreases with the length of the peptide. This is in accordance with results from loop formation kinetics in unfolded polypeptide chains, which showed that the dynamics of loop formation are coupled to motions of other chain segments and depend on the overall chain dimension (78). Thus, loop formation is faster at the chain ends than in the interior of the chain because of differences in internal flexibility at the different positions in a polypeptide chain.

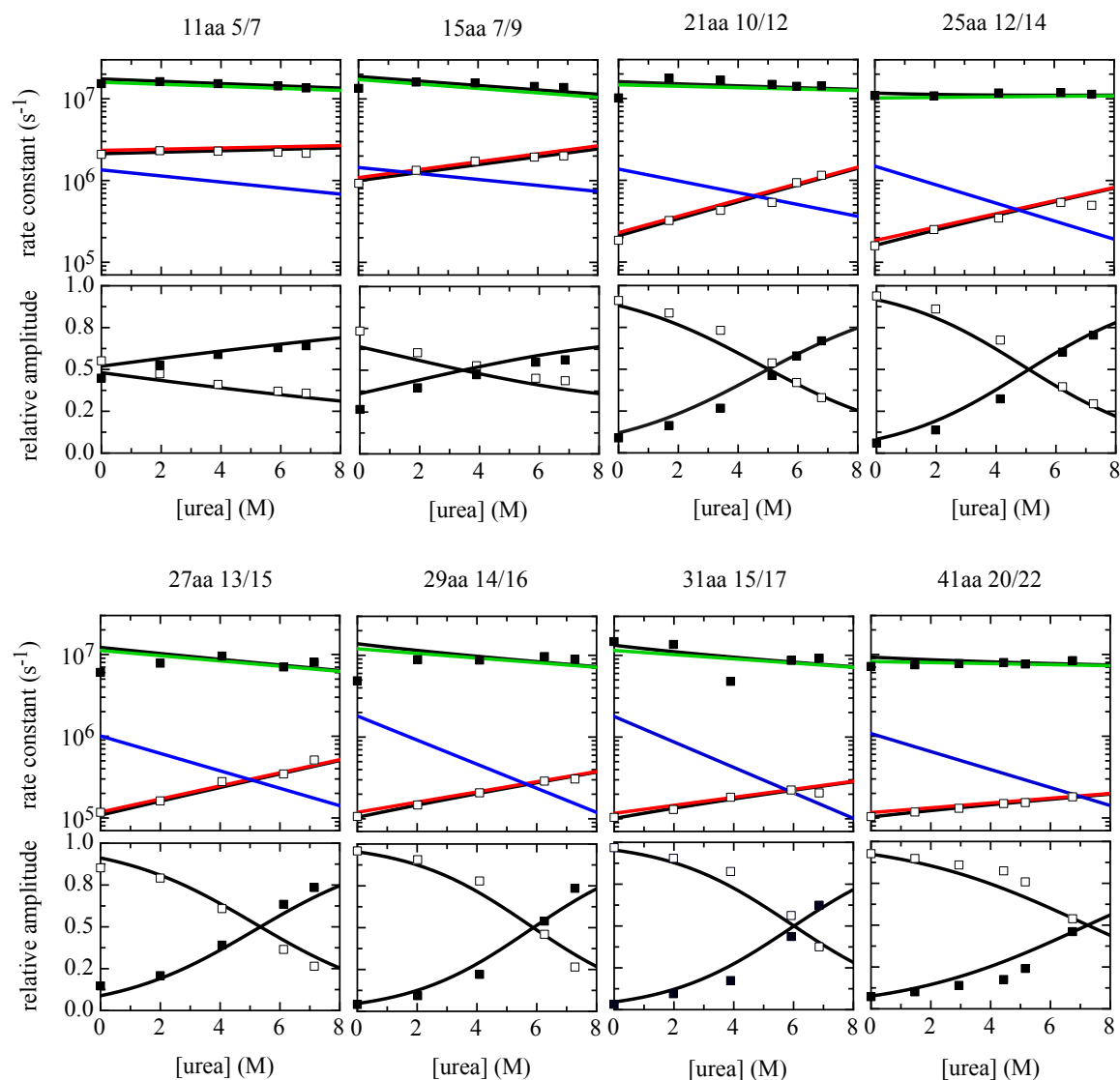


Figure 4.5: Urea dependence of helix-coil dynamics in the center of helical peptides of different length. The peptides were labeled in the center with an $i,i+2$ spacing. The squares represent the observable rate constants $\lambda_{1,2}$ and relative amplitudes $A_{1,2}$ obtained from individually fitting each kinetic trace. A global fit of the observable rate constants $\lambda_{1,2}$ (black lines) and amplitudes $A_{1,2}$ (black lines) using the analytical solution of the three-state model yields the rate constant for helix folding k_f (blue line), unfolding k_u (red line) and contact formation k_c (green line). All experiments were performed in 10 mM potassium phosphate buffer, pH 7.0 at 5 °C.

Table 4.3: Effect of helix length on stability and dynamics in the central region of helical peptides with respect to urea.

Peptide Label pos.	k_u (10^5s^{-1})	k_f (10^6s^{-1})	k_c (10^6s^{-1})	m_u ($\text{J mol}^{-1} \text{M}^{-1}$)	m_f ($\text{J mol}^{-1} \text{M}^{-1}$)	m_c ($\text{J mol}^{-1} \text{M}^{-1}$)	K_{eq}	A_{miss} (%)	Θ 222 nm ($\text{deg cm}^2 \text{dmol}^{-1}$)
11aa 5/7	23.37 ± 2.8	1.35 ± 0.3	15.92 ± 2.9	-39 ± 13	197 ± 18	66 ± 11	0.58 ± 0.1	61	-2456.6
15aa 7/9	10.89 ± 0.4	1.45 ± 0.1	17.26 ± 2.5	-259 ± 7	195 ± 10	145 ± 8	1.33 ± 0.1	60	-6077.5
21aa 10/12	2.33 ± 0.2	1.21 ± 0.1	15.88 ± 6.6	-580 ± 8	237 ± 12	188 ± 18	5.19 ± 0.6	29	-19740.3
25aa 12/14	1.63 ± 0.2	1.43 ± 0.3	9.97 ± 4.5	-517 ± 8	546 ± 19	-30 ± 28	8.77 ± 2.0	27	-21832.9
27aa 13/15	1.31 ± 0.2	1.46 ± 0.5	18.10 ± 1.6	-472 ± 15	549 ± 21	205 ± 42	11.2 ± 3.4	29	-22774.7
29aa 14/16	1.20 ± 0.1	1.81 ± 0.4	12.03 ± 4.4	-332 ± 9	785 ± 19	151 ± 29	15.1 ± 3.7	20	-22810.3
31aa 15/17	1.17 ± 0.1	1.79 ± 0.5	11.49 ± 7.0	-261 ± 10	829 ± 20	138 ± 37	15.3 ± 4.1	12	-24795.5
41aa 20/22	1.17 ± 0.1	1.08 ± 0.1	8.20 ± 2.3	-156 ± 6	586 ± 10	34 ± 26	9.26 ± 1.2	0	-32534.3

The CD signal at 222 nm is indicative for the overall helical content and is given in units of $\text{deg} \cdot \text{cm}^2 \cdot \text{dmol}^{-1}$. m_u , m_f and m_c are the urea dependencies of $\ln k_u$, $\ln k_f$ and $\ln k_c$ respectively, multiplied by RT (see eq. 1.20) (64). A_{miss} denotes the dead time absorbance change with respect to the donor-only reference.

The urea dependence of the rate constant for contact formation k_c is independent of the helix length as was shown in previous studies with $m_c \approx 130 \text{ J mol}^{-1} \text{ M}^{-1}$ indicating that the change in solvent accessible surface area (ΔSASA) upon contact formation is similar for all peptides (Fig. 4.6A) (14, 64, 170, 186). In contrast, the urea dependence of k_u and k_f is more complex. The m_f -value is positive and increases with helix length until 31 aa whereas m_u is negative and decreases with length until 21 aa and then increases in longer and stable helices (Fig. 4.6A). However, the ΔSASA between the coil (C) and helical (H) state upon unfolding can be expressed with the m_{eq} -value ($m_{\text{eq}} = m_f - m_u$) (69). Figure 4.6B shows that ΔSASA upon unfolding increases with helix length until 29 aa and then decreases again. The increase in ΔSASA upon unfolding might be due to an increase in unfolded regions in longer helices. The decrease in ΔSASA at 31 aa suggests increased coil nucleation events above a helix length of 31 aa and an increased equilibrium fraction of peptides with two separate helices (186). This is in agreement with the peptide stability in the helix center K_{eq} which also decreases at a length of 31 aa (Tab. 4.3). However, the m_{eq} -value in this case is only an apparent value and does not correlate with the ΔSASA between C and H of the elementary step because the rate constants k_f and k_u represent helix folding and unfolding dynamics in the region between the TTET labels.

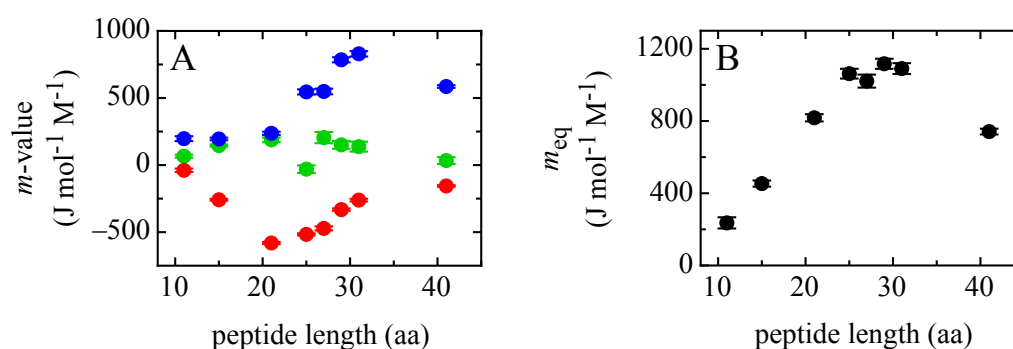


Figure 4.6: Effect of helix length on the denaturant m -values of helix folding, unfolding and contact formation. (A) Dependence of m_u (red), m_f (blue), and m_c -values (green) on helix length. (B) The m_{eq} -value ($m_{\text{eq}} = m_f - m_u$) with respect to helix length. The change in solvent accessible surface area (ΔSASA) upon unfolding correlates with m_{eq} and increases with helix length until 31 aa.

4.1.3 Comparison of the Diffusion Coefficient for Boundary Diffusion with $i,i+2$ and $i,i+6$ Spacing

The diffusion coefficient for boundary diffusion with $i,i+2$ spacing of the TTET labels is calculated by equation 4.2 as described before. A plot of the squared average diffusion distance $\langle l^2 \rangle$ against the unfolding time $1/k_u$ for each peptide results in a linear relationship confirming that helix-coil dynamics in these peptides also follow a classical, Einstein-type, 1-D diffusion law (Fig. 4.7). The N- and C-terminal residues were considered to be in a non-helical conformation and the average position of the helix-coil boundary was assumed at position 2 and $n-1$ (with n number of aa) (Tab. 4.2) (168, 170, 186-188). Shorter diffusion distances were considered for the two instable helices with 11 aa and 15 aa (Fig. 4.4A). Here, the average position of the helix-coil boundary was assumed at position 3 or 4 and $n-2$ or $n-3$ (Tab. 4.2). Furthermore, we considered that unfolding to the first TTET label is sufficient for enabling TTET. Due to the fact that the peptides are symmetric in length, it does not matter whether unfolding occurs from the C- or N-terminus. The slope of the plot is $1.9 \cdot 10^7 \text{ aa}^2 \text{ s}^{-1}$ and yields an upper diffusion coefficient for one boundary of $D = 4.8 \pm 0.3 \cdot 10^6 \text{ aa}^2 \text{ s}^{-1}$ or $1.07 \pm 0.07 \cdot 10^{-9} \text{ cm}^2 \text{ s}^{-1}$ with a y-intercept of zero (Fig. 4.7, Eq. 4.2). The y-intercept demonstrates that the $i,i+2$ approach is more accurate with respect to the diffusion distances $\langle l^2 \rangle$ and helix unfolding times $1/k_u$ as compared to the $i,i+6$ approach (Fig. 4.7). Only helices shorter than 29 aa were considered in this calculation because of increasing contributions of coil nucleation events

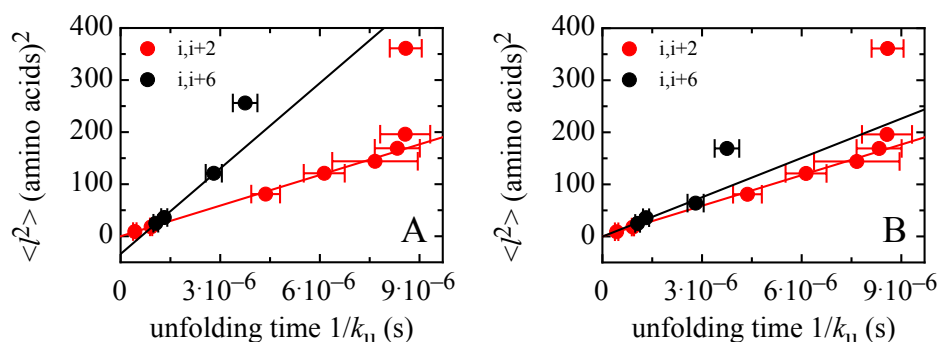


Figure 4.7: Correlation between the distance of boundary diffusion and the time constant for helix unfolding for $i,i+6$ and $i,i+2$. Effect of TTET label spacing on the diffusion coefficient for boundary diffusion. (A) The average diffusion distances, l , of the boundaries in peptides with $i,i+2$ spacing (red) were calculated between position $n-1$ and the C-terminal label (Nal) and in peptides with $i,i+6$ spacing (black) were calculated between position 2 and the N-terminal label (Xan). (B) Additionally, for the helix with 31 aa and 41 aa a short diffusion distance of 8 aa and 13 aa was considered. Both plots of $\langle l^2 \rangle$ vs. $1/k_u$ are linear, indicating that boundary diffusion can be described by equation 4.1. The solid line represents a fit of equation 4.2 to the data with $D = 1.1 \pm 0.1 \cdot 10^{-9} \text{ cm}^2 \text{ s}^{-1}$ (red) and $D = 3.5 \pm 0.5 \cdot 10^{-9} \text{ cm}^2 \text{ s}^{-1}$ (black) (A) or $D = 1.4 \pm 0.2 \cdot 10^{-9} \text{ cm}^2 \text{ s}^{-1}$ (black) at 5°C (B).

at a helix length of 31aa which leads to a deviation from linearity (Fig. 4.7).

Based on the results from the $i,i+2$ approach, it is possible to interpret the results from $i,i+6$ by reevaluating the diffusion distances. A comparison of the results from $i,i+2$ and $i,i+6$ reveals a 6 times smaller diffusion coefficient in peptides with $i,i+2$ spacing. However, in peptides with $i,i+6$ spacing we assume that four helical segments between the labels have to unfold to enable TTET. Considering a diffusion distance to the first TTET label in the $i,i+6$ approach as described above yields $D = 3.5 \pm 0.5 \cdot 10^{-9} \text{ cm}^2 \text{ s}^{-1}$, which is still 3 times larger than $i,i+2$ (Fig. 4.7A). However, the $i,i+6$ spacing approach yields a similar diffusion coefficient with $D = 1.4 \pm 0.2 \cdot 10^{-9} \text{ cm}^2 \text{ s}^{-1}$ and a y-intercept of zero when additionally a very short diffusion distance is considered for the helix of 31 aa where the diffusion distance might be overestimated (Fig. 4.7B). This overestimation is further clarified in the $i,i+2$ approach, where the helix unfolding time deviates from linearity at helices longer than 29 aa and by the decrease in m_{eq} values at 31 aa (Fig. 4.7, Fig. 4.6B). Thus, helices with 31 aa contain increasing contributions from coil nucleation events and TTET is not predominantly enabled by boundary diffusion at this length. Consequently, the diffusion distance was overestimated in $i,i+6$ and resulted into a larger diffusion coefficient with a negative offset on the y-axis (186).

The time constant for the elementary step of helix growth $1/k_1$ and shrinking $1/k_{-1}$ can be determined experimentally from the diffusion coefficient when we assume an unbiased one-dimensional random walk of the helix-coil boundary along the peptide backbone (Eq. 4.3).

$$\tau = \frac{\delta^2}{2D} \quad (4.3)$$

Here, δ is the propagation distance in amino acids, D is the diffusion coefficient in $\text{aa}^2 \text{ s}^{-1}$ and τ is the time required for each propagation step in seconds. Using the diffusion coefficient of the $i,i+2$ approach yields an elementary time constant for helix growth and shrinking by one amino acid of $1/k \approx 100 \text{ ns}$. However, simulations based on the linear Ising model yielded values of $1/k_1 \approx 50 \text{ ns}$ and $1/k_{-1} \approx 65 \text{ ns}$ which is a factor of 2 faster than determined experimentally from the diffusion coefficient (170). This difference might be explained by the fact that the helix-coil boundary follows a biased one-dimensional random walk where the probability of helix growth and shrinking is not equal. Nevertheless, simulations on the length-dependence of helix-coil dynamics

revealed elementary steps of $1/k_1 = 83$ ns and $1/k_{-1} = 98$ ns which is close to the value determined experimentally (186). Another possibility might be that the peptides with $i,i+2$ spacing follow a different one-dimensional diffusion law where diffusion from two sides of the helical segment is not explicitly true and we do not observe two identical processes at a time. Accordingly, the prefactor in the modified Einstein equation (Eq. 4.4) changes to a value between 4 and 2 which results in an upper limit for the diffusion coefficient of boundary diffusion of $D = 9.5 \pm 0.6 \cdot 10^6$ aa² s⁻¹ or $2.13 \pm 0.14 \cdot 10^{-9}$ cm² s⁻¹.

$$\langle l^2 \rangle \approx \frac{4D}{k_u} \quad (4.4)$$

Hence, the elementary process of adding and removing helical segments occurs with a time constant of $1/k \approx 100 - 50$ ns which is in good agreement with previous simulations (170, 186).

Concluding, the $i,i+2$ spacing approach is well suited to determine the diffusion coefficient for boundary diffusion more accurately as the diffusion distance is better defined and TTET is primarily caused by boundary diffusion.

4.2 Energetics of the Boundary Diffusion Mechanism

4.2.1 Effect of Solvent Viscosity on Boundary Diffusion

Boundary diffusion is 2 to 3 orders of magnitude slower in comparison with free diffusion of small molecules and globular proteins. Sucrose, for example, has a diffusion coefficient of $D = 2.5 \cdot 10^{-6} \text{ cm}^2 \text{ s}^{-1}$ whereas ribonuclease and lysozyme have diffusion coefficients of about $D = 7 \cdot 10^{-7} \text{ cm}^2 \text{ s}^{-1}$ at 5 °C (222). However, free diffusion and 1-D diffusion within a polypeptide chain cannot be compared directly because of different degrees of freedom. Moreover, a 1-D diffusion along the peptide backbone might be limited by the sterics of bond rotations which suggests that boundary diffusion is slowed down by local energy barriers. On the basis of the $i, i+2$ spacing approach, we are able to characterize the boundary diffusion process in more detail and to test whether boundary diffusion is purely diffusion-controlled or encounters energy barriers arising from intramolecular interactions such as hydrogen bonds or steric effects from bond rotations.

According to the Stokes-Einstein law, a fully diffusion-controlled reaction is inversely proportional to the solvent viscosity ($D \propto 1/\eta$) and directly proportional to the temperature ($D \propto k_B T$) with an activation energy close to zero ($E_a = 0$) (214-216) (Eq. 4.5).

$$D = \frac{k_B T}{6\pi \cdot \eta \cdot r_s} \quad (4.5)$$

In this equation, $k_B T$ is the thermal energy of the system where k_B is the Boltzmann constant and T the absolute temperature. The impact of friction on diffusion is related to the solvent viscosity η and the radius r_s of a spherical particle. D represents in our case the diffusion coefficient for boundary diffusion. We studied the effect of solvent viscosity η on the diffusion coefficient D for boundary diffusion, to test whether boundary diffusion is purely diffusion-controlled or limited by intrinsic energy barriers. Furthermore, we can use the solvent viscosity dependence of the diffusion coefficient to correct for the decrease in solvent viscosity with temperature (Eq. 4.7).

Generally, the effect of solvent viscosity on the diffusion coefficient for boundary diffusion can be described empirically by

$$D = D_0 \left(\frac{\eta}{\eta_0} \right)^{-\alpha} \quad (4.6)$$

where η_0 is the reference solvent viscosity of water at 5°C, D_0 is the diffusion coefficient for boundary diffusion at η_0 and α reflects the sensitivity of the diffusion coefficient towards changes in solvent viscosity. $\alpha = 1$ demonstrates a $1/\eta$ viscosity dependence as expected for processes limited exclusively by solvent friction whereas $\alpha = 0$ indicates that a reaction is independent of solvent viscosity and not limited by diffusion (103). Studying the effect of solvent viscosity on helix-coil dynamics requires a probing reaction that is fully diffusion-controlled to eliminate any contribution from the probing reaction to the observed viscosity effect. TTET between Xan and Nal is a probing reaction that is diffusion-controlled and thus exhibits a $1/\eta$ viscosity dependence with $\alpha = 1.01 \pm 0.02$ (13, 14, 18). Consequently, TTET does not affect the observed solvent viscosity dependence of boundary diffusion.

Another requirement to obtain the actual viscosity dependence of boundary diffusion is the use of small viscogenic co-solutes. The magnitude of the viscosity effect depends on the size of the co-solute relative to the object. Larger co-solutes exhibit a smaller effect than smaller co-solutes at the same viscosity. This is due to the fact that macroscopic and microscopic solvent viscosity experienced by an object are only identical when the co-solute is of similar size or smaller than the object (212). That is why we used glycerol to increase the solvent viscosity because it is one of the smallest viscogens with a hydrodynamics radius of $r_H = 2.2 \pm 0.2 \text{ \AA}$. The corresponding hydrodynamic diameter ($d_H = 2 \cdot r_H$) of glycerol is equivalent to the length of a peptide bond (3.8 Å) (211, 212).

Figure 4.8A shows the effect of increasing glycerol concentration on global helix stability for a peptide with 21 aa. There is only a minor increase in global helix content as judged by the ellipticity at 222 nm which demonstrates that the stability effect of glycerol is small and the diffusion distance is not affected. However, a bigger effect of glycerol on helix stability is observed for the instable peptide with 15 aa which indicates that the diffusion distance increases with glycerol (Fig. A3).

The TTET kinetics in the center of a helix with 21 aa become slower with increasing glycerol concentration (Fig. 4.8B). Thus, the effect of glycerol on helix-coil dynamics in the helix center entirely relies on the change in solvent viscosity and is not due to increasing diffusion distances. Even the TTET kinetic trace at the highest viscosity is still faster than the spontaneous triplet decay of the donor (grey trace) which demonstrates that

the observed triplet decay is due to intrinsic helix-coil dynamics. The TTET kinetics can be described by the sum of three exponentials at all glycerol concentrations. The additional kinetic phase with less than 10 % in amplitude was not considered for the global analysis and might represent a folded subpopulation (see section 4.3). The global fit of the viscosity dependence of the TTET kinetics using the analytical solution of the three-state model yields the rate constants for k_f , k_u and k_c (Fig. 4.8C, Fig. 4.9). A linear dependence of the logarithm of the solvent viscosity $\log \eta$ on the logarithm of the microscopic rate constants $\log(k_i)$ was assumed according to previous studies and equation 4.6 (64, 78). The glycerol dependence measurements reveal similar values for k_f , k_u and k_c in water as the urea dependence (Tab. 4.3, 4.4, Fig. A2).

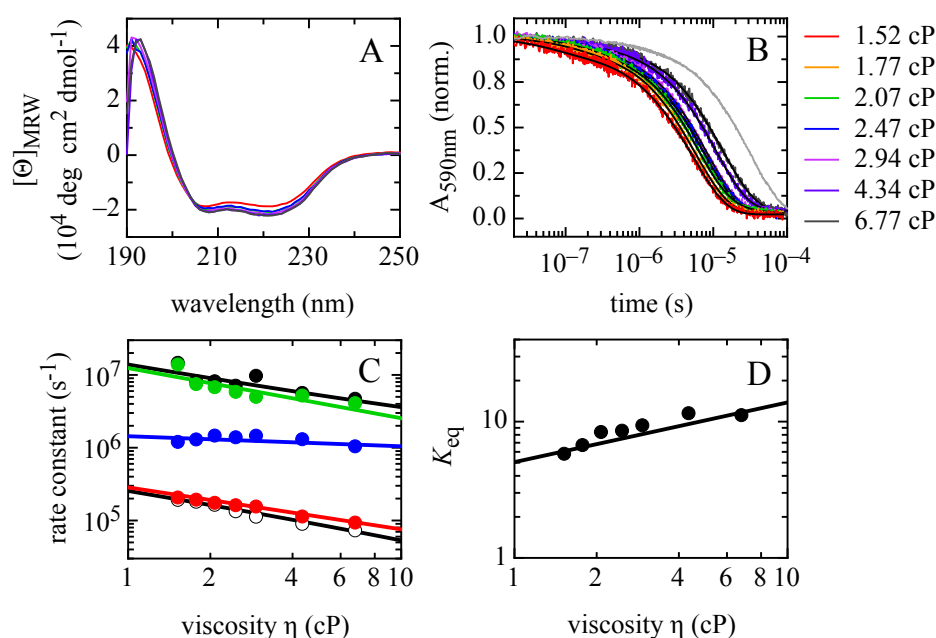


Figure 4.8: Effect of solvent viscosity on helix-coil dynamics and stability in the helix center. (A) Far-UV CD spectra of a peptide with 21 aa in different concentrations of glycerol (0, 5, 10, 15, 20, 30, 40 % (w/v)). (B) TTET kinetics monitored by the triplet absorbance of xanthone at 590 nm in different glycerol concentrations. The grey line represents the triplet lifetime in water for a donor-only peptide as reference. The black lines represent triple-exponential fits to the kinetics. (C) A global fit of the observable rate constants $\lambda_{1,2}$ (black circles) using the analytical solution of the three-state model yields the rate constant for helix folding k_f (blue line), unfolding k_u (red line) and contact formation k_c (green line). Colored filled circles are results from individual fits. (D) Thermodynamic stability in the center of a helix with 21 aa with respect to solvent viscosity obtained by global fitting (line) or individually fitting (circles). All experiments were performed at 5 °C.

Figure 4.8C shows the effect of increasing solvent viscosity on each individual microscopic rate constant in a peptide with 21 aa obtained by a global fit of the viscosity dependence (coloured lines) or by individually fitting each trace (coloured circles). All rate constants decrease with increasing solvent viscosity. Helix unfolding ($\alpha_u = 0.58$) and

contact formation ($\alpha_c = 0.69$) in the center exhibit the strongest solvent viscosity dependence, which is reasonable because both reactions comprise large-scale motions within the peptide and lead to intermolecular interactions with the solvent. Helix folding ($\alpha_f = 0.14$), in contrast, shows only a weak solvent viscosity dependence because it is a local process and leads to the formation of intramolecular hydrogen bonds.

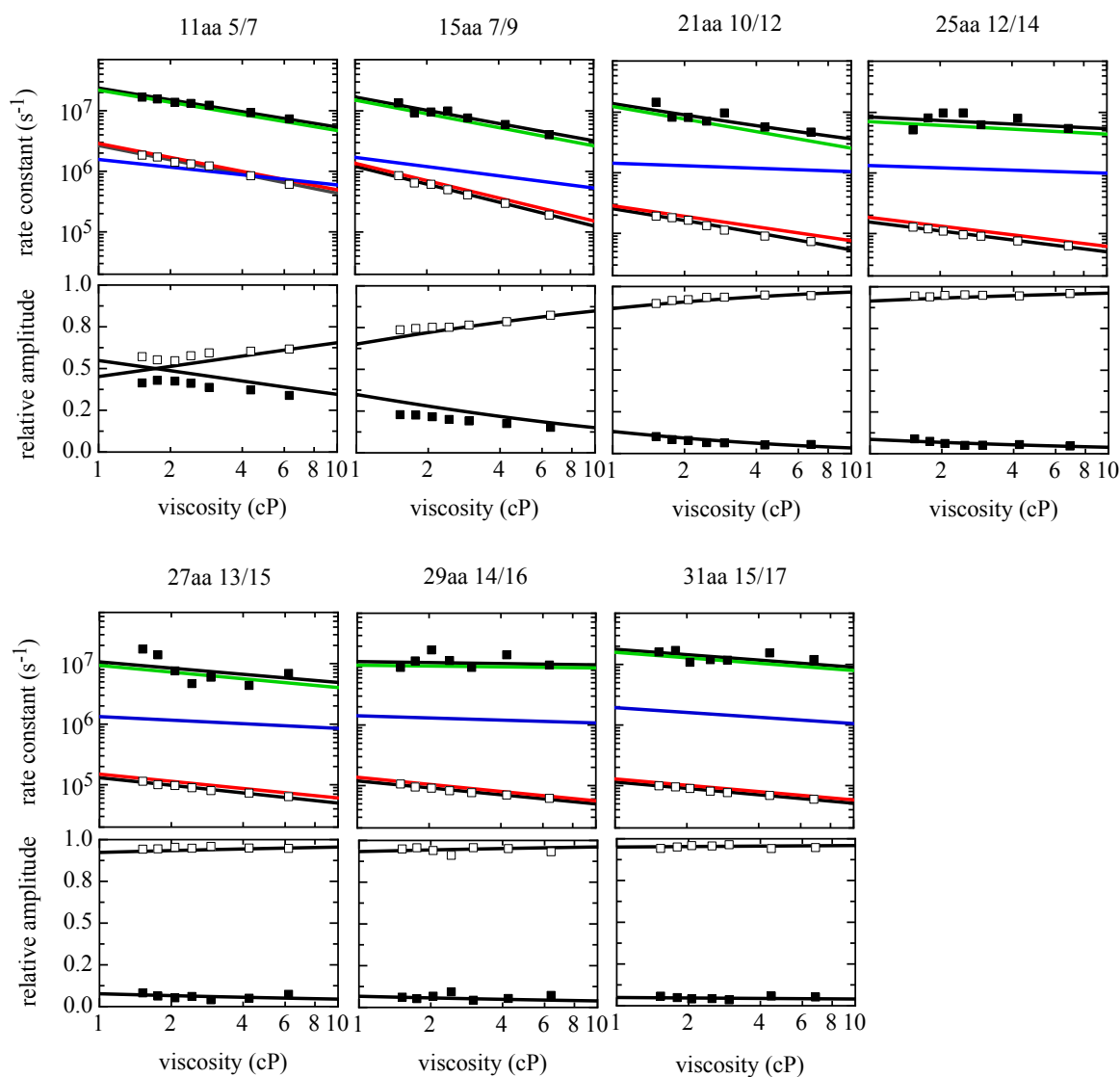


Figure 4.9: Glycerol dependence of helix-coil dynamics in the center of helical peptides of different length. The peptides were labeled in the center with an $i, i+2$ spacing. The squares represent the observable rate constants $\lambda_{1,2}$ and relative amplitudes $A_{1,2}$ obtained from individually fitting each kinetic trace. A global fit of the observable rate constants $\lambda_{1,2}$ (black lines) and amplitudes $A_{1,2}$ (black lines) using the analytical solution of the three-state model yields the rate constant for helix folding k_f (blue line), unfolding k_u (red line) and contact formation k_c (green line). All experiments were performed in 10 mM potassium phosphate buffer, pH 7.0 at 5 °C.

Table 4.4: Effect of helix length on stability and dynamics in the central region of helical peptides with respect to glycerol.

Peptide Label pos.	k_u (10^5s^{-1})	k_f (10^6s^{-1})	k_c (10^6s^{-1})	α_u	α_f	α_c	K_{eq}	A_{miss} (%)
11aa 5/7	20.91 ± 2.86	1.31 ± 0.30	16.55 ± 3.40	0.76 ± 0.03	0.42 ± 0.04	0.67 ± 0.03	0.63 ± 0.15	67
15aa 7/9	9.16 ± 0.08	1.38 ± 0.22	10.98 ± 2.88	0.95 ± 0.02	0.51 ± 0.03	0.75 ± 0.05	1.51 ± 0.24	48
21aa 10/12	2.24 ± 0.45	1.36 ± 0.27	9.31 ± 0.85	0.58 ± 0.04	0.14 ± 0.04	0.69 ± 0.15	6.06 ± 1.19	13
25aa 12/14	1.52 ± 0.17	1.26 ± 0.34	6.47 ± 4.89	0.48 ± 0.04	0.13 ± 0.05	0.21 ± 0.20	8.29 ± 2.21	11
27aa 13/15	1.27 ± 0.18	1.23 ± 0.52	8.00 ± 2.50	0.39 ± 0.04	0.19 ± 0.06	0.37 ± 0.23	9.68 ± 4.04	10
29aa 14/16	1.17 ± 0.21	1.35 ± 0.36	9.52 ± 5.86	0.39 ± 0.03	0.12 ± 0.08	0.05 ± 0.20	11.59 ± 3.12	8
31aa 15/17	1.11 ± 0.09	1.73 ± 0.46	13.99 ± 8.89	0.35 ± 0.03	0.26 ± 0.07	0.30 ± 0.15	15.55 ± 4.15	3

α_u , α_f and α_c are the glycerol dependencies of $\log k_u$, $\log k_f$ and $\log k_c$ respectively (see equation 4.6). A_{miss} denotes the dead time absorbance change with respect to the donor-only reference.

The solvent viscosity dependence of all rate constants decreases with the length of the peptides and similar results were obtained by individually fitting each kinetic trace (Tab. 4.4, Fig. 4.9, A2, A3). The decrease in the α -value with helix length suggests that helix folding, unfolding and contact formation comprise large-scale motions in shorter helices and more local motions in longer helices. Large-scale motions are stronger coupled to solvent motions than local motions and therefore might lead to a decrease in the α -value with helix length (223). However, these are only apparent values which do not correlate with the elementary reaction. The linear Ising model has to be applied to allow any interpretation on the solvent viscosity dependence of all rate constants.

Based on the rate constant for helix folding and unfolding the equilibrium constant K_{eq} can be calculated. Figure 4.8D shows that the thermodynamic stability in the center of the helix with 21 aa increases with increasing viscosity which could be due to a slowing down of boundary diffusion, i.e. helix unfolding. However, this change in stability becomes smaller with increasing length of the peptide (Fig. A3). Another explanation might be that glycerol stabilizes the folded, helical conformation by preferential hydration, which is a common effect of viscogens on equilibrium properties (65). This might explain the small increase in the rate constant for helix folding k_f until 2 cP, which was apparent only by fitting the kinetic traces individually (Fig. 4.8C). However, this effect is not observed in other peptides (Fig. A3). The rate constant for helix unfolding k_u , in contrast, decreases linearly with increasing viscosity indicating a marginal stability effect of glycerol.

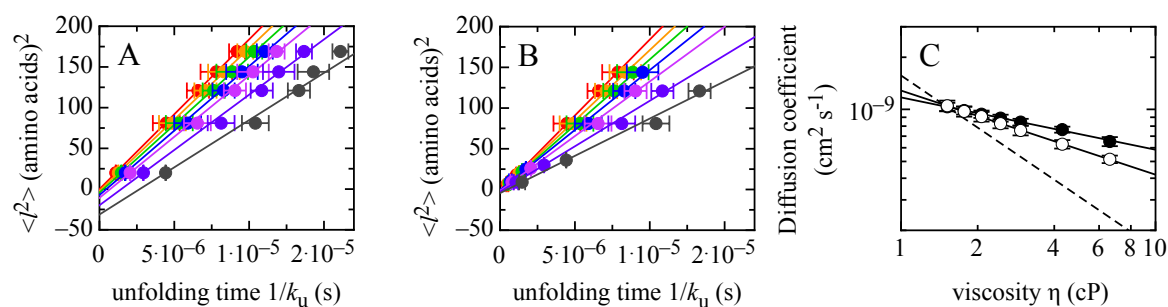


Figure 4.10: Solvent viscosity dependence of the diffusion coefficient for helix-coil boundary diffusion.

(A, B) Correlation between the distance of boundary diffusion and the time constant for helix unfolding at different glycerol concentrations (0 – 40 % (w/v), red to black circles) with fixed (A) and adjusted diffusion distances (B). The different plots of $\langle l^2 \rangle$ vs. $1/k_u$ are linear, indicating that boundary diffusion can be described by equation 4.1. The solid lines represent fits of equation 4.2 to the data. Some data points were omitted for clarity. (C) Corresponding double logarithmic plot of the diffusion coefficient for boundary diffusion with respect to solvent viscosity. The data were fitted with equation 4.6 and revealed a solvent viscosity dependence of boundary diffusion between $\alpha = 0.3$ (filled circles) and $\alpha = 0.5$ (open circles). A fully diffusion-controlled reaction with a $1/\eta$ viscosity dependence ($\alpha = 1$) is shown in comparison (dashed line).

To test whether boundary diffusion is completely diffusion controlled we need to determine the diffusion coefficient at different solvent viscosities. Thus, we analyzed the effect of the diffusion distance $\langle l^2 \rangle$ on the unfolding time $1/k_u$ of each individual peptide with equation 4.2 as described above (Fig. 4.10A). We assumed that the diffusion distance does not change with increasing solvent viscosity as indicated by CD spectroscopy and considered the terminal amino acids in coil conformation as already stated (Tab. 4.2, Fig. 4.10A). The plots of $\langle l^2 \rangle$ vs. $1/k_u$ are linear for all solvent viscosities indicating that boundary diffusion can be described by a diffusive process. However, the negative offset with increasing solvent viscosities indicates that the diffusion distances might be underestimated for shorter helices which show stability effects of glycerol (Fig. 4.10A).

The slope of each individual plot yields the diffusion coefficient at the respective solvent viscosity (Eq. 4.2). As can be seen, the slope decreases with increasing glycerol concentration indicating that the diffusion coefficient decreases with increasing solvent viscosity as expected for a diffusion-controlled reaction (Fig. 4.10A). For the calculation of the diffusion coefficient only peptides shorter than 29 aa were considered because these contain only few coil nucleation events. The corresponding double logarithmic plot of the diffusion coefficient against the solvent viscosity demonstrates that boundary diffusion decreases linearly with increasing solvent viscosity (filled circles Fig. 4.10C). The effect of solvent viscosity η on the diffusion coefficient D for boundary diffusion was analyzed with equation 4.6. A completely diffusion-controlled reaction has $\alpha = 1$ which demonstrates a $1/\eta$ viscosity dependence (dashed line, Fig. 4.10C). A double logarithmic plot of the diffusion coefficient against the solvent viscosity was used to obtain the α -value from the slope. The slope yields $\alpha = 0.30 \pm 0.04$ with a diffusion coefficient at η_0 of $D_0 = 1.03 \pm 0.03 \cdot 10^{-9} \text{ cm}^2 \text{ s}^{-1}$ (filled circles) (Eq. 4.6). The diffusion coefficient in water is close to the value obtained from the urea dependence ($D = 1.07 \pm 0.07 \cdot 10^{-9} \text{ cm}^2 \text{ s}^{-1}$). The α -value of 0.3 represents a lower limit for the sensitivity of boundary diffusion towards changes in solvent viscosity because we assume the helix-coil boundary at constant positions (2 and n-1) at all solvent viscosities.

However, the negative offset indicates that the diffusion distances might change for shorter helices with increasing solvent viscosity (Fig. 4.10A). Adjusting the diffusion distances for the helix with 15 aa by changing the average position of the boundary from 4 to 2 or n-3 to n-1 respectively, leads to zero y-intercepts at all viscosities (Fig. 4.10B). The plot of $\log D$ vs. $\log \eta$ yields a slope of $\alpha = 0.49 \pm 0.05$ and a diffusion coefficient of $D_0 = 1.05 \pm 0.05 \cdot 10^{-9} \text{ cm}^2 \text{ s}^{-1}$ in water (open circles 4.10C). For the calculation of the

diffusion coefficient only peptides shorter than 27 aa were considered for the last three solvent viscosities. The α -value of 0.5 might represent the actual viscosity dependence of boundary diffusion. The fractional viscosity dependence of the diffusion coefficient represents a deviation from the Stokes law (216). This deviation indicates that boundary diffusion is not completely diffusion-controlled and suggests that boundary diffusion is additionally limited by energy barriers such as steric effects from torsional backbone isomerization and intramolecular interactions (111, 113, 114). This is in agreement with pressure dependence measurements on helix-coil dynamics, which revealed that the helix-coil transition proceeds through a high-energy transition state with a larger volume than the ground states (224). The large volume was explained due to the presence of unsatisfied hydrogen bonds and steric effects.

However, we additionally have to perform temperature-dependent measurements of the diffusion coefficient for boundary diffusion to determine whether intrinsic energy barriers limit boundary diffusion.

4.2.2 Effect of Temperature on Boundary Diffusion

We studied the effect of temperature on boundary diffusion to test whether intrinsic energy barriers slow down boundary diffusion. Therefore, we measured helix-coil dynamics in peptides of various lengths at different temperatures between 5 °C and 40 °C in 5 °C steps. Figure 4.11A shows the thermal stability of a peptide with 21 aa monitored by the change in ellipticity at 222 nm. The CD signal decreases with increasing temperature, which is indicative of a loss in helical structure. This behavior was observed for all peptides that show a helical conformation. In contrast, the CD signal of completely unfolded peptides increases linearly with temperature (Fig. A5). Therefore, we considered only peptides with helical structure between 15 aa to 31 aa for determining the diffusion coefficient for helix-coil boundary diffusion within a temperature range of 5 °C to 40 °C (Fig. 4.12).

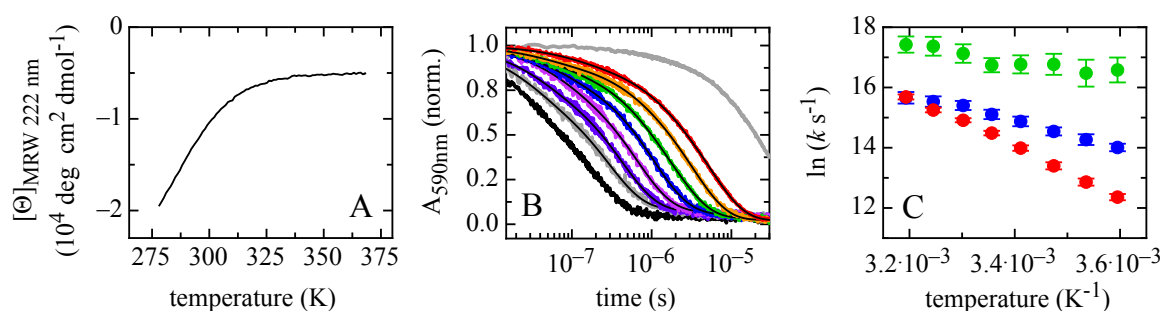


Figure 4.11: Effect of temperature on helix-coil dynamics and stability in the helix center. (A) Thermal unfolding transition of a peptide with 21 aa monitored by the change in ellipticity at 222 nm. (B) TTET kinetics monitored by the triplet absorbance of xanthone at 590 nm at different temperatures (5 – 40°C, red to black). The grey line represents the triplet lifetime at 5 °C for a donor-only peptide as reference. The black lines represent triple-exponential fits to the kinetics. (C) A global fit of the urea dependence data using the analytical solution of the three-state model yielded the rate constant for helix folding k_f (blue), unfolding k_u (red) and contact formation k_c (green) at the respective temperature. The rate constants in the Arrhenius plot are not viscosity-corrected.

The TTET kinetics of a helix with 21 aa in the center are accelerated with increasing temperature (Fig. 4.11B). The missing amplitude at the beginning of the kinetics in relation to the donor reference is caused by a fraction of unfolded peptides which already form contact within laser excitation. This missing amplitude increases with temperature because the fraction of unfolded peptides increases (Fig. A5). Figure 4.11C shows the Arrhenius plot of the corresponding rate constants for helix folding, unfolding and contact formation in the center obtained by globally fitting an urea dependence at the respective temperature. All rate constants show an almost linear dependence of $\ln k$ vs. $1/T$ indicating only a small change in the heat capacity ($\Delta C_p^{0\dagger}$). This is in contrast to previous studies on

helical peptides with $i,i+6$ spacing, where a pronounced curvature was found in the Arrhenius plot (225). The rate constants for helix folding and unfolding in the center show a strong temperature dependence whereas contact formation is almost independent of the temperature with an apparent activation energy of 24 kJ mol^{-1} . This value is in accordance with apparent activation energies found for loop formation in unstructured polypeptides and is partly due to the decrease in solvent viscosity with increasing temperature (211, 212). However, the increase in the rate constants for helix folding k_f and unfolding k_u with temperature can be attributed to peptide unfolding, smaller energy barriers and the change in solvent viscosity with temperature. Peptide unfolding leads to smaller distances from the helix-coil boundary to the helix center and accordingly speeds up helix unfolding and TTET in the center (Fig. 4.11B, C, A5).

The diffusion coefficient for boundary diffusion is obtained by a correlation between the distance of boundary diffusion and the time constant for helix unfolding in the center at the respective temperature (Fig. 4.12A, A11, Eq. 4.2). The plots of $\langle l^2 \rangle$ vs. $1/k_u$ are linear for all temperatures. Figure 4.12A shows that the slope and consequently the diffusion coefficient increase with temperature. We assume a change in the diffusion distance with temperature of 1 aa per $10 \text{ }^\circ\text{C}$ (1 aa per $5 \text{ }^\circ\text{C}$ in total). Even if we do not consider a change in the diffusion distance it has no significant effect on the results (Fig. A4). The diffusion coefficient for boundary diffusion at the respective temperature is calculated as described above for peptides shorter than 29 aa until $25 \text{ }^\circ\text{C}$ (Eq. 4.2). Above $25 \text{ }^\circ\text{C}$ all peptides between 15 aa to 31 aa were considered. Figure 4.12B shows that the logarithm of the diffusion coefficient for boundary diffusion increases linearly with temperature which is expected for a diffusion-controlled reaction. The diffusion coefficient for boundary diffusion was viscosity-corrected to correct for the decrease in solvent viscosity with temperature (Eq. 4.7).

$$D_0(T) = D(T) \cdot \left(\frac{\eta(T)}{\eta_0} \right)^\alpha \quad (4.7)$$

Here, $D(T)$ is the experimentally observed diffusion coefficient at the respective temperature T , $\eta(T)$ is the viscosity of water at a given temperature and η_0 is the viscosity of water at $5 \text{ }^\circ\text{C}$. The viscosity-corrected diffusion coefficient $D_0(T)$ is obtained by using the experimentally determined α -value from the glycerol dependence ($\alpha = 0.5$) (Fig. 4.12B).

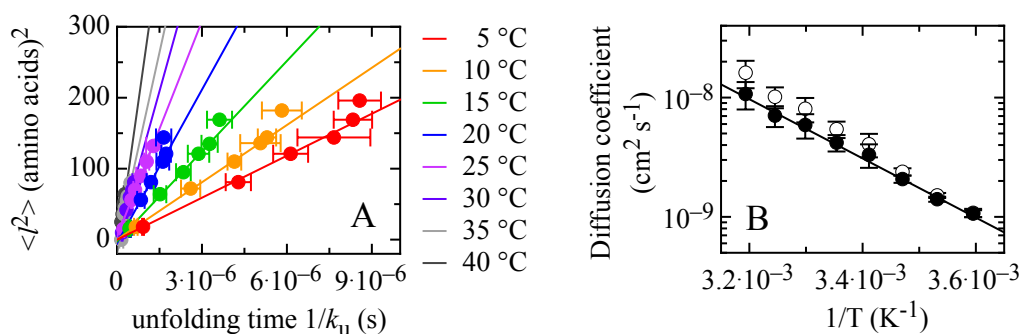


Figure 4.12: Temperature dependence of the diffusion coefficient for helix-coil boundary diffusion. (A) Correlation between the distance of boundary diffusion $\langle l^2 \rangle$ and the time constant for helix unfolding $1/k_u$ for all peptides at different temperatures. The different plots of $\langle l^2 \rangle$ vs. $1/k_u$ are linear, indicating that boundary diffusion can be described by equation 4.1. The solid line represents a fit of equation 4.2 to the data. (B) Effect of temperature on the logarithm of the diffusion coefficient for boundary diffusion. The open circles represent the observed diffusion coefficient and the filled circles represent the diffusion coefficient corrected for the viscosity change with temperature using $\alpha = 0.5$ (Eq. 4.7). The solid line represents a fit of equation 4.8 to the data.

The linear temperature dependence of the diffusion coefficient for boundary diffusion allows an empirical determination of the activation energy for boundary diffusion by the Arrhenius equation (Eq. 4.8) (226).

$$D = D_0 \cdot e^{\left(\frac{-E_a}{RT}\right)} \quad (4.8)$$

Here, D_0 is the diffusion coefficient for boundary diffusion in absence of any free energy barriers, E_a is the activation energy and RT is the thermal energy, where R is the universal gas constant and T the absolute temperature. A classical Arrhenius analysis reveals an energy barrier of $E_a = 47.5 \pm 3.1 \text{ kJ mol}^{-1}$ using $\alpha = 0.5$ and $D_0 = 0.85 \pm 1.12 \text{ cm}^2 \text{ s}^{-1}$ with an upper limit of $E_a = 51.1 \pm 3.2 \text{ kJ mol}^{-1}$ for $\alpha = 0.3$ (Tab. 4.5, Fig. 4.12B). An activation energy of $E_a \approx 48 \text{ kJ mol}^{-1}$, which is in the order of $19.5 RT$ at room temperature might be an explanation for the weak solvent viscosity dependence. Even when we consider boundary diffusion as completely diffusion-controlled with a $1/\eta$ viscosity dependence ($\alpha = 1$) yields an activation energy of $E_a = 38.6 \pm 3.3 \text{ kJ mol}^{-1}$ (Tab. 4.5).

However, helix-coil dynamics are more complex because of the multi-state character of α -helices and do not occur as a single step. Thus, a classical Arrhenius analysis might not be valid to determine the activation parameters for this system. The low cooperativity of the helix-coil transition suggests a rough energy landscape with different conformations of similar energy to the global minimum that encounter many small barriers (227) (Fig. 4.13). Zwanzig considered in a theoretical study a simple one-dimensional version

for diffusion in a rough potential (228). In his work he correlated the temperature dependence of a 1-D diffusion process with the barrier height E_a for different scenarios. If the potential roughness is random or Gaussian distributed, then the effective diffusion coefficient is

$$D = D_0 \cdot e^{\left(\frac{E_a}{k_B T}\right)^2} \quad (4.9)$$

where D_0 is the diffusion coefficient in absence of any energy barriers, E_a is the average barrier height encountered by diffusion and $k_B T$ is the thermal energy (Fig. 4.13A). However, if the potential roughness is periodically distributed and identical for each diffusion step, which we assume for boundary diffusion, then the effective diffusion coefficient is (Fig. 4.13B)

$$D = D_0 \cdot e^{\left(\frac{2E_a}{k_B T}\right)} \quad (4.10)$$

Depending on the roughness of the potential, diffusion can be slowed down, especially at lower temperatures where $E_a \gg k_B T$. Consequently, the observed diffusion coefficient depends on the height of the energy barriers. We apply both theoretical models on our experimental data to obtain information about the barrier height, which slows down boundary diffusion.

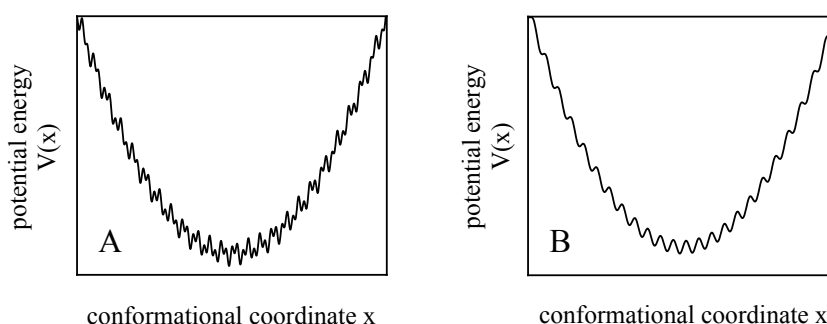


Figure 4.13: Example of a rough one-dimensional energy landscape. Diffusion in a rough one-dimensional potential with a random distribution of many small potential barriers (A) or periodically distributed potential barriers of identical height (B). Figure modified according to Zwanzig (228).

Applying equation 4.9 on the data with a random distribution of barrier heights reveals an average barrier height of $E_a = 7.6 \pm 0.3 \text{ kJ mol}^{-1}$ and a diffusion coefficient in absence of

energy barriers of $D_0 = 4.69 \pm 3.19 \cdot 10^{-5} \text{ cm}^2 \text{ s}^{-1}$ (Tab. 4.5). A barrier height of $\approx 8 \text{ kJ mol}^{-1}$ is in good agreement with results of H-bond energies determined by experiments and simulations which found values between $6 - 9 \text{ kJ mol}^{-1}$ (162, 229-231). Schellman estimated an enthalpy change of $\Delta H = -6.3 \text{ kJ mol}^{-1}$ per hydrogen bond in helices, which is in good agreement with Scholtz *et al.* who found experimentally a value of $\Delta H = -4.2 \text{ kJ mol}^{-1}$ per residue (134, 160).

Table 4.5: Activation energies for boundary diffusion according to Arrhenius and Zwanzig.

α -value	E_a Arrhenius	E_a Zwanzig (identical barrier heights)	E_a Zwanzig (random barrier heights)
0	56.4 ± 3.2	28.2 ± 1.6	8.3 ± 0.2
0.3	51.1 ± 3.2	25.6 ± 1.6	7.9 ± 0.3
0.5	47.5 ± 3.1	23.8 ± 1.6	7.6 ± 0.3
1	38.6 ± 3.3	19.3 ± 1.6	6.8 ± 0.3

Activation energy E_a according to Arrhenius (Eq. 4.8) and Zwanzig with a random (Eq. 4.9) or periodic distribution of barrier heights (Eq. 4.10) with respect to different solvent viscosity corrections α (Eq. 4.7). The activation energies are in kJ mol^{-1} .

However, we assume that boundary diffusion encounters similar energy barriers for each diffusion step especially for peptides which consist mainly of alanine residues. Thus, applying the Arrhenius-like model with periodically distributed barriers of identical height (Eq. 4.10) yields $E_a = 23.8 \pm 1.6 \text{ kJ mol}^{-1}$ and $D_0 = 0.85 \pm 1.12 \text{ cm}^2 \text{ s}^{-1}$ (Tab. 4.5). Based on T-jump experiments, Jas *et al.* also reported a weak solvent viscosity dependence ($\alpha = 0.6$) of helix-coil dynamics with an intrinsic activation energy of $\sim 21 \text{ kJ mol}^{-1}$ which is in good agreement with our results (109). When we consider no change in the diffusion distance an average barrier height of $E_a = 9.4 \pm 0.2 \text{ kJ mol}^{-1}$ for a random distribution (Eq. 4.9) and $E_a = 36.5 \pm 1.7 \text{ kJ mol}^{-1}$ (Eq. 4.10) for a periodic distribution of barrier heights is obtained (Fig. A4). This demonstrates that the diffusion distance has only a small effect on the results and that boundary diffusion is slowed down by energy barriers.

The experimentally determined maximum diffusion coefficient D_0 yields the maximum rate constant k for helix growth and shrinking by one amino acid (Eq. 4.11).

$$k = \frac{2D}{\delta^2} \quad (4.11)$$

The Arrhenius (Eq. 4.8) and Arrhenius-like equation (Eq. 4.10) yields a maximum value for the elementary step of $k = 8 \cdot 10^{15} \text{ s}^{-1}$ which is 7 to 5 orders of magnitude faster than determined previously (194, 196, 198). However, this difference can be explained by the fact that D_0 consists of both a pre-exponential factor k_0 and an entropic contribution $\Delta S^{0\dagger}$ according to the van't Hoff-Arrhenius law (Eq. 1.11). The model of Zwanzig with a random distribution of barrier heights (Eq. 4.9) yields a maximum value of $k = 4 \cdot 10^{11} \text{ s}^{-1}$, which is in accordance with the value predicted by Schwarz (194, 196). Schwarz and co-workers estimated an upper value for helix elongation of $k = 10^{10} \text{ s}^{-1}$ with an elementary step of backbone isomerization $k_1 \approx 10^{10} \text{ s}^{-1}$ and hydrogen bond formation $k_2 \geq 10^{11} \text{ s}^{-1}$ (196).

Nevertheless, independent of the chosen model, we could show that the weak solvent viscosity dependence ($\alpha = 0.5$) of helix-coil boundary diffusion originates from intrinsic energy barriers ranging between 8 – 48 kJ mol^{-1} . Grote and Hynes predicted a weak solvent viscosity dependence ($\alpha < 1$) for systems with memory friction where local, narrow energy barriers dominate the dynamics of the folding transition (110, 114). These local energy barriers give rise to internal friction effects for the boundary diffusion mechanism in α -helices, which might be attributed to the making/breaking of intramolecular interactions such as hydrogen bonds and steric effects from torsional backbone isomerization as was recently shown by MD-simulations (111, 114). Kiefhaber and co-workers have shown that local dynamics in unstructured polypeptides, which are mainly limited by the steric hindrance of bond rotations, encounter energy barriers up to 20 kJ mol^{-1} with α as low as 0.75 (85, 211, 212). However, they also found that the activation parameters of local chain dynamics depend on the amino acid sequence of the peptide. More flexible poly(Gly-Ser) chains exhibit smaller activation energies of $\sim 15 \text{ kJ mol}^{-1}$ than stiffer poly(Ser) chains with $\sim 20 \text{ kJ mol}^{-1}$ (Fig. 1.11C). This is in accordance with results from Ediger and co-workers who studied local dynamics of different synthetic polymers in various solvents and found activation energies of $\sim 14 \text{ kJ mol}^{-1}$ with an exponent of $\alpha = 0.4$ and 0.8 (232-234). These results suggest that steric effects from torsional isomerization reactions already contribute $\sim 14 \text{ kJ mol}^{-1}$ and more depending on the amino acid sequence. The solvent viscosity dependence of boundary diffusion ($\alpha = 0.5$) is weaker than for unstructured polypeptides ($\alpha = 0.75$) which imply a larger internal friction for boundary diffusion. This can be explained by the fact that besides torsional barriers, H-bonds have to be broken and formed during boundary diffusion. Thus, the boundary diffusion mechanism more likely encounters

larger energy barriers in the range of 24 – 48 kJ mol⁻¹. The isomerization of the C–N amide bond exhibits a rotational barrier of ~ 70 kJ mol⁻¹ which represent an upper value for torsional energy barriers because this bond is intrinsically hindered due to its double bond character (235). This is in contrast to Scheraga, who proposed barriers for bond rotations in polypeptides in the range of 2 – 6 kJ mol⁻¹ (236). On the other hand, H-bond energies can vary from 4 – 50 kJ mol⁻¹, which makes it rather difficult to estimate proper activation parameters for boundary diffusion (134, 160, 162, 229-231, 237-239).

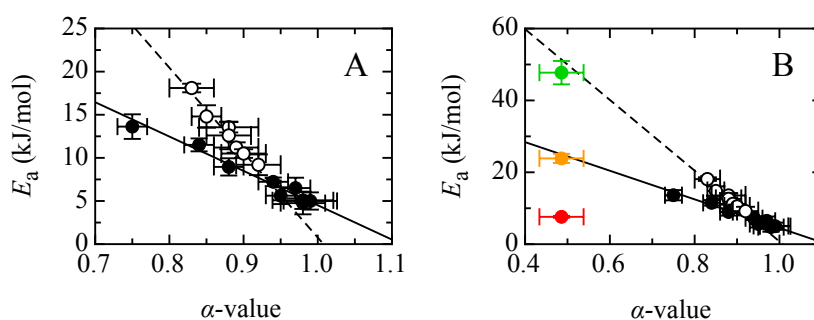


Figure 4.14: Correlation between the activation energy E_a and solvent viscosity dependence α for loop formation in unstructured polypeptides and boundary diffusion in helical peptides. (A) Correlation of the activation energy for loop formation of flexible poly(Gly-Ser) (filled circles and solid line) and stiffer poly(Ser) peptides (open circles and dashed line) with α . Both sequences show different correlations of E_a and α . (B) The barrier height of boundary diffusion according to Arrhenius (Eq. 4.8, green), Zwanzig with random (Eq. 4.9, red) and identical barrier heights (Eq. 4.10, orange) is plotted in comparison to the unstructured peptides. The lines represent linear fits of poly(Gly-Ser) and poly(Ser) peptides. Data from unstructured peptides were taken from (211, 212).

Grote and Hynes predicted that the height of local energy barriers E_a must be directly related to the solvent viscosity dependence α (110, 114). Recent results revealed a correlation of the α -value with the activation parameters for loop formation in different unstructured polypeptide chains as was proposed by the Grote-Hynes-theory (211, 212). Figure 4.14A shows the plot of E_a vs. α for poly(Gly-Ser) and poly(Ser) chains. Both peptide sequences show that E_a is inversely proportional to α ($E_a \propto 1/\alpha$) but with a different correlation. Flexible chains show generally smaller activation energies than stiffer chains at the same α -value. This demonstrates that internal friction effects depend on the amino acid sequence as each side chain has different steric properties. A comparison of the activation parameters for boundary diffusion obtained by the different models with the activation parameters for unstructured polypeptides shows that the model of Zwanzig, which assumes a random distribution of barrier heights (Eq. 4.9) does not adequately describe our data (Fig. 4.14B). In contrast, the Arrhenius-like model (Eq. 4.10)

and classical Arrhenius model (4.8) fit to the correlation of both the flexible and stiffer peptide sequences. This indicates that the Arrhenius-like model (Eq. 4.8) with periodically distributed potential barriers of identical height is more realistic for the 1-D boundary diffusion mechanism of α -helices, as expected. The barrier height of 24 kJ mol^{-1} fits into the range of flexible poly(Gly-Ser) peptide sequences. However, the steric effects of alanine-based α -helices is more comparable with the stiffer poly(Ser) chains which suggests that an classical Arrhenius analysis with a barrier height of 48 kJ mol^{-1} might be valid.

However, despite encountering barriers, helix-coil boundary diffusion still follows a classical, Einstein type, 1-D diffusion law indicating that the diffusing boundary mechanism is not a fully diffusion-controlled process but is rather described by a 1-D random walk with local energy barriers.

4.2.3 Internal and Solvent Friction in Boundary Diffusion

We could show that boundary diffusion is not exclusively limited by solvent friction and encounters significant intrinsic energy barriers in the range of 24 or 48 kJ mol⁻¹ depending on the used model. These barriers that might be attributed to H-bond interactions and sterically hindered bond rotations were shown to be insensitive to solvent friction and hence create internal friction effects for boundary diffusion (111). Moreover, we could demonstrate that internal friction is related to local energy barriers and the height of these local barriers is inversely proportional to the solvent viscosity dependence α ($E_a \propto 1/\alpha$) according to the Grote-Hynes theory (110). Previous work proposed that friction is composed of an additive contribution of internal friction f_{int} to solvent friction f_{solv} (Eq. 4.12) (119-123).

$$f_r = f_{solv} \cdot \left(\frac{\eta}{\eta_0} \right)^\alpha + f_{int} \quad (4.12)$$

For systems where the time scale of barrier crossing is slower than the time scale of solvent motions, the friction of barrier crossing is constant and proportional to the solvent viscosity ($\alpha = 1$). Consequently, internal friction is independent of the solvent viscosity and results in a positive offset at vanishing viscosities according to equation 4.12. However, for systems with memory friction or slow solvent motions with respect to barrier crossing, the friction of barrier crossing is not proportional to the solvent viscosity ($\alpha < 1$) but depends on the barrier frequency. This results in a power law relationship according to the Grote-Hynes theory (110).

We tested the validity of equation 4.12 experimentally by analyzing the solvent viscosity dependence of the diffusion coefficient for boundary diffusion (Fig. 4.15A). The friction coefficient f_r is calculated from the diffusion coefficient according to the Stokes-Einstein equation (Eq. 4.13).

$$D = \frac{k_B T}{6\pi \cdot \eta \cdot r_s} \quad \text{with} \quad f_r = 6\pi \cdot \eta \cdot r_s \quad (4.13)$$

Figure 4.15B shows the friction coefficient for helix-coil boundary diffusion as a function of solvent viscosity. The friction coefficient shows a non-linear dependence on solvent

viscosity indicating a power law relationship as expected for a process that is not exclusively limited by solvent friction. A simple linear relationship for $\alpha = 1$ (Eq. 4.12) with an additive contribution of internal friction to solvent friction cannot adequately describe the data but reveals a contribution from internal friction of $f_{int} = 2.08 \pm 1.02 \text{ g s}^{-1}$ (Fig. 4.15B, C dashed line). However, a power law relationship ($\alpha < 1$) with the experimentally determined α -value from our viscosity dependence measurements ($\alpha = 0.5$) can adequately describe the data but shows no indication for an additive contribution from internal friction ($f_{int} = -0.005 \pm 0.49 \cdot 10^{-5} \text{ g s}^{-1}$) to solvent friction ($f_{solv} = 3.7 \pm 0.4 \cdot 10^{-5} \text{ g s}^{-1}$) (Fig. 4.15B, C solid line). This is consistent with studies on local and global dynamics of unfolded polypeptides and proteins measured by TTET and time-resolved FRET (211, 212, 240, 241). They also reported that a power law with independently fitted α -values gives fit of better quality with no evidence of internal friction. Simulations revealed that a quantitative separation of internal and solvent friction effects is not straightforward because both effects are intrinsically entangled (113). However, our results suggest that internal friction does not contribute additively to solvent friction but modulates the effect of solvent viscosity on boundary diffusion (α) by local energy barriers (Eq. 4.14). Hence, we could demonstrate that equation 4.12 is not a proper description of internal and solvent friction effects in boundary diffusion.

$$f_r = f_{solv} \cdot \left(\frac{\eta}{\eta_0} \right)^\alpha \quad (4.14)$$

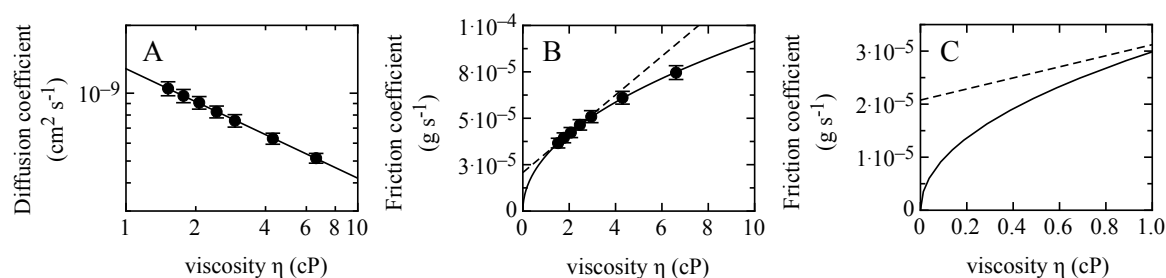


Figure 4.15: Effect of solvent viscosity on the diffusion coefficient and friction coefficient for helix-coil boundary diffusion. (A) Double logarithmic plot of the diffusion coefficient for boundary diffusion with respect to solvent viscosity. The data were fitted with equation 4.6 and revealed a solvent viscosity dependence of boundary diffusion of $\alpha = 0.5$. (B) The corresponding friction coefficient with respect to solvent viscosity was calculated by equation 4.13. The lines represent fits of equation 4.12 to the data with the experimentally determined α -value of $\alpha = 0.5$ (solid line) and $\alpha = 1$ (dashed line). (C) Inset of figure B shows that the power law relationship reveals no contributions from internal friction since the y-axis intercept is zero in the absence of solvent viscosity.

4.3 Characterization of the Third Kinetic Phase

The TTET kinetics of peptides longer than 21 aa can be described by the sum of three exponentials (Fig. 4.16, Fig. A1). The observed triple-exponential kinetics suggest an equilibrium between three distinct populations of molecules. The slowest observable rate constant $\lambda_2 \approx 1.6 \cdot 10^5 \text{ s}^{-1}$ is the main kinetic phase (87 % amplitude) and represents a folded, helical population of molecules. The fastest observable rate constant $\lambda_1 \approx 1.1 \cdot 10^7 \text{ s}^{-1}$ (7 % amplitude) represents an unfolded or partially unfolded population of molecules where contact formation and triplet transfer is enabled as was shown in a previous study (170). The third observable rate constant represents a small population of molecules with $\lambda_3 \approx 1.1 \cdot 10^6 \text{ s}^{-1}$ (6 % amplitude) (Fig. 4.16). All three observable reactions are faster than the spontaneous donor triplet decay ($\lambda_T \approx 5 \cdot 10^4 \text{ s}^{-1}$), which demonstrates that the observed triplet decay is due to intrinsic helix-coil dynamics.

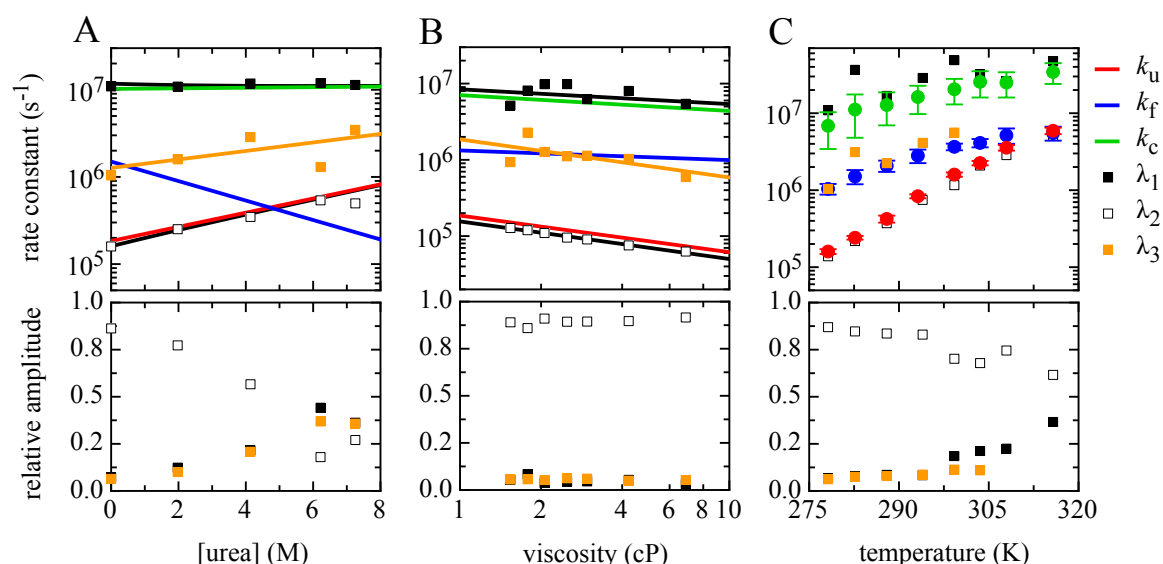


Figure 4.16: Denaturant, solvent viscosity and temperature dependence of the three observable rate constants. (A) Urea dependence, (B) glycerol dependence and (C) temperature dependence of a peptide with 25 aa labeled in the center with an $i,i+2$ spacing. The squares represent the observable rate constants $\lambda_{1,2,3}$ and relative amplitudes $A_{1,2,3}$ obtained from individually fitting each kinetic trace. A global fit of the observable rate constants $\lambda_{1,2}$ (black lines) and amplitudes $A_{1,2}$ (black lines) using the analytical solution of the three-state model yields the rate constant for helix folding k_f (blue line), unfolding k_u (red line) and contact formation k_c (green line). The urea and solvent viscosity dependence of the observable rate constants λ_3 was obtained by a linear fit. All experiments were performed in 10 mM potassium phosphate buffer, pH 7.0 at 5 °C.

To test for the origin of the third kinetic phase, we performed a denaturant, glycerol and temperature dependence. Destabilizing the helical state by addition of urea leads to an increase in amplitude of the third phase λ_3 (220) (Fig. 4.16A, lower panel). In contrast, stabilizing the helical structure by addition of glycerol leads to a decrease in amplitude of

λ_3 (65) (Fig. 4.16B, lower panel). Moreover, the amplitude of λ_3 increases with temperature (Fig. 4.16C, lower panel). However, at 30 °C, λ_3 is not observable and TTET can be described by the sum of two exponentials. These results suggest that this reaction, which shows the same changes in amplitudes as the fast phase λ_1 , originates from molecules that are unfolded or partially unfolded but exhibit slower TTET than in λ_1 .

On the other hand, the rate constant λ_3 shows the same urea dependence as λ_2 with a negative m -value of $-259 \text{ J mol}^{-1} \text{ M}^{-1}$ (Fig. 4.16A, upper panel). Moreover, λ_3 has a similar solvent viscosity dependence as λ_2 with $\alpha = 0.49$ and is strongly temperature-dependent (Fig. 4.16B and C, upper panel). This is in contrast to the observable rate constant λ_1 , that mostly show weaker dependencies to urea and temperature (Fig. 4.16B, C, A5). The slow observable rate constant λ_2 nearly exclusively reflects the rate constant for helix unfolding k_u from the folded, helical state (170). Consequently, the results suggest that λ_3 is related to TTET in partially unfolded conformations where helix unfolding between the labels is still required. However, the observable rate constant λ_3 is independent of the peptide length with a time constant of $1/\lambda_3 \approx 770 \text{ ns}$, suggesting that these molecules have the same conformation in the region of the labels and the same unfolding process leads to TTET in all peptides (Fig. 4.17A).

Concluding, λ_3 represents TTET in a partially unfolded population of molecules where the same helix unfolding process between the labels has to occur in order to enable TTET. It is suggested that this small population of molecules consists of multiple helical segments with separate triplet labels because longer helices have a higher tendency for multiple helical segments which was also shown by previous SAXS experiments (242).

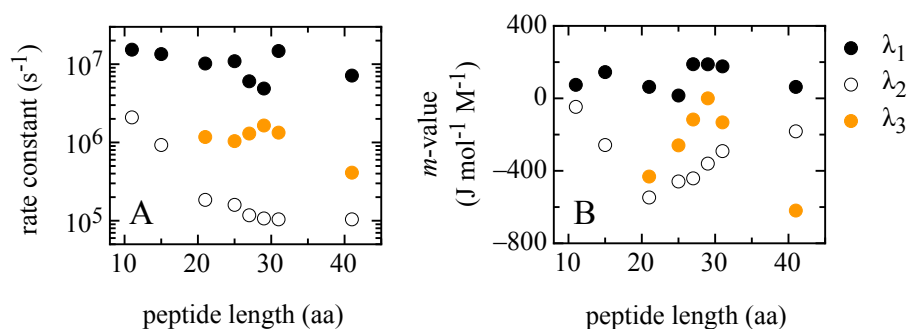


Figure 4.17: Length and urea dependence of all observable rate constants for TTET. (A) Effect of peptide length on the observable rate constants $\lambda_{1,2,3}$ for TTET. (B) Effect of peptide length on the urea dependence (m -value) of the observable rate constants $\lambda_{1,2,3}$ for TTET.

4.4 Effect of Capping Motifs on Boundary Diffusion

4.4.1 Effect of Capping Motifs on Stability and Dynamics in the Helix Center

Specific N- and C-capping motifs are frequently found in protein α -helices and increase helix stability by hydrogen bonding, hydrophobic interactions or electrostatic interactions with the helix-dipole (143, 144, 163-167, 173-176). It was shown recently that capping motifs lead to a stabilization in the helix center by altering helix unfolding dynamics but not refolding in the center (186). Thus, helix stability in the center is changed remotely from the region of stabilization or destabilization and this non-local effect could not be distinguished to an impact on boundary diffusion or boundary diffusion distances. We therefore, investigate the effect of different capping motifs located at the N-cap and C-cap position on the diffusion coefficient and diffusion distances for boundary diffusion by TTET. These experiments were performed with the same series of peptides with $i,i+2$ spacing but varying capping motifs (Tab. 4.2).

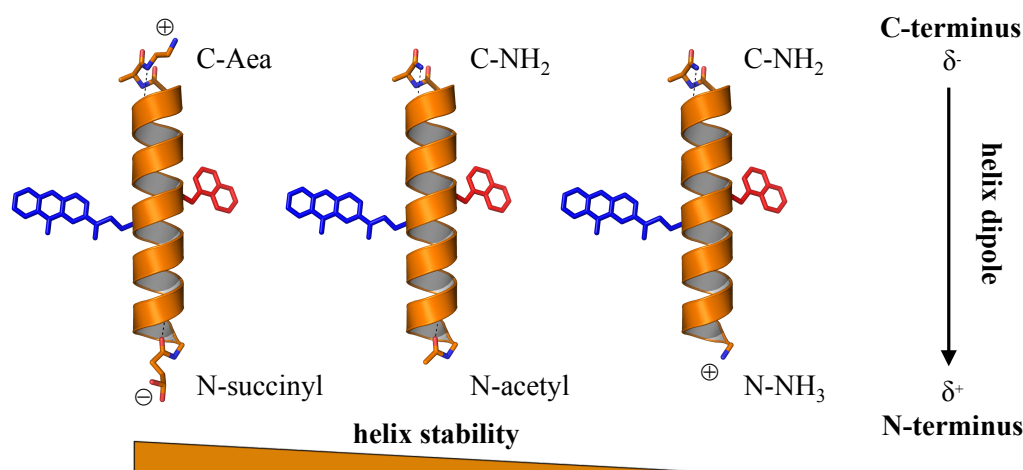


Figure 4.18: Effect of different end-capping motifs on helix stability. We tested three differently charged capping motifs in helical peptides with $i,i+2$ spacing of the TTET labels. Peptides with neutral, uncharged termini are acetylated at the N-terminus (N-acetyl) and amidated at the C-terminus (C-NH₂). Peptides with a destabilizing capping motif have a free, positively charged N-terminus (N-NH₃⁺) and amidated C-terminus (C-NH₂). Peptides with a stabilizing capping motif have a negatively charged, N-terminal succinate (N-succinyl) and positively charged, C-terminal 2-aminoethylamide (C-Aea).

We tested three different N- and C-capping motifs with respect to charges (Fig. 4.18). A stabilizing capping motif with an N-terminal succinyl (Suc) and a C-terminal 2-aminoethylamide (Aea). In these peptides opposing charges at the helix ends are introduced to favorably interact with the helix macro-dipole. Moreover, a destabilizing capping motif with a free, positively charged N-terminus (NH₃⁺) and amidated C-terminus (NH₂) is applied. In these peptides is a positive charge at the positively

charged N-terminus introduced to unfavorably interact with the helix macro-dipole. Finally, a neutral, uncharged capping motif with an acetylated N-terminus (Ac) and amidated C-terminus (NH₂) is applied as a reference with medium stability.

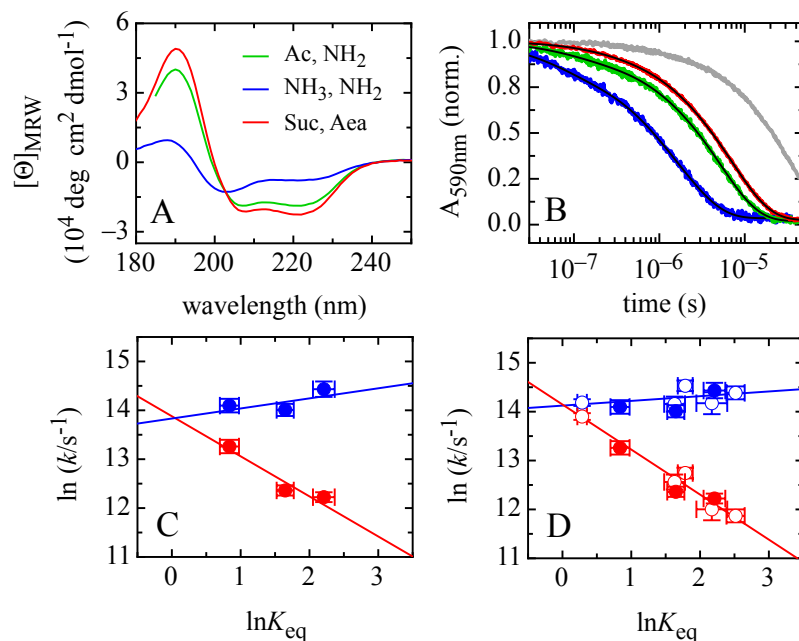


Figure 4.19: Effect of end-capping motifs on helix-coil dynamics and stability in the helix center. (A) Far-UV CD spectra of a peptide with 21 aa and acetylated N-terminus and amidated C-terminus (green), free, positively charged N-terminus and amidated C-terminus (blue) or N-terminal succinate and C-terminal 2-aminoethylamide (Aea) (red). (B) TET kinetics monitored by the triplet absorbance of xanthone at 590 nm. The grey line represents the triplet lifetime for a donor-only peptide as reference. The black lines represent triple-exponential fits to the kinetics. (C) Leffler plot for helix folding k_f (blue) and unfolding k_u (red). The solid lines represent linear fits to the data with a slope of $\Phi_u = 0.82 \pm 0.19$ and $\Phi_f = 0.21 \pm 0.16$. (D) Leffler plot for helices with 21aa (filled circles), 15 aa and 25 aa (open circles). The solid lines represent linear fits to all data with a slope of $\Phi_u = 0.92 \pm 0.07$ and $\Phi_f = 0.09 \pm 0.05$, respectively. All experiments were performed at 5 °C.

First, we investigated the impact of the different N- and C-capping motifs on secondary structure content and global helix stability by CD spectroscopy. The far-UV CD spectra of all peptides show typical helical CD bands with a maximum in ellipticity at 190 nm and minima at 208 and 222 nm (Fig. 4.19A). A quantitative analysis of the helix content at 222 nm is not possible due to absorbance of the TET labels in the far-UV region as already stated above. However, the decrease in the CD band at 222 nm for the peptide with a free N-terminus indicates a lower helix content compared to the reference peptide with a neutral, uncharged capping motif. In contrast, the peptide with a negatively charged N-cap and positively charged C-cap exhibit an increase in negative ellipticity at 222 nm indicating a higher helix content compared to the reference. Thus, a positive charge at the N-terminus leads to repulsive interactions with the helix macro-dipole and

results in a major destabilization of the helix, whereas opposite charges at the termini favorably interact with the helix macro-dipole and leads to a major stabilization of the helix. The same effect was previously observed for the C-peptide, a modified peptide fragment of RNase A (143, 144).

We performed TTET experiments at 5 °C to investigate the impact of capping motifs on folding and unfolding dynamics in the helix center (Fig. 4.19B). The TTET kinetics were monitored by the triplet absorbance decay of xanthone at 590 nm and can be described by the sum of three exponentials. The additional kinetic phase with less than 10 % in amplitude potentially arises from a folded subpopulation as described in section 4.3 and was not included into the global analysis. Figure 4.19B shows that TTET in the central region of the helix is decelerated by the stabilizing capping motif and accelerated by the destabilizing capping motif. The urea dependence of the TTET kinetics of each peptide was fitted globally using the analytical solution of the three-state model to obtain k_u , k_f and k_c (Fig. 4.20). We performed a phi-value analysis in order to quantify the effect of changes in helix stability on the folding and unfolding rate constants (Fig. 4.19C). A Leffler relationship correlates the effect of changes in activation free energy ($\Delta G^{0\dagger}$) with the corresponding effect on equilibrium free energy (ΔG^0) (Eq. 4.15) (29, 87, 243).

$$\phi_f = \frac{\partial \Delta G_f^{0\dagger}}{\partial \Delta G^0} = \frac{\partial \ln k_f}{\partial \ln K_{eq}} \quad \phi_u = \frac{\partial \Delta G_u^{0\dagger}}{\partial \Delta G^0} = \frac{\partial \ln k_u}{\partial \ln K_{eq}} = 1 - \phi_f \quad (4.15)$$

Figure 4.19C shows the effect of the different N- and C-capping motifs on helix folding and unfolding with respect to stability in the central region of a helix with 21 aa. The Leffler plot yields a value of $\Phi_u = 0.82 \pm 0.19$ demonstrating that the stability effect of capping motifs in the center is predominantly due to a change in helix unfolding as was published recently with an *i,i+6* spacing of the TTET labels (186). Helix folding seems to be influenced as well with $\Phi_f = 0.21 \pm 0.16$. However, this is difficult to evaluate because of the large error and the small data set. Moreover, the overall stability difference between the most and least stable helix is only about 3.5 kJ mol^{-1} , which is too low to yield reliable results in a classical phi-value analysis. Extending the data set by using the results from different helix lengths increases the accuracy of the analysis (89, 244). Adding the results from helices with 15 aa and 25 aa into the phi-value analysis yields $\Phi_u = 0.92 \pm 0.07$ and $\Phi_f = 0.09 \pm 0.05$ which is consistent with the previous study on *i,i+6* peptides (Fig. 4.19D) (186). All helix capping variants fall on the same line in the Leffler plot,

indicating that changes in stability at the N- or C-terminus have the same effect on helix-coil dynamics, which implies that boundary diffusion is identical from both directions. It is not possible to obtain information on the transition state for helix formation, since the rate constants k_f and k_u represent helix folding and unfolding dynamics in the region between the TTET labels and not between two conformational states.

The non-local effect of the capping motifs on helix unfolding in the center suggests two possible origins. One possibility is that capping motifs lead to a helix elongation and thereby increase the diffusion distance $\langle l^2 \rangle$ from the boundary to the helix center. The other possibility is that capping motifs stabilize helices kinetically by increased energy barriers and thus slow down boundary diffusion (186). Both effects would result in a decrease in the rate constant for helix unfolding k_u in the center as was observed in the Leffler relationship (Fig. 4.19D). Therefore, we tested the effect of capping motifs on the diffusion coefficient D and diffusion distance $\langle l^2 \rangle$ for boundary diffusion in helical peptides.

4.4.2 Effect of Capping Motifs on the Diffusion Coefficient for Boundary Diffusion

Helix folding and unfolding dynamics are studied in alanine-based helical peptides of different length between 11 aa and 31 aa with central TTET labels and $i,i+2$ spacing as described before (Fig. 4.3). Figure 4.20 shows the effect of peptide length on helix-coil dynamics and secondary structure content for all capping motifs. The impact of peptide length on secondary structure and global stability was judged by CD spectroscopy (Fig. 4.20A, D, G, Tab. 4.6, 4.7). All peptides show typical helical CD spectra. The increase in helix content with increasing peptide length as indicated by an increase in ellipticity at 222 nm is observed for all capping motifs. However, the peptides with destabilizing capping motif show on average smaller helicities than the peptides with stabilizing capping motif. As expected, opposite charges at the capping positions are favorable regarding the helix macro-dipole and lead to a global stabilization of the helix. However, the global stability effect of the N- and C-caps is more prominent in shorter helices than in longer which is in agreement with the Lifson-Roig theory and previous experiments (Fig. A7) (168, 186).

Figure 4.20B, E and H shows that TTET in the central region of the helix is slowed down with increasing length of the peptide but is still faster than the spontaneous triplet decay of the donor (grey trace). However, TTET in peptides with stabilizing capping motif show slower kinetics than peptides of the same length with destabilizing capping motif as already shown above (Fig. 4.19B). A global analysis of the urea dependencies to the analytical solution of the three-state model yields k_u , k_f and k_c (Fig. A6, A8, Tab. 4.6, 4.7). The corresponding plot of the rate constant for helix folding k_f , unfolding k_u and contact formation k_c for the different capping motifs with respect to helix length is shown in figure 4.20C, F and I. Irrespective of the capping motif we observe the same length-dependence for all rate constants demonstrating that capping motifs have no impact on the length dependence of the rate constants. However, the rate constant k_u is decreased in peptides with a stabilizing capping motif and increased in peptides with a destabilizing capping motif whereas k_f is unchanged as was also shown in the Leffler plot (Fig. 4.19). The rate constant for helix folding k_f and unfolding k_u allows to determine the equilibrium constant K_{eq} in the central part of the helix. Figure 4.21 shows that the stability in the helix center is increased by an N-terminal succinyl and C-terminal 2-aminoethylamide group and decreased by a free N-terminal NH_3^+ group with respect to the reference peptides with neutral, uncharged termini (Tab. 4.6, 4.7). Likewise, this stability effect is stronger in shorter helices than in longer as was observed by far-UV CD spectroscopy.

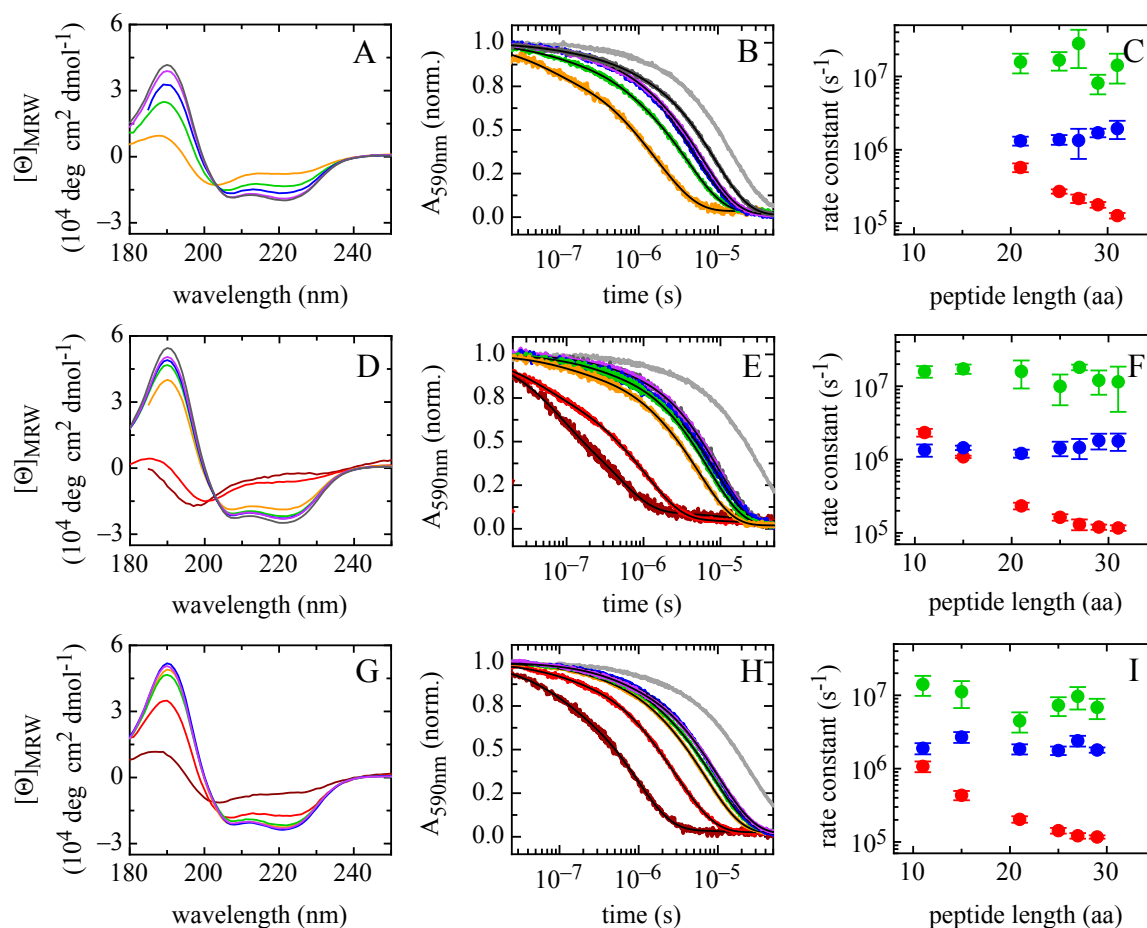


Figure 4.20: Effect of peptide length on helix-coil dynamics and stability in the helix center. Peptides of different lengths with destabilizing (upper panel) and stabilizing capping motif (lower panel) with respect to the reference (middle panel). The colors in the plots correspond to the colors of the peptide lengths (Fig. 4.3). Far-UV CD spectra of peptides with a free N-terminus and C-amide (A), N-acetyl and C-amide (D) or N-succinyl and C-2-aminoethylamide (Aea) (G). TTET kinetics monitored by the triplet absorbance of xanthone at 590 nm (B, E, H). The grey line represents the triplet lifetime for a donor-only peptide as reference. The black lines represent triple-exponential fits to the kinetics. Rate constant for helix folding k_f (blue), unfolding k_u (red) and contact formation k_c (green) obtained by a global fit of the urea dependence data using the analytical solution of the three-state model (C, F, I). All experiments were performed at 5 °C.

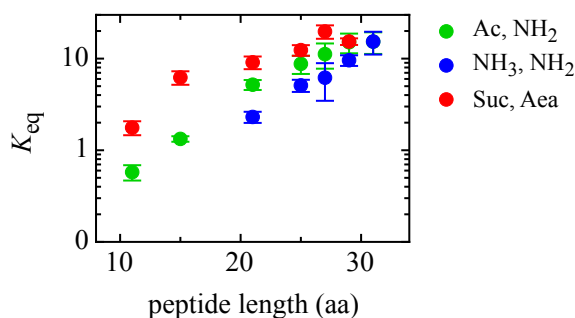


Figure 4.21: Effect of capping motifs on helix stability in the central region of helical peptides. Thermodynamic stability of helical peptides of various length with stabilizing (red) and destabilizing capping motif (blue) in comparison with peptides with neutral, uncharged capping motif (green) at 5 °C.

The diffusion coefficient for boundary diffusion is determined by a correlation of the squared average diffusion distance $\langle l^2 \rangle$ with the helix unfolding time $1/k_u$ in the center of each individual peptide (Eq. 4.16).

$$\langle l^2 \rangle \approx \frac{4D}{k_u} \quad (4.16)$$

A diffusion coefficient for boundary diffusion of $D = 1.07 \pm 0.07 \cdot 10^{-9} \text{ cm}^2 \text{ s}^{-1}$ was determined for peptides containing no charges at the termini (Fig. 4.22). The helix-coil boundary was assumed at position 2 and $n-1$ and only helices shorter than 29 aa were considered in this calculation because longer helices have more contributions of coil nucleation events as demonstrated by the deviation from linearity above 29 aa (see section 4.1.3) (186). Figure 4.22 shows the plots of $\langle l^2 \rangle$ vs. $1/k_u$ for peptides with stabilizing and destabilizing capping motif in comparison to peptides with no charges at the ends. All plots are linear demonstrating that helical peptides with different capping motifs still follow a classical 1-D diffusion law. First, we assumed no change in the diffusion distance $\langle l^2 \rangle$ and considered the same diffusion distances for both capping motifs as described above (Fig. 4.22 A, B). It is evident that the individual unfolding times are faster or slower than the neutral, uncharged capping motif. Consequently, both plots show either a negative or positive y-offset indicating varying diffusion distances for the different capping motifs. A positive y-offset indicates shorter diffusion distances from the boundary to the helix center whereas a negative y-offset suggests longer diffusion distances than in the reference peptides. However, the diffusion coefficients are not dramatically changed in comparison to the reference with $D = 1.04 \pm 0.07 \cdot 10^{-9} \text{ cm}^2 \text{ s}^{-1}$ (stabilizing) and $D = 1.30 \pm 0.13 \cdot 10^{-9} \text{ cm}^2 \text{ s}^{-1}$ (destabilizing).

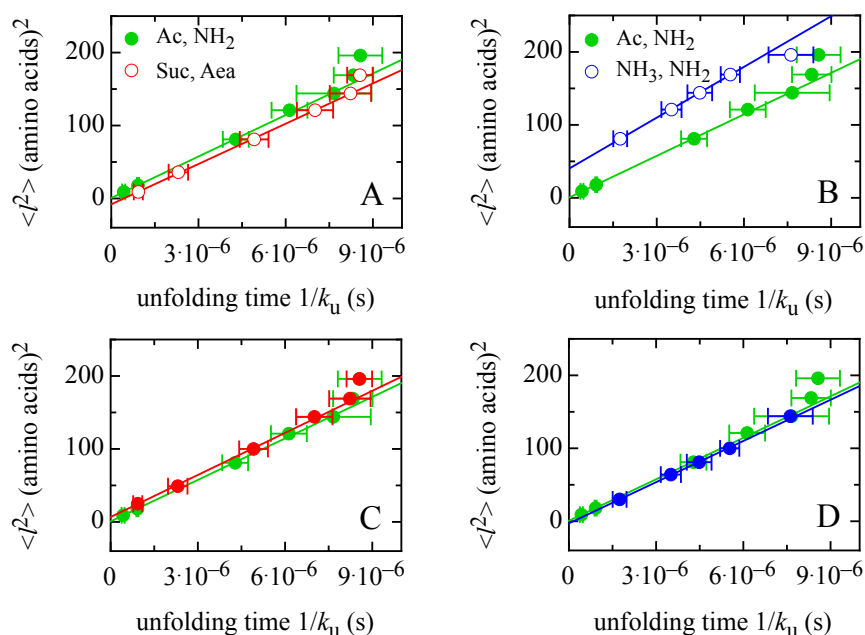


Figure 4.22: Correlation between the distance of boundary diffusion and the time constant for helix unfolding with respect to different capping motifs. Effect of different diffusion distances $\langle l^2 \rangle$ on the helix unfolding time $1/k_u$ in peptides with stabilizing (red) (A, C) and destabilizing capping motif (blue) (B, D) in comparison to peptides with neutral, uncharged termini (green). For the calculation of the diffusion coefficient D unvaried (upper panel, open circles) and varied diffusion distances (lower panel, closed circles) were considered. For unvaried diffusion distances, an average diffusion distance, l , of the boundaries between position 2 and the N-terminal label (Xan) or between position $n-1$ and the C-terminal label (Nal) was used (given as numbers of amino acids) (A, B). For varied diffusion distances, an average diffusion distance, l , between position 1 and the N-terminal label (Xan) or between position n and the C-terminal label (Nal) was used for peptides with stabilizing capping motif (C). For peptides with destabilizing capping motif, an average diffusion distance, l , between position 5 and the N-terminal label (Xan) was used (D). The different plots of $\langle l^2 \rangle$ vs. $1/k_u$ are linear, indicating that boundary diffusion can be described by a 1-D diffusion process (Eq. 4.1). The solid lines represent fits of equation 4.16 to the data.

Assuming a change in the diffusion distances $\langle l^2 \rangle$ is reasonable because the average helix content is altered by attractive and repulsive electrostatic interactions between capping motifs and the helix dipole (Fig. 4.19A). A change in the diffusion distances reduces the y-axis offsets and leads to more reliable diffusion coefficients. Considering longer diffusion distances for peptides with a stabilizing capping motif, where the average position of the boundary is moved from residue 2 and $n-1$ to 1 and n , yields a similar diffusion coefficient as before with $D = 4.81 \pm 0.40 \cdot 10^6 \text{ aa}^2 \text{ s}^{-1}$ or $1.08 \pm 0.09 \cdot 10^{-9} \text{ cm}^2 \text{ s}^{-1}$ (for peptides shorter than 27 aa) but a y-intercept close to zero (Fig. 4.22C, Tab. A1). However, a completely folded helix is rather unlikely at equilibrium suggesting that unfolding to the first TTET label is not sufficient to enable triplet transfer. For peptides with a destabilizing capping motif, shorter diffusion distances from the N-terminus are considered with an average position of the boundary at residue 5 (Tab. A1). These diffusion distances result in a y-intercept of zero and an almost identical diffusion

coefficient as the reference peptides with $D = 4.70 \pm 0.42 \cdot 10^6 \text{ aa}^2 \text{ s}^{-1}$ or $1.06 \pm 0.09 \cdot 10^{-9} \text{ cm}^2 \text{ s}^{-1}$ (Fig. 4.22D).

Thus, neither stabilizing nor destabilizing capping motifs lead to a change in the diffusion coefficient for boundary diffusion, which implies that longer or shorter diffusion distances are the origin of their stability effect as indicated by the y-offsets (Fig. 4.22A, B).

Table 4.6: Effect of helix length on stability and dynamics in the central region of helical peptides with destabilizing capping motif.

Peptide Label pos.	k_u ($10^5 s^{-1}$)	k_f ($10^6 s^{-1}$)	k_c ($10^6 s^{-1}$)	m_u ($J mol^{-1} M^{-1}$)	m_f ($J mol^{-1} M^{-1}$)	m_c ($J mol^{-1} M^{-1}$)	K_{eq}	A_{miss} (%)	Θ 222 nm ($deg cm^2 dmol^{-1}$)
21aa 10/12	5.73 ± 0.8	1.32 ± 0.2	15.72 ± 4.7	-285 ± 38	719 ± 56	-6.1 ± 27	2.31 ± 0.3	40	-7813.2
25aa 12/14	2.70 ± 0.2	1.37 ± 0.2	16.73 ± 4.7	-443 ± 27	1011 ± 41	-22 ± 21	5.10 ± 0.8	29	-13384.1
27aa 13/15	2.17 ± 0.3	1.34 ± 0.6	28.15 ± 15	-413 ± 21	741 ± 30	495 ± 27	6.19 ± 2.7	18	-16459.8
29aa 14/16	1.78 ± 0.2	1.71 ± 0.2	8.12 ± 2.4	-326 ± 23	1221 ± 32	0.26 ± 17	9.59 ± 1.3	10	-19030.5
31aa 15/17	1.26 ± 0.1	1.94 ± 0.5	14.21 ± 6.2	-406 ± 11	955 ± 22	-67 ± 38	15.34 ± 4.3	6	-19829.5

Table 4.7: Effect of helix length on stability and dynamics in the central region of helical peptides with stabilizing capping motif.

Peptide Label pos.	k_u ($10^5 s^{-1}$)	k_f ($10^6 s^{-1}$)	k_c ($10^6 s^{-1}$)	m_u ($J mol^{-1} M^{-1}$)	m_f ($J mol^{-1} M^{-1}$)	m_c ($J mol^{-1} M^{-1}$)	K_{eq}	A_{miss} (%)	Θ 222 nm ($deg cm^2 dmol^{-1}$)
11aa 5/7	10.73 ± 1.8	1.89 ± 0.3	14.12 ± 4.3	-108 ± 21	532 ± 48	17 ± 21	1.76 ± 0.3	45	-7052.6
15aa 7/9	4.33 ± 0.6	2.69 ± 0.5	11.16 ± 4.5	-284 ± 11	422 ± 17	-47 ± 31	6.23 ± 1.1	8	-17344.5
21aa 10/12	2.03 ± 0.2	1.85 ± 0.3	4.48 ± 1.4	-272 ± 9	567 ± 15	-125 ± 20	9.11 ± 1.4	5	-22606.6
25aa 12/14	1.43 ± 0.1	1.76 ± 0.2	7.31 ± 2.1	-230 ± 8	694 ± 13	35 ± 22	12.38 ± 1.6	5	-21745.3
27aa 13/15	1.21 ± 0.1	2.40 ± 0.4	9.68 ± 3.3	-261 ± 10	706 ± 14	109 ± 30	19.75 ± 3.3	2	-23558.7
29aa 14/16	1.17 ± 0.1	1.80 ± 0.2	6.85 ± 2.1	-245 ± 7	689 ± 10	91 ± 24	15.39 ± 1.3	7	-23145.4

The CD signal at 222 nm is indicative for the overall helical content and is given in units of $deg \cdot cm^2 \cdot dmol^{-1}$. m_u , m_f and m_c are the urea dependencies of $\ln k_u$, $\ln k_f$ and $\ln k_c$ respectively, multiplied by RT (see equation 1.20) (64). A_{miss} denotes the dead time absorbance change with respect to the donor-only reference.

4.4.3 Effect of Capping Motifs on the Diffusion Distance from the Helix-Coil Boundary to the Helix Center

For our calculations of the different diffusion coefficients for boundary diffusion we assumed a distinct location of the helix-coil boundary. However, theoretical and experimental work on the helix-coil transition revealed that α -helices follow a multi-state transition (140, 168-171, 187-189). Consequently, the boundary is broadly distributed and $\langle l^2 \rangle$ denotes an average diffusion distance over an ensemble of different helical conformations. The determination of the diffusion coefficient relies strongly on the correct diffusion distance. A quantitative evaluation of the average boundary position can be obtained by using the Lifson-Roig model for the helix-coil transition. The Lifson-Roig model assigns statistical weights for residue conformations and depending on the conformations of surrounding residues there are three different statistical weights. Residues in a helical segment have a statistical weight of w . Coil residues are used as a reference and have a weight of 1. Helical residues between coil and helical conformations are assigned weights of v . We use the statistical weights for helix propagation w and nucleation v according to Rohl *et al.* (Tab. 1.1) (162). Additional weights are introduced into the model to account for capping effects at the helix ends (162, 176, 178). We consider that the TTET labels have similar helix propensities as tryptophan for Nal and glutamine for Xan. A 4-fold increase in N-capping propensity of N-succinyl and a 3-fold increase in C-capping propensity of C-2-aminoethylamide (Aea) is assumed with respect to N-acetyl and C-amide, which is comparable to an alanine \rightarrow aspartate or alanine \rightarrow arginine substitution (Tab. 1.1) (162, 176).

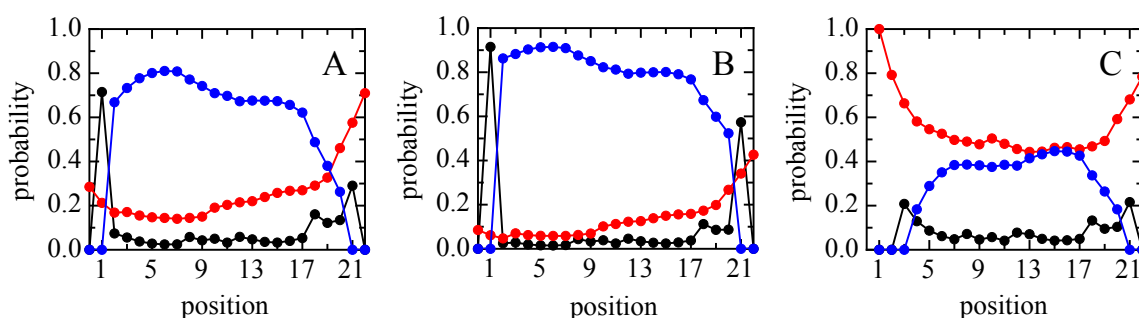


Figure 4.23: Predicted position-dependent helix and random coil content of helical peptides with different capping motifs. The probability of each residue being helical (blue), coil (red) and at the helix-coil boundary (black) as predicted by the Lifson-Roig theory with the parameters given in table 1.1. (A) Peptide of 21 aa with N-acetyl and C-amide, (B) N-succinyl and C-2-aminoethylamide or (C) with free N-terminus and C-amide.

A position-dependent helix and coil content as predicted by Lifson-Roig theory with the parameters given in table 1.1 is shown in figure 4.23. The helix-coil boundary position in a peptide with neutral, uncharged termini is broadly distributed at the C-terminus (between position $n-4$ and n) and distinctly located at the N-terminus at position 1 (Fig. 4.23A). Thus, the distance from the boundary to the helix center is shorter from the C-terminus than from the N-terminus and consequently helix unfolding in the center is more likely from the C-terminus. This result was also shown by NMR and position-dependent TTET experiments (170, 171). Hence, helix unfolding in the center should be dominated by boundary diffusion from the C-terminus, due to a shorter average diffusion distance. Accordingly, the prefactor in equation 4.16 changes to a value between 4 and 2, which results in a larger diffusion coefficient for boundary diffusion (see section 4.1.3). The helix content in the peptide with stabilizing capping motif is increased and here the boundary is distinctly located at both termini (position 1 and n) as we assumed in section 4.4.2 (Fig. 4.23B). However, helix unfolding in the center should be dominated by boundary diffusion from the C-terminus due to a lower probability of the boundary. The peptide with destabilizing capping motif has the lowest helix content with a broadly distributed boundary at both termini (between position 2 and 5 and $n-4$ and n) (Fig. 4.23C). Accordingly, helix unfolding in the center is dominated by boundary diffusion from both termini but is more likely from the charged N-terminus.

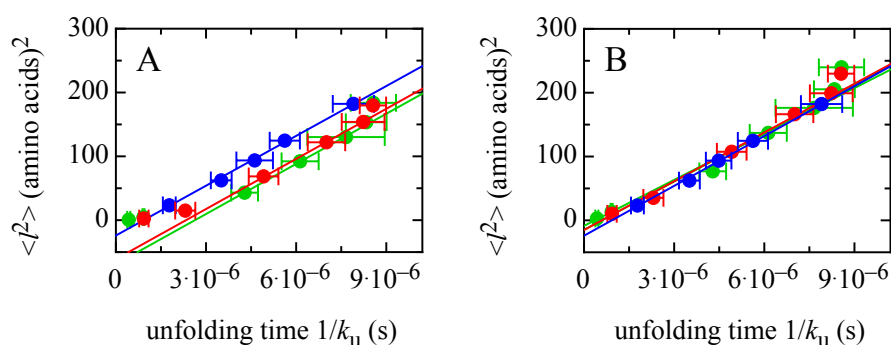


Figure 4.24: Correlation between the distance of boundary diffusion determined by the Lifson-Roig model and the experimentally determined time constant for helix unfolding for different capping motifs. Effect of the diffusion distance $\langle l^2 \rangle$ on the helix unfolding time $1/k_u$ in the central region of peptides with stabilizing (red), destabilizing (blue) and neutral, uncharged capping motif (green) at 5 °C. The average diffusion distances, l , were calculated by the Lifson-Roig theory. We used either the average distance from one boundary (N- or C-terminal) (A) or the mean value from both boundaries (N- and C-terminal) to the helix center (B). The different plots of $\langle l^2 \rangle$ vs. $1/k_u$ are linear, indicating that boundary diffusion can be described by a diffusive process (Eq. 4.1). The solid lines represent fits of equation 4.16 to the data.

The average position of the helix-coil boundary is the weighted mean of all probabilities and is determined for all peptide lengths and capping motifs (Eq. 3.6). A plot of the calculated average diffusion distance $\langle l^2 \rangle$ using Lifson-Roig theory against the experimentally determined helix unfolding times $1/k_u$ in the center of individual peptides is also linear for all capping motifs (Fig. 4.24). First, we considered only the shortest average diffusion distance from either the N- or C-terminal boundary to the helix center (Fig. 4.24A). There is a deviation from linearity at shorter peptides leading to a negative offset for all capping motifs. This indicates that the diffusion distances are not well described by the parameters of the Lifson-Roig model. Comparing the predicted diffusion distances between the different capping motifs shows that the individual diffusion distances in peptides with neutral and stabilizing capping motif are smaller than in the peptides with destabilizing capping motif with respect to the CD signal at 222 nm (Tab. 4.6, 4.7). Additionally, the peptides with a free N-terminus yield a smaller y-offset than the peptides with neutral and stabilizing capping motifs. This suggests that the c -value of arginine is too large because in the more stable peptides helix unfolding in the center should be dominated by boundary diffusion from the C-terminus due to a shorter average distance. The c -values are principally not so well characterized in the literature as the n -values. Moreover, Baldwin and co-workers observed that the c -values do not significantly vary among the different amino acids because of low preferences for the C-cap position (162, 165, 177, 245).

However, α -helices follow a multi-state transition which indicates that there are multiple equilibrium conformations with different distances from the N- and C-terminal boundary to the helix center (140, 168-171, 187-189). In order to obtain contributions from both termini we used the arithmetic mean of the diffusion distances from both N- and C-terminal boundaries to the helix center (Fig. 4.24B). This plot shows the same deviation from linearity above a helix length of 31 aa as described before and yields a y-intercept close to zero demonstrating that helix unfolding in the center is caused by boundary diffusion from both termini. Moreover, this plot shows that the individual diffusion distances are either increased by the N-succinyl and C-2-aminoethylamide group or decreased by the N-NH₃⁺ group. Using the average distances from one or both termini has no dramatic effect on the diffusion coefficient for boundary diffusion.

Concluding, the diffusion distances are well predicted by the parameters of the Lifson-Roig model when we consider an average diffusion distance from both boundaries to the helix center as is approximated in equation 4.16. However, for the peptides with a free

N-terminus we considered an average distance from the N-terminal boundary because of a shorter, average distance to the helix center. Moreover, the positively charged N-terminus is the major driving force for helix destabilization with respect to the helix dipole. Nevertheless, this theoretical approach also reveals that there is no impact of capping motifs on the diffusion coefficient for boundary diffusion at 5 °C with $D \approx 6.4 \cdot 10^6 \text{ aa}^2 \text{ s}^{-1}$ or $1.4 \cdot 10^{-9} \text{ cm}^2 \text{ s}^{-1}$ (Tab. 4.8). However, we could show that capping motifs affect the diffusion distance $\langle l^2 \rangle$ from the boundary to the helix center. For the calculation of the diffusion coefficient, only peptides between 15 aa and 27 aa are considered for the stabilizing capping motif whereas all peptide lengths are considered for the destabilizing capping motif (Fig. 4.24B). For the neutral, uncharged capping motif peptides between 11 aa and 29 aa are considered. The diffusion coefficients predicted by LR-theory are close to the assumption with a distinct location of the boundary. This demonstrates that there is no large discrepancy between the assumed and predicted diffusion distances from LR-theory (see section 4.4.2).

Table 4.8: Comparison of the diffusion coefficient for boundary diffusion in peptides with different capping motifs obtained by different approaches.

N-cap	C-cap	Diffusion coefficient ($\text{cm}^2 \text{ s}^{-1}$)	Diffusion coefficient (LR) ($\text{cm}^2 \text{ s}^{-1}$)
NH ₃	NH ₂	$1.06 \pm 0.09 \cdot 10^{-9}$	$1.46 \pm 0.13 \cdot 10^{-9}$
Ac	NH ₂	$1.07 \pm 0.07 \cdot 10^{-9}$	$1.42 \pm 0.08 \cdot 10^{-9}$
Suc	Aea	$1.08 \pm 0.09 \cdot 10^{-9}$	$1.44 \pm 0.10 \cdot 10^{-9}$

The diffusion distance was either assumed or calculated by Lifson-Roig (LR) theory. The average position of the helix-coil boundary was the weighted mean of all probabilities (Eq. 3.6). The experiments were performed at 5 °C. **NH₃** = free N-terminus, **NH₂** = amide, **Ac** = acetyl, **Suc** = succinyl, **Aea** = 2-aminoethylamide.

4.4.4 Effect of Capping Motifs on the Activation Energy for Boundary Diffusion

To test whether capping motifs locally increase the energy barrier encountered by boundary diffusion, we studied the effect of temperature on the diffusion coefficient for boundary diffusion for all capping motifs. Therefore, we measured helix-coil dynamics in peptides of various lengths with different N- and C-caps between 5 °C and 35 °C.

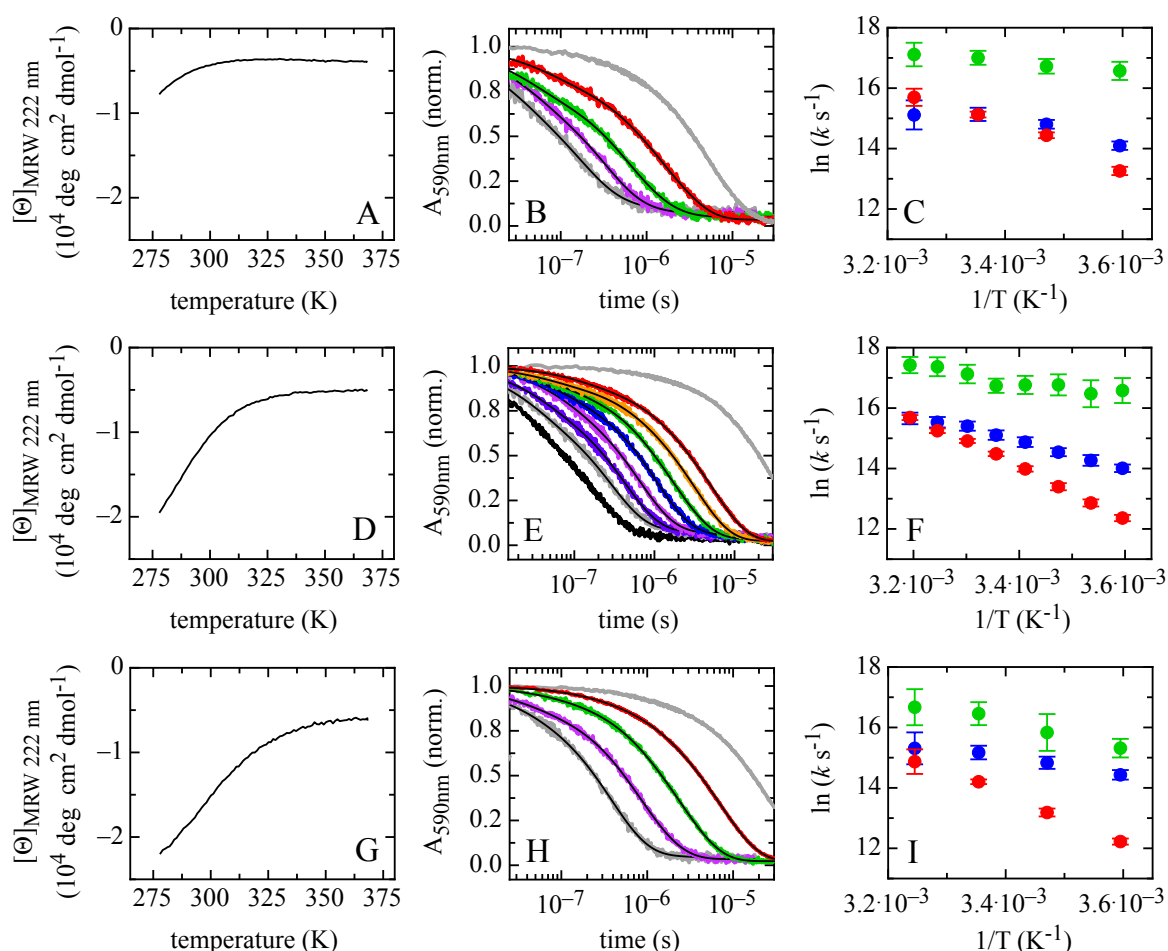


Figure 4.25: Effect of temperature on helix-coil dynamics and stability in the peptide center. Peptide of 21 aa with a destabilizing (upper panel) and stabilizing capping motif (lower panel) with respect to the reference (middle panel). (A, D, G) Thermal unfolding transitions monitored by the change in ellipticity at 222 nm. (B, E, H) TTET kinetics monitored by the triplet absorbance of xanthone at 590 nm at 5 °C (red), 15 °C (green), 25 °C (purple) and 35 °C (grey). The grey line represents the triplet lifetime at 5 °C for a donor-only peptide as reference. The black lines represent triple-exponential fits to the kinetics. (C, F, I) Rate constant for helix folding k_f (blue), unfolding k_u (red) and contact formation k_c (green) obtained by a global fit using the analytical solution of the three-state model. The rate constants in the Arrhenius plot are not viscosity-corrected.

Figure 4.25 shows the thermal stability of a peptide with 21 aa and destabilizing (A), neutral (D) or stabilizing (G) capping motif monitored by the change in ellipticity at 222 nm. The CD signal of all peptides decreases with increasing temperature, which is indicative of a loss in helical structure. The peptide with destabilizing capping motif has a

smaller ellipticity and is unfolded at lower temperatures than the peptide with a neutral capping motif, whereas the peptide with stabilizing capping motif has a larger ellipticity and unfolds at higher temperatures (Fig. 4.25A, D, G). Thus, a positively charged N-terminus leads to a lower thermal stability, whereas a negatively charged N-cap and positively charged C-cap leads to a higher thermal stability of the helix. From the thermal transition curves we can conclude that most of the peptides exhibit a significant amount of helical structure until 35 °C (Fig. A9, A10).

We measured the TTET kinetics in the helix center at various temperatures to determine the microscopic rate constants for helix folding, unfolding and contact formation for all capping motifs (Fig. 4.25B, E, H). The corresponding rate constants k_f , k_u and k_c are shown in figure 4.25 C, F and I. The more stable peptide with stabilizing capping motif shows the same linear dependence of $\ln k$ vs. $1/T$ as described before (Fig. 4.11C), whereas the less stable peptide with destabilizing capping motif show a pronounced curvature for k_f and k_u in the Arrhenius plot (Fig. 4.25C). The rate constant for contact formation shows generally a weak temperature-dependence as described previously with apparent activation energies of 15 kJ mol⁻¹ (destabilizing capping motif) and 33 kJ mol⁻¹ (stabilizing capping motif), which is in agreement with apparent activation energies found for loop formation in unstructured peptides (Fig. 4.25C, F, I) (85, 211, 212).

Figure 4.26A, B shows the relation of the diffusion distance $\langle l^2 \rangle$ with the helix unfolding time $1/k_u$ of each peptide at different temperatures. The plots are linear at all temperatures indicating that helix-coil dynamics can be described by a diffusional process for all temperatures and capping motifs (Eq. 4.1). We assume a change in the diffusion distance with temperature of 1 aa per 10 °C as stated before. The corresponding plot of $\log D$ vs. $1/T$ shows that there is no impact of capping motifs on the diffusion coefficient for boundary diffusion over the whole temperature range (Fig. 4.26C, D, A11). We analyzed the temperature dependence with two different approaches. A classical Arrhenius analysis (Eq. 4.8) reveals an enthalpic barrier after viscosity correction of $E_a = 48.2 \pm 3.7$ kJ mol⁻¹ for the stabilizing capping motif and $E_a = 47.7 \pm 7.4$ kJ mol⁻¹ for the destabilizing capping motif (Tab. 4.9). An Arrhenius-like analysis from R. Zwanzig as described above (Eq. 4.10) reveals an energy barrier of $E_a = 24.1 \pm 1.9$ kJ mol⁻¹ for peptides with stabilizing capping motif and $E_a = 23.9 \pm 3.7$ kJ mol⁻¹ for peptides with destabilizing capping motif.

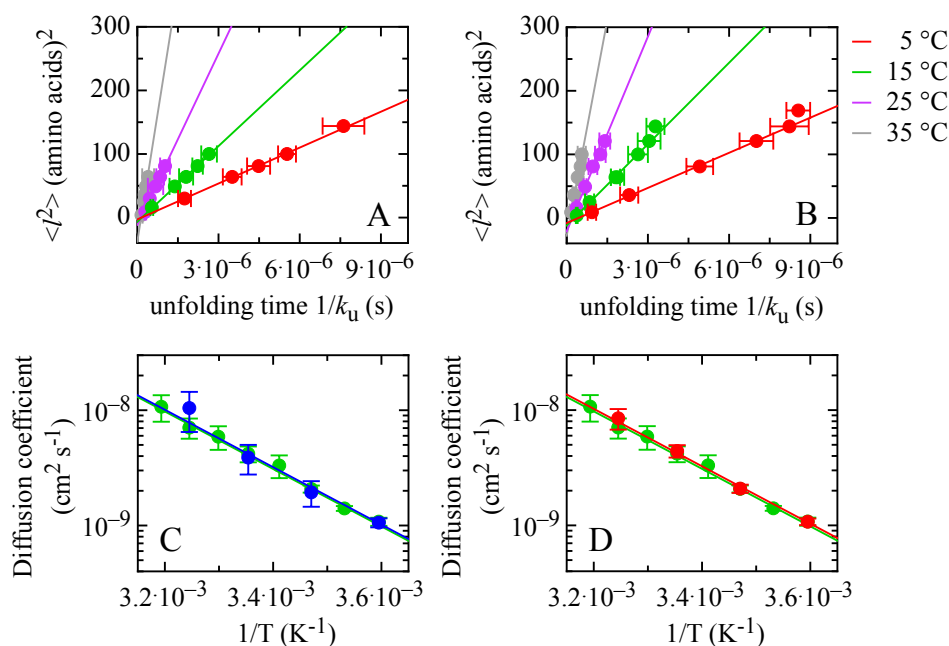


Figure 4.26: Temperature dependence of the diffusion coefficient for helix-coil boundary diffusion for different capping motifs. Correlation between the distance of boundary diffusion $\langle l^2 \rangle$ and the time constant for helix unfolding $1/k_u$ of all peptides with destabilizing (A) and stabilizing capping motif (B) at different temperatures. Effect of destabilizing (C) and stabilizing capping motif (D) on the temperature dependence of the diffusion coefficient for boundary diffusion. The diffusion coefficients are viscosity-corrected using $\alpha = 0.5$. The solid line represents a fit of equation 4.8 and equation 4.10 to the data.

Table 4.9: Effect of capping motifs on the activation energy for boundary diffusion obtained by different approaches.

N-cap	C-cap	Zwanzig (kJ mol ⁻¹)	Arrhenius (kJ mol ⁻¹)	Zwanzig (LR) (kJ mol ⁻¹)	Arrhenius (LR) (kJ mol ⁻¹)
NH ₃	NH ₂	23.9 ± 3.7	47.7 ± 7.4	24.4 ± 2.7	48.8 ± 5.6
Ac	NH ₂	23.9 ± 1.6	47.7 ± 3.3	31.9 ± 1.4	63.9 ± 2.9
Suc	Aea	24.1 ± 1.9	48.2 ± 3.7	29.1 ± 1.9	58.2 ± 3.8

The diffusion distance was either assumed or calculated using the predictions from Lifson-Roig (LR) theory. The average position of the helix-coil boundary was the weighted mean of all probabilities (Eq. 3.6). The activation energy was determined according to Arrhenius (Eq. 4.8) and Zwanzig (Eq. 4.10). **NH₃** = free N-terminus, **NH₂** = amide, **Ac** = acetyl, **Suc** = succinyl, **Aea** = 2-aminoethylamide.

The results show that capping motifs do not affect the energy barrier and the diffusion coefficient for boundary diffusion (Tab. 4.8, 4.9). This suggests that end-capping motifs change helix stability in the center by elongating the helix and thereby slow down helix unfolding because of increased diffusion distances from the helix-coil boundary to the helix center. However, we assume a distinct location of the boundary and a distinct change of the diffusion distance with temperature of 1aa per 10 °C. The determination of the diffusion coefficient and activation energy for boundary diffusion relies strongly on the correct diffusion distance. A quantitative evaluation of the average diffusion distance

for each capping motif at any temperature can be obtained by the Lifson-Roig (LR) model for the helix-coil transition as described in section 4.4.3. The propagation parameter w is temperature-dependent and we assume a change in enthalpy of $\Delta H = 4200 \text{ J mol}^{-1}$ per residue according to Scholtz *et al.* (160) (Eq. 4.17).

$$w(T) = w_0(T) \cdot e^{\left(\frac{-\Delta H}{RT}\right)} \quad (4.17)$$

Here, $w(T)$ is the propagation parameter at the respective temperature T , $w_0(T)$ is the propagation parameter at 273.15 K and ΔH is the change in w with temperature. All other parameters are temperature-independent and were not changed during the calculations.

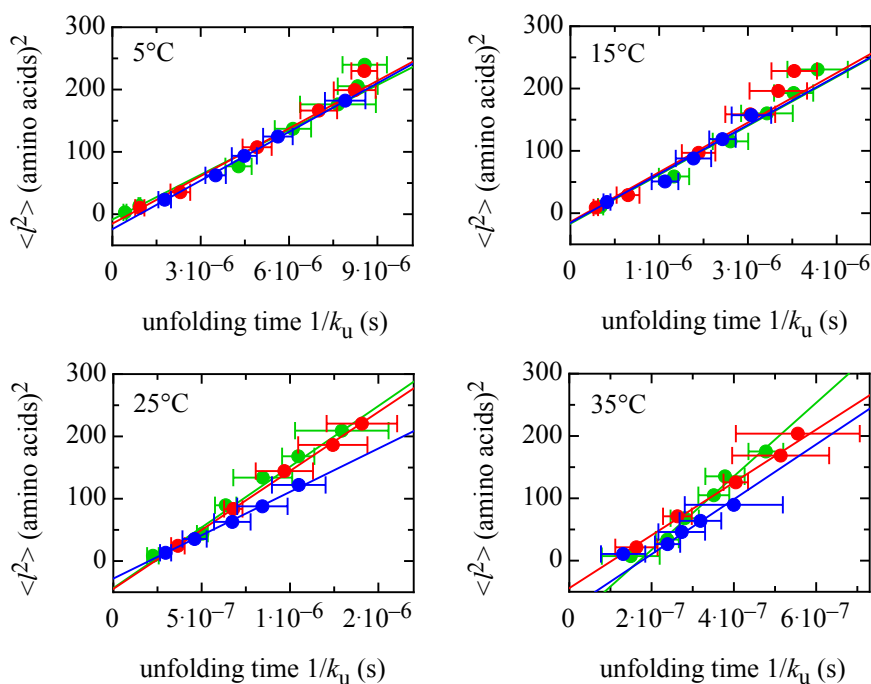


Figure 4.27: Correlation between the distance of boundary diffusion and the time constant for helix unfolding with respect to different capping motifs and temperatures. Effect of the diffusion distance $\langle l^2 \rangle$ on the helix unfolding time $1/k_u$ in peptides with N-succinyl and C-2-aminoethylamide (red), free N-terminus and C-amide (blue) or N-acetyl and C-amide (green) at different temperatures. The average diffusion distances, l , of the boundaries were predicted by the Lifson-Roig theory. The different plots of $\langle l^2 \rangle$ vs. $1/k_u$ are linear, indicating that boundary diffusion can be described by a diffusion process (Eq. 4.1). The solid lines are fits of equation 4.16 to the data.

The average distance at the respective temperature is calculated as described above and here we considered the mean diffusion distance from both N- and C-terminal boundaries to the helix center for all capping motifs. Figure 4.27 shows the plots of the predicted average diffusion distances $\langle l^2 \rangle$ against the experimentally observed helix unfolding

times $1/k_u$ at 5 – 35 °C. All plots are linear with a small negative y-offset. However, at 25 °C this offset increases, which indicates that the diffusion distances are generally underestimated or overestimated in longer peptides. A potential reason is the temperature-dependence of the propagation parameter w . A change in enthalpy of $\Delta H = 4200 \text{ J mol}^{-1}$ per residue represents only a lower limit, since no change in the heat capacity (ΔC_p^0) for the helix-coil transition was assumed (160). Moreover, there was a broad helix-coil transition in the DSC experiments with no baselines which is difficult for determining ΔH and ΔC_p^0 .

Irrespective of the w -value, the predictions do not show any impact of N- and C-capping motifs on the diffusion coefficient for boundary diffusion at all temperatures (Fig. 4.27). Accordingly, capping motifs do not alter the energy barrier of boundary diffusion (Fig. 4.28). The effect of the helix propensity (w -value) on the diffusion distance should be identical for all capping motifs and thus the magnitude of the w -value has no influence on the qualitative result. Moreover, using the shortest average distances from either the N- or C-terminal boundary to the helix center has no impact on the diffusion coefficient and activation energies but yields larger offsets (Fig. A12, A13, Tab. A2). The activation energy obtained by predictions based on the LR-model is in the range of the activation energies determined by assuming a change in the diffusion distance with temperature of 1 aa per 10 °C demonstrating that our assumption is reasonable (Tab. 4.9). The destabilizing capping motif show smaller activation barriers for boundary diffusion but this is due to the large error at 35 °C (Fig. 4.28).

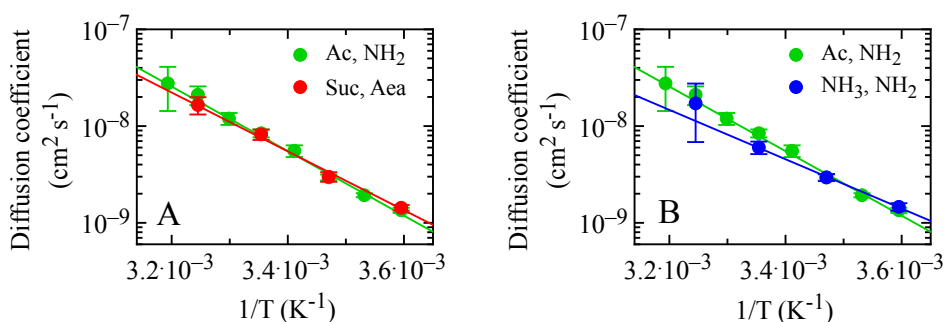


Figure 4.28: Temperature dependence of the diffusion coefficient for helix-coil boundary diffusion for different capping motifs by using the Lifson-Roig theory. Effect of stabilizing (A) and destabilizing capping motif (B) on the diffusion coefficient of boundary diffusion with respect to temperature. The diffusion coefficient was determined with the calculated average diffusion distances of the Lifson-Roig theory. The solid line represents a fit of equation 4.8 and 4.10 to the data.

The results of both approaches demonstrate that capping motifs stabilize α -helices by elongation of the diffusion distance $\langle l^2 \rangle$ from the boundary to the helix center. Several

studies revealed that the stability effect of capping motifs arises from both electrostatic and hydrogen bond interactions while others indicated that it is purely electrostatic (143, 144, 162-167, 173-179, 181-186, 246, 247). Thus, helix elongation can be performed by side-chain to backbone hydrogen bonding to unsatisfied NH donor and CO acceptor groups at the ends of the helix or by attractive electrostatic interactions with the helix dipole. In order to investigate the origin of helix elongation we screened the properties of the charge-helix dipole interaction by increasing concentrations of sodium chloride (NaCl).

4.4.5 Contribution from Charges to the Effect of Capping Motifs on Helix Stability

The biggest effect of charge-helix dipole interactions on helix stability is at the N-cap and C-cap position but the nature of this effect has been debated controversially. Previous studies suggested that the helix dipole effect arises from both hydrogen bond and electrostatic interactions while others indicated that it is purely electrostatic (143, 144, 162-167, 173-186, 246, 247). Moreover, Doig and co-workers reported that the biggest effect on helix stability at the N-cap position is due to an almost linear geometry of hydrogen bonds in contrast to helical positions (N1, N2) (179, 182-184). Our results indicate that capping motifs stabilize α -helices non-locally in the center by helix elongation. We investigate the contributions from hydrogen bonds and electrostatic interactions to the effect of capping motifs on helix stability by increasing concentrations of NaCl.

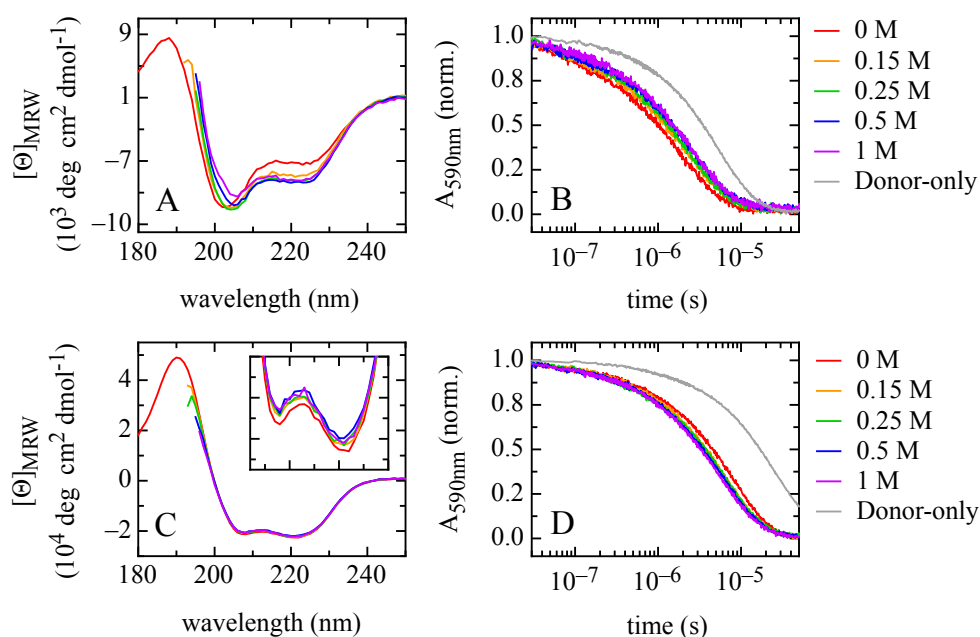


Figure 4.29: Effect of ionic strength on stability and dynamics in the center of helical peptides. Salt dependence of a helical peptide with 21 aa and destabilizing (upper panel) or stabilizing capping motif (lower panel). Far-UV CD spectra (A, C) and the corresponding TTET kinetics in the helix center (B, D) were monitored at 5 °C in various concentrations of NaCl.

The effect of NaCl on global helix content and stability is studied by far-UV CD spectroscopy and TTET (Fig. 4.29). The peptide of 21 aa with a free, positively charged N-terminus is stabilized by increasing concentrations of NaCl as demonstrated by the increase in the CD band at 222 nm (Fig. 4.29A). Likewise, TTET in the helix center is slowed down with increasing ionic strength because of an increased diffusion distance

from the boundary to the helix center (Fig. 4.29B). In contrast, the peptide of 21 aa with a negatively charged N-cap and positively charged C-cap shows the opposite effect. Here, the helix is destabilized with increasing concentrations of NaCl as indicated by the decrease in the CD band at 222 nm and TTET in the helix center is accelerated by NaCl because of a decreased diffusion distance from the boundary (Fig. 4.26C, D). Thus, the helix stability effect in both peptides can be screened by increasing concentrations of NaCl, which is a property of electrostatic interactions. However, hydrogen bond interactions are independent of the ionic strength of the solution and cannot be screened by NaCl (173, 191). The charge-helix dipole interaction in both peptides is completely screened by 1 M NaCl (Fig. 4.29). At 1 M NaCl, TTET in the center of the peptide with a stabilizing capping motif is identical to the peptide with neutral, uncharged termini, which indicates that the helix-stabilizing effect of N-succinyl and C-2-aminoethylamide is entirely electrostatic as was also shown previously (246) (Fig. 4.30). However, the peptide with a destabilizing capping motif does not reproduce the triplet lifetime of the peptide with neutral, uncharged termini at 1 M NaCl suggesting that there are additional contributions from hydrogen bond interactions (Fig. 4.30). An additional hydrogen bond interaction in the peptide with a free N-terminus can be ascribed to the fact that an acetylation or succinylation of the N-terminus produces one additional amide group. This missing hydrogen bond leads to a shorter helix and faster TTET in the peptide center as compared to the other capping motifs.

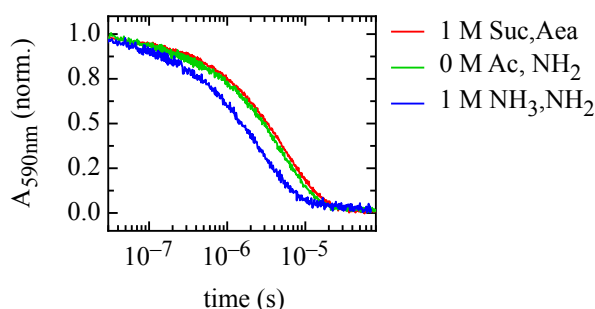


Figure 4.30: Comparison of the effect of NaCl on the triplet lifetime in the center of helical peptides with different capping motifs. Effect of NaCl on the TTET kinetics in the center of a peptide with 21 aa and destabilizing (blue) or stabilizing capping motif (red) in comparison to a peptide with neutral, uncharged termini (green). The helix-stabilizing effect of N-Suc and C-Aea (red) is completely screened by 1 M NaCl, which reproduces the triplet lifetime of the peptide with uncharged termini (green). This indicates that the stabilizing interactions of N-Suc and C-Aea are entirely electrostatic. The helix-destabilizing effect of N-NH₃⁺ and C-NH₂ (blue) is not completely screened by 1 M NaCl and therefore does not reproduce the triplet lifetime of the peptide with uncharged termini. This suggests that the destabilizing interactions of the N-NH₃⁺ group are not entirely electrostatic. An additional contribution from hydrogen bond interactions can be ascribed to a missing hydrogen bond which is formed by N-terminal acetylation or succinylation. The TTET kinetics were monitored in 1 M or 0 M NaCl at 5 °C.

Thus, the results indicate that charged capping motifs stabilize α -helices in the center by electrostatic interactions with the helix dipole and not by hydrogen bond interactions to unsatisfied backbone NH donor and CO acceptor groups at the helix ends. Attractive electrostatic interactions between capping motifs and the helix dipole lead to an elongation of the helix whereas repulsive electrostatic interactions lead to a decrease in helix length. Hence, capping motifs do not affect the diffusion coefficient for boundary diffusion but change the diffusion distance to the helix center. However, uncharged, polar side-chains, which cannot interact with the helix dipole, were shown to stabilize α -helices by hydrogen bond interactions (163-166, 191).

5 Summary and Outlook

The dynamics of α -helices have been studied extensively and the kinetic mechanism of the helix-coil transition has long been under debate. Experimental and theoretical work on α -helices have shown that a linear Ising model is able to describe thermodynamic and kinetic properties of the helix-coil transition (134, 160, 168-170, 187-190, 194-196, 217). Previous triplet-triplet energy transfer (TTET) experiments between xanthone (Xan) and naphthalene (Nal) demonstrated that equilibrium helix-coil dynamics can be understood as a classical, Einstein-type, 1-D diffusion process of the helix-coil boundary along the peptide backbone leading to a position- and length-dependent rate constant for helix unfolding k_u (170, 186). A modified Einstein equation, which correlates the diffusion distance $\langle l^2 \rangle$ with the helix unfolding time $1/k_u$ in the center of individual peptides, revealed a diffusion coefficient for boundary diffusion of $D = 2.7 \cdot 10^7$ (amino acids)² s⁻¹ or $6.1 \cdot 10^{-9}$ cm² s⁻¹ (186). However, these experiments were performed in peptides with an $i,i+6$ spacing of the TTET labels which has an inherent uncertainty in defining an exact diffusion distance since it is not known, how many helical segments between the labels have to be unfolded to enable triplet transfer between Xan and Nal. Consequently, the previously determined diffusion coefficient for boundary diffusion is imprecise because the determination of the diffusion coefficient relies strongly on the correct diffusion distance.

The aim of the present study was to determine a more reliable diffusion coefficient for boundary diffusion in order to further characterize the boundary diffusion mechanism for the helix-coil transition in peptides. Therefore, we performed temperature- and viscosity-dependent TTET measurements on helical peptides of different length to elucidate whether boundary diffusion is purely diffusive or an activated process. Based on this, we tested whether internal friction effects, which are caused by intrinsic energy barriers, contribute additively to solvent friction according to current models or whether it modulates the effect of solvent viscosity on boundary diffusion as proposed by Grote and Hynes (110). Moreover, we investigated the effect of capping motifs on helix stability by analyzing the impact of capping motifs on the diffusion coefficient and diffusion distance for boundary diffusion.

A reliable determination of the diffusion coefficient for boundary diffusion is achieved by using a suitable TTET label spacing which decrease the uncertainty in the diffusion distance. Placing the labels with $i,i+2$ spacing enabled a more exact determination of the diffusion distance and revealed a diffusion coefficient for boundary diffusion of $D = 4.8 \pm$

$0.3 \cdot 10^6 \text{ aa}^2 \text{ s}^{-1}$ or $1.07 \pm 0.07 \cdot 10^{-9} \text{ cm}^2 \text{ s}^{-1}$. The results showed that helices above 31 aa contain significant contributions from coil nucleation events. Hence, TTET does not predominantly occur through boundary diffusion above this peptide length which is in accordance with previous results (186). A comparison of the results from peptides with $i,i+2$ and $i,i+6$ spacing yields a similar diffusion coefficient of $D = 1.4 \pm 0.2 \cdot 10^{-9} \text{ cm}^2 \text{ s}^{-1}$ for $i,i+6$ spacing when helix unfolding to the first TTET label is assumed to enable triplet transfer.

Previous NMR and position-dependent TTET experiments have shown that the C-terminal region of the helix is less stable than the N-terminal region (170, 171). Hence, helix unfolding in the center in $i,i+2$ peptides is dominated by boundary diffusion from the C-terminus, due to a shorter average diffusion distance to the helix center. Accordingly, the prefactor in the modified Einstein equation changes to a value between 4 and 2 which results in an upper limit for the diffusion coefficient for boundary diffusion of $D = 9.5 \pm 0.6 \cdot 10^6 \text{ aa}^2 \text{ s}^{-1}$ or $2.13 \pm 0.14 \cdot 10^{-9} \text{ cm}^2 \text{ s}^{-1}$. Thus, the elementary process of adding and removing helical segments occurs with a time constant of $1/k \approx 100 - 50 \text{ ns}$ which is in good agreement with previous simulations based on a linear Ising model (170, 186). However, helix unfolding solely by boundary diffusion from the C-terminus has to be tested experimentally by analyzing the effect of N- and C-terminal extensions on TTET in the helix center.

On the basis of the $i,i+2$ spacing approach it was possible to characterize the boundary diffusion mechanism of α -helices in more detail by analyzing the effect of solvent viscosity η and temperature T on the diffusion coefficient D . We found a weaker solvent viscosity dependence than $1/\eta$ with $\alpha = 0.5$ indicating that boundary diffusion is not fully diffusion-controlled. Temperature-dependence measurements confirmed that boundary diffusion is not exclusively limited by solvent friction with an intrinsic activation barrier of $E_a = 24$ or 48 kJ mol^{-1} depending on the model used to analyze the data and a pre-exponential factor of $A = 10^{15} \text{ s}^{-1}$. The energy barrier of the boundary diffusion mechanism is probably due to the breakage and formation of hydrogen bond interactions and steric effects from torsion angle isomerizations along the peptide backbone which were shown to be weakly dependent on solvent friction (111, 114). Moreover, we could demonstrate that the height of these local barriers is inversely proportional to the solvent viscosity dependence α ($E_a \propto 1/\alpha$) according to Grote-Hynes theory and that internal friction does not contribute additively to solvent friction, in contradiction to current models (110). Internal friction, in contrast, modulates the effect of solvent viscosity on

boundary diffusion. However, despite encountering energy barriers, boundary diffusion still follows a classical, Einstein type, 1-D diffusion law indicating that the diffusing boundary mechanism for the helix-coil transition is described by a 1-D random walk along the peptide backbone with local energy barriers.

The last part of this thesis focused on the effect of N- and C-capping motifs on helix-coil dynamics and stability. It was shown that capping motifs increase helix stability non-locally by altering helix unfolding but not refolding in the helix center (186). Up to date, the molecular origin of this non-local effect was unknown. It was suggested that capping motifs either elongate the helix, which leads to increased diffusion distances from the helix-coil boundary to the center, or slow down boundary diffusion by increased energy barriers. We investigated the effect of differently charged capping motifs located at the N-cap and C-cap position on the diffusion coefficient D and diffusion distances $\langle l^2 \rangle$ for boundary diffusion. It could be demonstrated that a negatively charged N-cap (N-succinyl) and positively charged C-cap (C-2-aminoethylamide) leads to a global stabilization of the helix, whereas a positively charged N-cap (N-NH₃⁺) leads to a global destabilization of the helix. The effect of both capping motifs on k_u could be attributed to an impact on the diffusion distance $\langle l^2 \rangle$ for boundary diffusion, which was reproduced by predictions based on the Lifson-Roig theory. However, capping motifs do not affect the diffusion coefficient D . Temperature-dependent measurements confirmed that capping motifs do not alter the energy barrier encountered by boundary diffusion. Moreover, we could demonstrate that the properties of helix stabilization and destabilization can be screened by 1 M NaCl, which indicates that charged capping motifs stabilize α -helices by electrostatic interactions with the helix dipole and not by hydrogen bond interactions with unsatisfied backbone NH donor and CO acceptor groups at the helix ends. Attractive electrostatic interactions between capping motifs and the helix dipole lead to an elongation of the helix, whereas repulsive electrostatic interactions lead to a decrease in helix length.

In the present study, we determined the diffusion coefficient for boundary diffusion in alanine-based peptides which have short side-chains. Future investigations on the impact of steric effects on boundary diffusion can be tested by incorporating bulky amino acids with C- β branched side-chains. It was shown that valine and isoleucine alter both helix folding and unfolding rate constants in the helix center indicating increased steric energy barriers in the transition state for helix formation and unfolding (186). Increased steric effects from torsion angle isomerizations should lead to a smaller diffusion coefficient

and larger activation barriers for boundary diffusion. Consequently, valine and isoleucine should lead to a smaller effect of solvent friction on boundary diffusion, since the barrier height is inversely proportional to the solvent viscosity dependence α as predicted by Grote and Hynes (110). Furthermore, increasing steric effects can be analyzed by pressure-dependence measurements where valine and isoleucine should lead to increased activation volumes for helix formation and unfolding compared to alanine (224).

Moreover, it would be interesting to investigate whether boundary diffusion is similar in proteins or whether the properties and mechanism change in the environment of a protein. Introducing helix breakers such as proline and glycine at the helix ends could mimic the environment of a protein and hence the effect on the dynamics and the diffusion coefficient for boundary diffusion can be analyzed.

6 Appendix

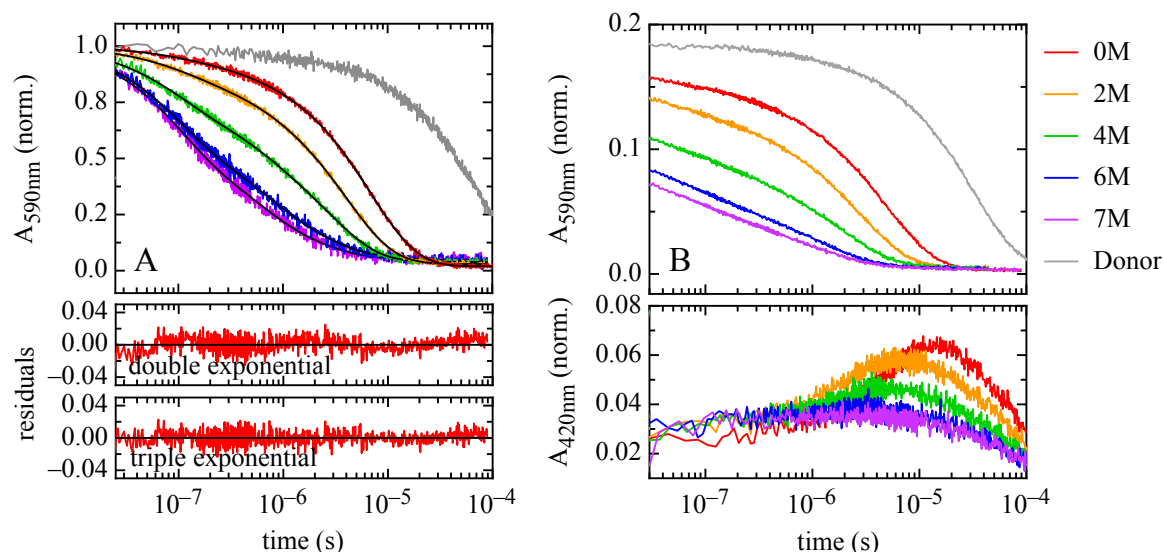


Figure A1: Effect of urea on the TTET kinetics in the central region of a helical peptide. TTET in a helical peptide of 25 aa (A) or 21 aa (B) with $i,i+2$ spacing of the TTET labels and acetylated N-terminus and amidated C-terminus. The TTET kinetics were monitored in various concentrations of urea by the triplet absorbance of xanthone at 590 nm (upper panel) and naphthalene at 420 nm (lower panel) to verify triplet transfer between donor and acceptor. The grey line represents the triplet lifetime for a donor-only peptide as reference and the black lines represent triple-exponential fits to the kinetics. The results from double- and triple-exponential fits to the TTET kinetics are shown as residuals (lower panel). TTET in longer peptides with $i,i+2$ spacing of the labels can be described by the sum of three exponentials. The dead time absorbance change with respect to the donor-only reference represents the missing amplitude (A_{miss}). All experiments were performed in 10 mM potassium phosphate buffer, pH 7.0 at 5 °C.

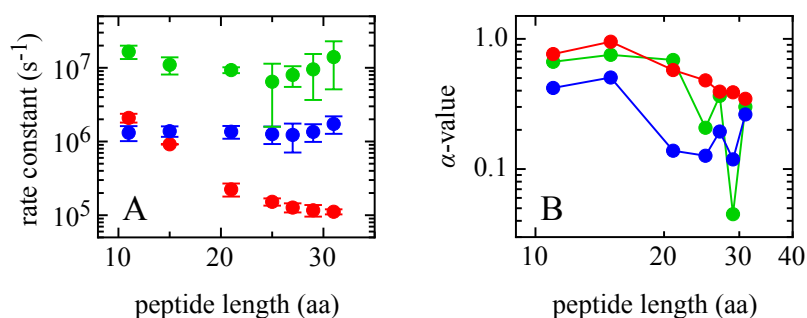


Figure A2: Effect of peptide length on helix-coil dynamics and stability in the helix center with respect to glycerol. (A) A global fit of the glycerol dependence data using the analytical solution of the three-state model yielded the rate constant for helix folding k_f (blue), unfolding k_u (red) and contact formation k_c (green) in water. (B) Effect of peptide length on the solvent viscosity dependence α for all rate constants. The errors are omitted for clarity and the solid lines represent a guide to the eye. All experiments were performed in 10 mM potassium phosphate buffer, pH 7.0 at 5 °C.

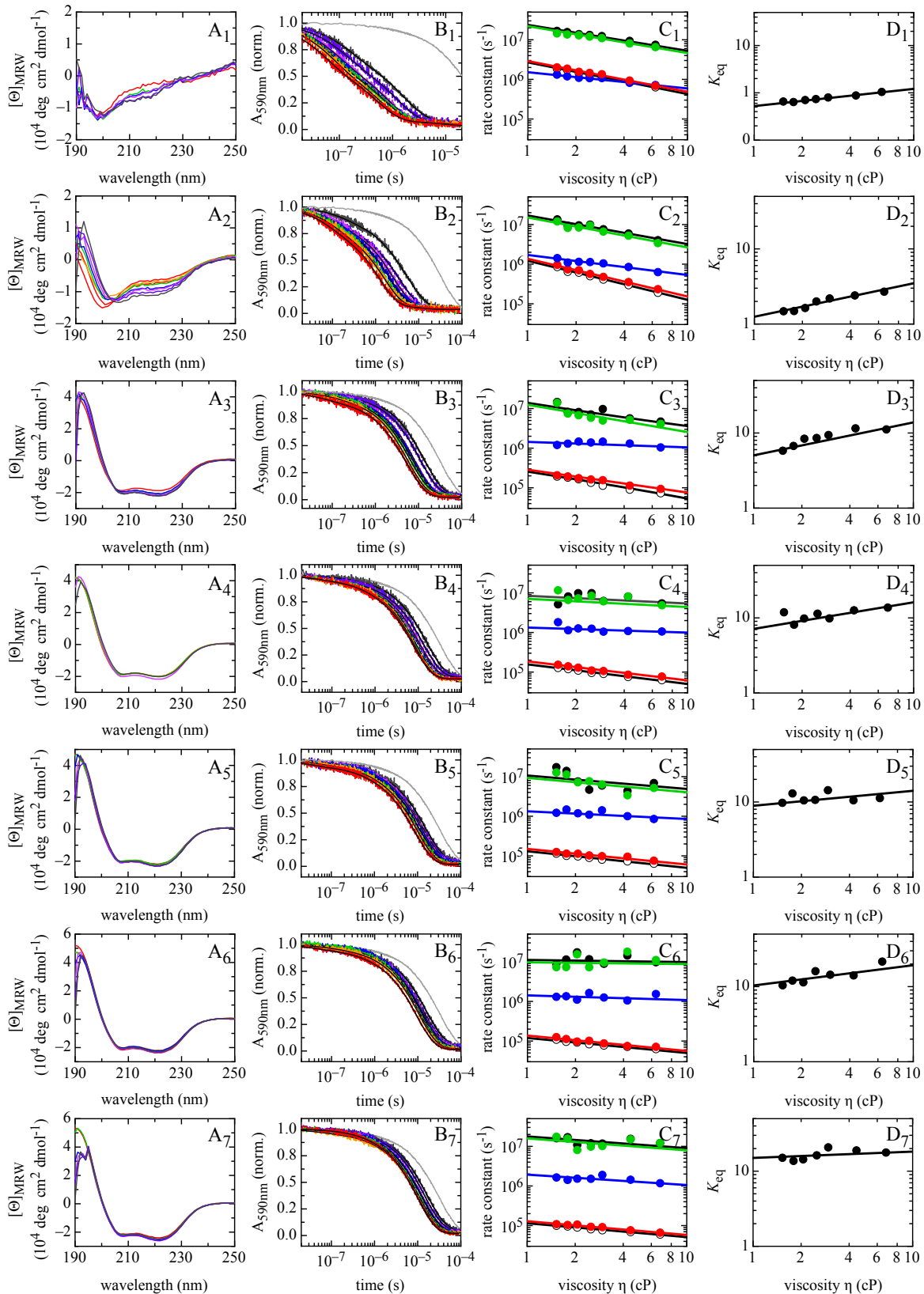


Figure A3: Effect of glycerol on helix-coil dynamics and stability in the helix center. (A) Far-UV CD spectra of helical peptides of various length (11 aa, 15 aa, 21 aa, 25 aa, 27 aa, 29 aa, 31 aa) in different concentrations of glycerol (0 – 40 % w/v). (B) TET kinetics monitored by the triplet absorbance of xanthone at 590 nm in different concentrations of glycerol. The grey line represents the triplet lifetime in water for a donor-only peptide as reference. The black lines represent triple-exponential fits to the kinetics. (C) A global fit of the observable rate constants $\lambda_{1,2}$ (black circles) using the analytical solution of the three-state model yields the rate constant of helix folding k_f (blue line), unfolding k_u (red line) and contact

formation k_c (green line). Filled circles are results from individual fits. (D) Corresponding thermodynamic stability in the helix center with respect to solvent viscosity. All experiments were performed in 10 mM potassium phosphate buffer, pH 7.0 at 5 °C.

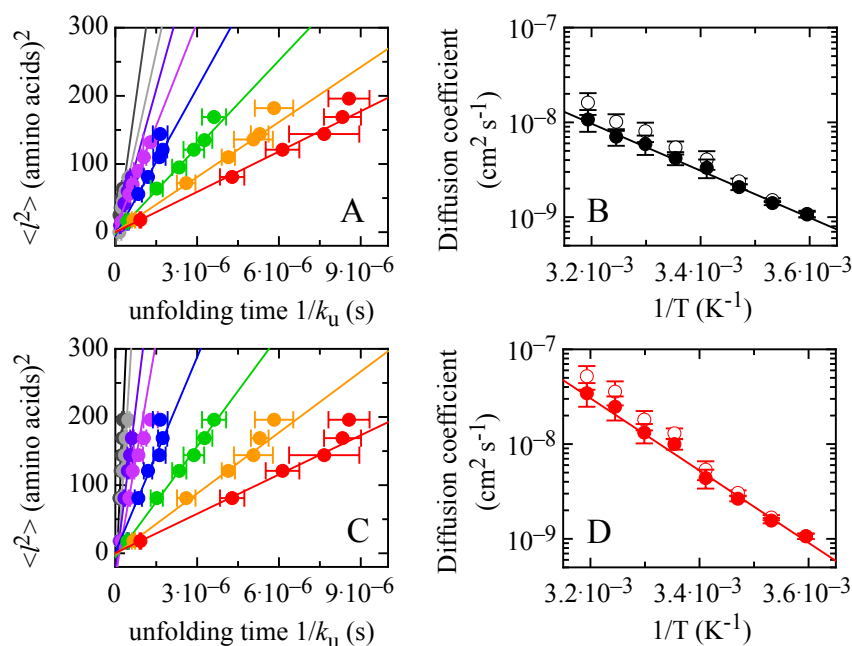


Figure A4: Temperature dependence of the diffusion coefficient for helix-coil boundary diffusion. (A, C) Correlation between the distance of boundary diffusion $\langle l^2 \rangle$ and the time constant for helix unfolding $1/k_u$ for all peptides at different temperatures (5 – 40 °C). We considered either a change in the diffusion distance of 1 aa per 10 °C (A) or no change in the diffusion distance (C) with increasing temperature. The different plots of $\langle l^2 \rangle$ vs. $1/k_u$ are linear. The solid line represents a fit of equation 4.2 to the data. (B, D) Effect of temperature on the diffusion coefficient for boundary diffusion. The black circles represent the diffusion coefficient for changed diffusion distances (B) and the red circles represent the diffusion coefficient for unchanged diffusion distances (D). Both diffusion coefficients are viscosity-corrected (filled circles) using $\alpha = 0.5$ (Eq. 4.7). The solid lines represent a fit of equation 4.8 or 4.10 to the data.

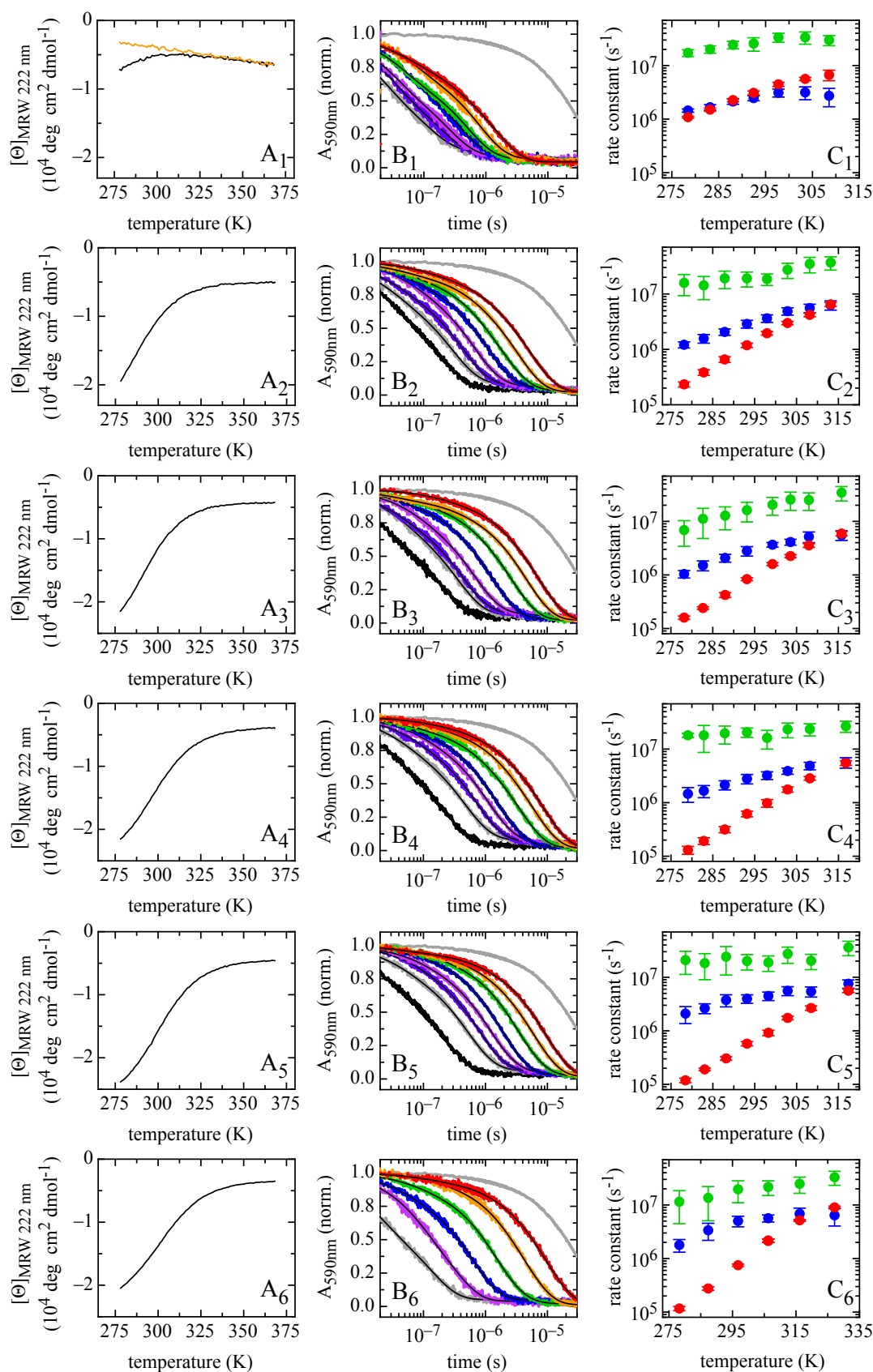


Figure A5: Effect of temperature on helix-coil dynamics and stability in the helix center. (A) Thermal unfolding transition of helical peptides of various length (15 aa, 21 aa, 25 aa, 27 aa, 29 aa, 31 aa) monitored by the change in ellipticity at 222 nm. The thermal unfolding transition of a completely unfolded peptide with 7 aa (yellow) is shown in comparison (A₁). (B) TTET kinetics monitored by the triplet absorbance of xanthone at 590 nm at different temperature (5 – 40 °C). The grey line represents the triplet lifetime at 5 °C

for a donor-only peptide as reference. The black lines represent triple-exponential fits to the kinetics. (C) A global fit of the urea dependence data using the analytical solution of the three-state model yields the rate constant of helix folding k_f (blue), unfolding k_u (red) and contact formation k_c (green) at the respective temperature.

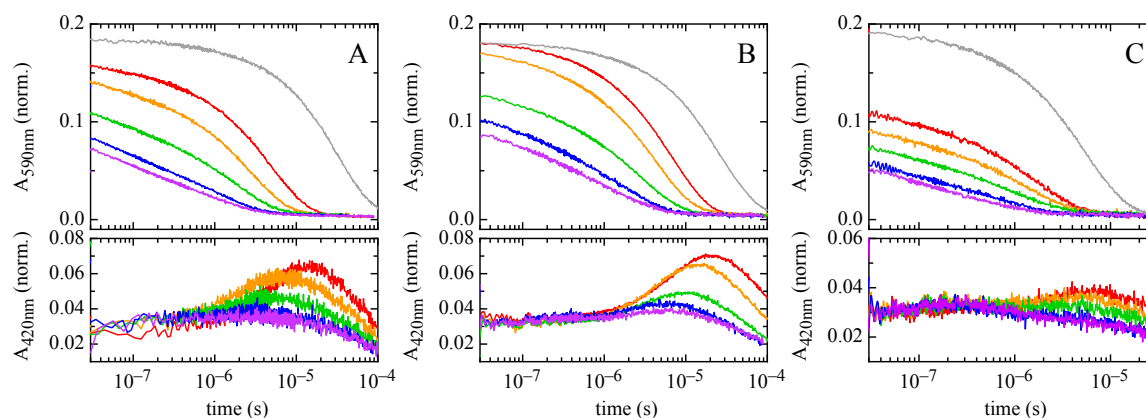


Figure A6: Effect of urea on the TTET kinetics in the central region of helical peptides with different end-capping motifs. TTET in helical peptides of 21 aa with acetylated N-terminus and amidated C-terminus (A), succinylated N-terminus and 2-aminoethylamidated C-terminus (B) or free, unblocked N-terminus and amidated C-terminus (C). The TTET kinetics were monitored in 0 M, 2 M, 4 M, 6 M and 7 M urea (red to purple) at 5 °C by the triplet absorbance of xanthone at 590 nm (upper panel) and naphthalene at 420 nm (lower panel) to verify triplet transfer between donor and acceptor. The grey line represents the triplet lifetime for a donor-only peptide as reference. The dead time absorbance change with respect to the donor-only reference represents the missing amplitude (A_{miss}).

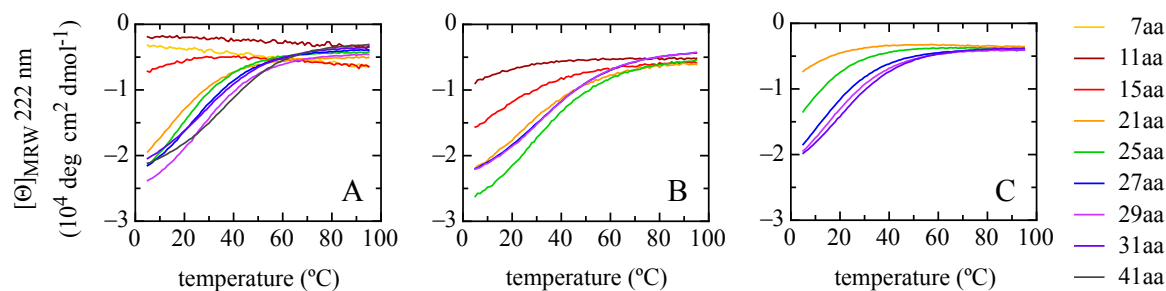


Figure A7: Effect of capping motifs on the thermal stability of helical peptides of various lengths. Thermal unfolding transition of helical peptides with acetylated N-terminus and amidated C-terminus (A), succinylated N-terminus and 2-aminoethylamidated C-terminus (B) or free, unblocked N-terminus and amidated C-terminus (C) monitored by the change in ellipticity at 222 nm.

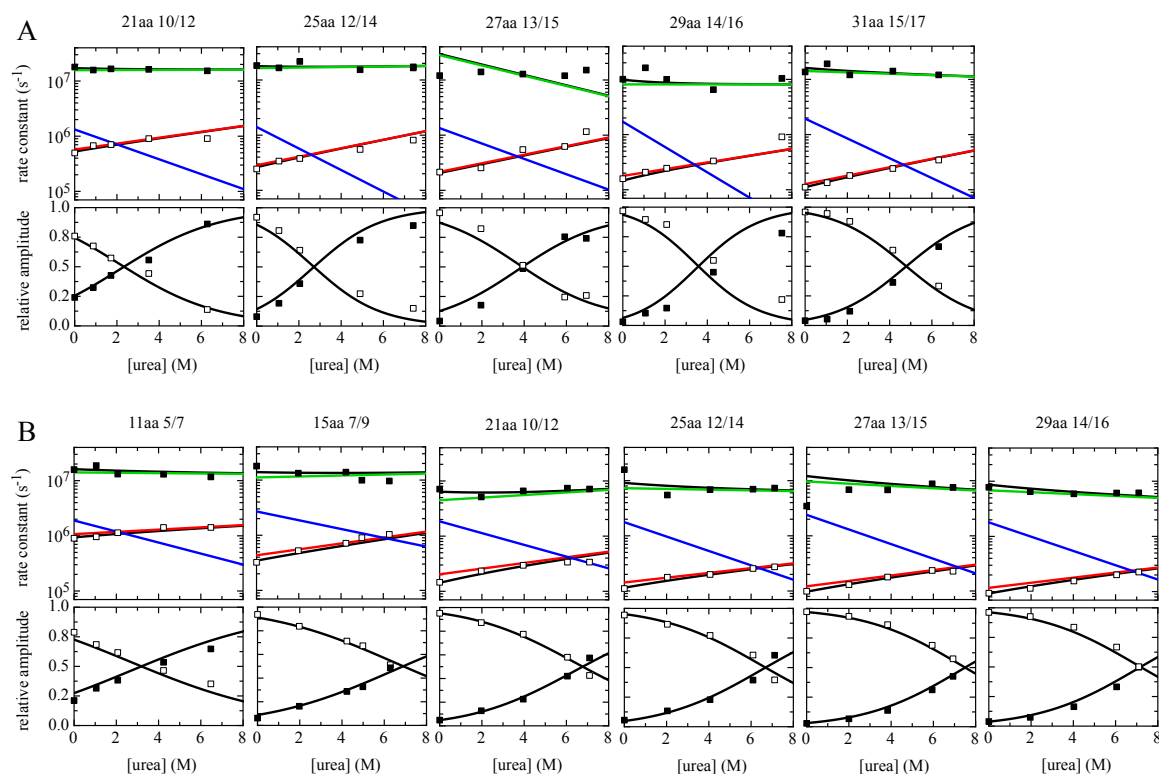


Figure A8: Urea dependence of helix-coil dynamics in the center of helical peptides with different capping motifs. (A) Peptides with destabilizing capping motif (free, positively charged N-terminus and amidated C-terminus). (B) Peptides with stabilizing capping motif (N-terminal succinate and C-terminal 2-aminoethylamide). The peptides were labeled in the center with an $i,i+2$ spacing. The squares represent the observable rate constants $\lambda_{1,2}$ (upper panel) and relative amplitudes $A_{1,2}$ obtained from individually fitting each kinetic trace (lower panel). A global fit of the observable rate constants $\lambda_{1,2}$ (black lines) and amplitudes $A_{1,2}$ (black lines) using the analytical solution of the three-state model yields the rate constant of helix folding k_f (blue line), unfolding k_u (red line) and contact formation k_c (green line). All experiments were performed in 10 mM potassium phosphate buffer, pH 7.0 at 5 °C.

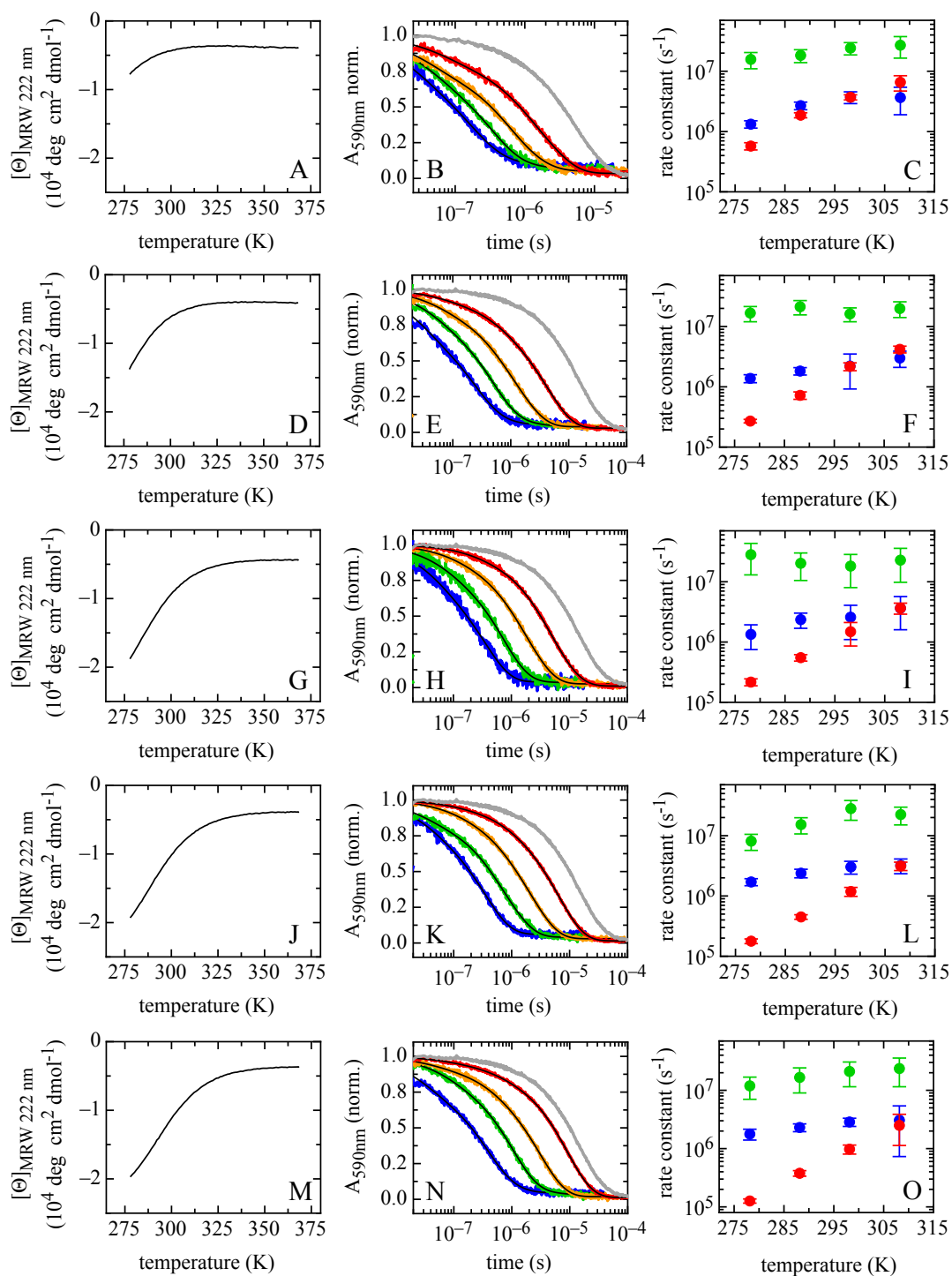


Figure A9: Effect of temperature on helix-coil dynamics and stability in the center of helical peptides with destabilizing capping motif. (A, D, G, J, M) Thermal unfolding transition of helical peptides of various length (21 aa, 25 aa, 27 aa, 29 aa, 31 aa) monitored by the change in ellipticity at 222 nm. (B, E, H, K, N) TET kinetics monitored by the triplet absorbance of xanthone at 590 nm at different temperature (5 – 35 °C). The grey line represents the triplet lifetime at 5 °C for a donor-only peptide as reference. The black lines represent triple-exponential fits to the kinetics. (C, F, I, L, O) A global fit of the urea dependence data using the analytical solution of the three-state model yields the rate constant of helix folding k_f (blue), unfolding k_u (red) and contact formation k_c (green) at the respective temperature.

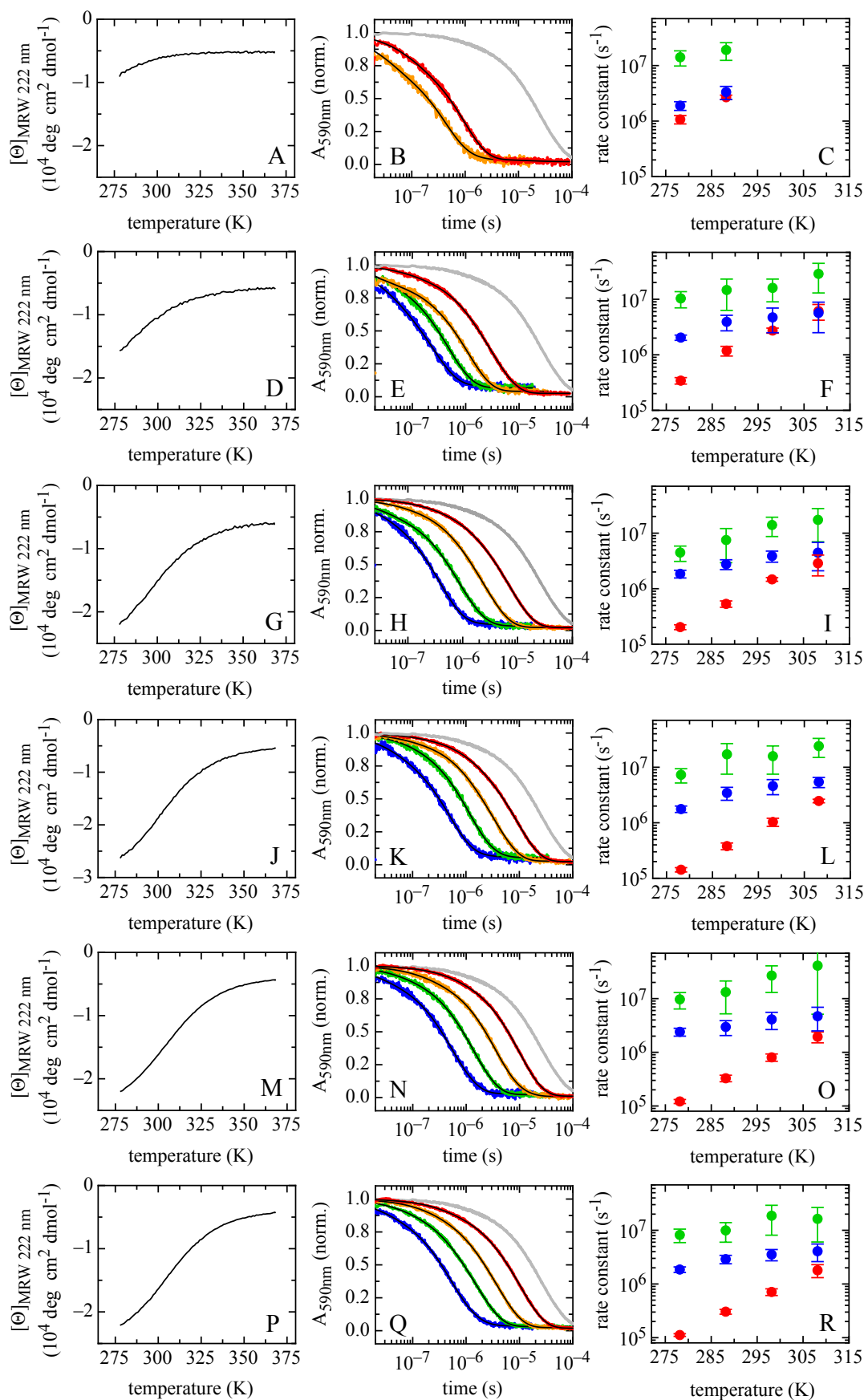


Figure A10: Effect of temperature on helix-coil dynamics and stability in the center of helical peptides with stabilizing capping motif. (A, D, G, J, M, P) Thermal unfolding transition of helical peptides of various length (11 aa, 15 aa, 25 aa, 27 aa, 29 aa) monitored by the change in ellipticity at 222 nm. (B, E, H,

K, N, O) TTET kinetics monitored by the triplet absorbance of xanthone at 590 nm at different temperature (5 – 35 °C). The grey line represents the triplet lifetime at 5 °C for a donor-only peptide as reference. The black lines represent triple-exponential fits to the kinetics. (C, F, I, L, O, R) A global fit of the urea dependence data using the analytical solution of the three-state model yields the rate constant of helix folding k_f (blue), unfolding k_u (red) and contact formation k_c (green) at the respective temperature.

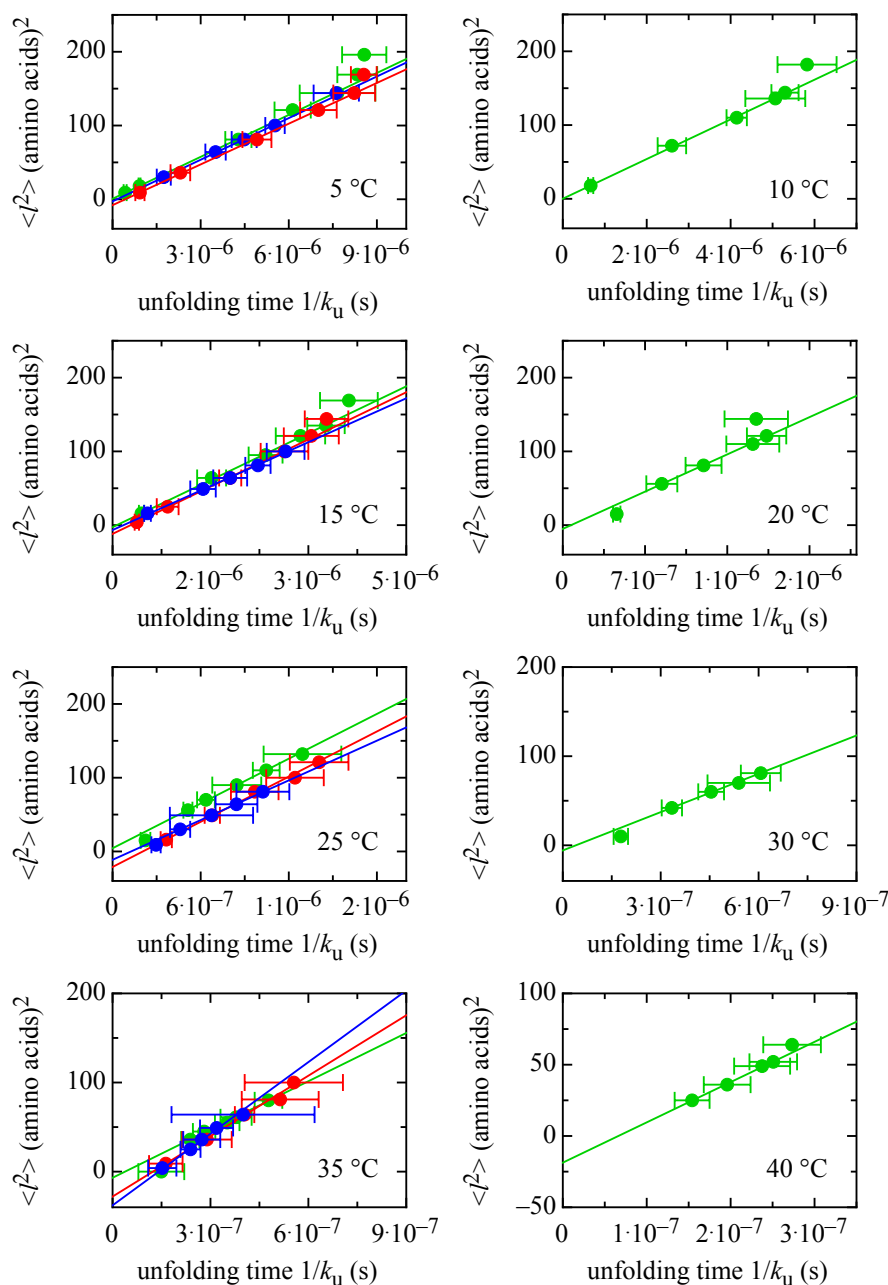


Figure A11: Correlation between the distance of boundary diffusion and the time constant for helix unfolding for different capping motifs and temperatures. Effect of the diffusion distance $\langle l^2 \rangle$ on the helix unfolding time $1/k_u$ in peptides with N-succinyl and C-2-aminoethylamide (red), free N-terminus and C-amide (blue) or N-acetyl and C-amide (green) at different temperatures. The average diffusion distance, l , from the boundaries to the helix center was assumed to change by 1 aa per 10 °C. The different plots of $\langle l^2 \rangle$ vs. $1/k_u$ are linear, indicating that boundary diffusion can be described by a diffusion process. The solid lines represent fits of equation 4.16 to the data.

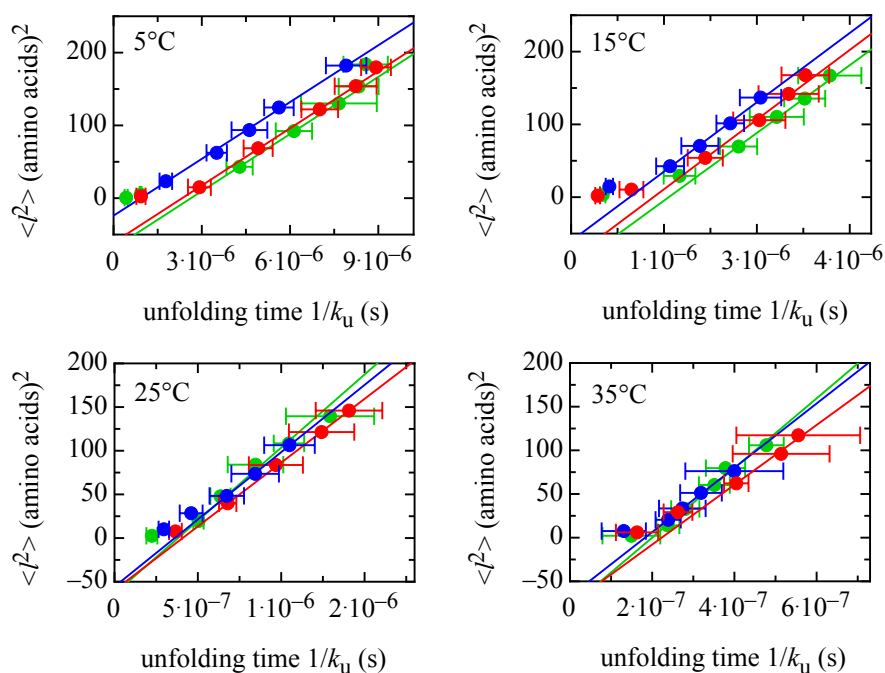


Figure A12: Correlation between the distance of boundary diffusion and the time constant for helix unfolding for different capping motifs and temperatures. Effect of the diffusion distance $\langle l^2 \rangle$ on the helix unfolding time $1/k_u$ in peptides with N-succinyl and C-2-aminoethylamide (red), free N-terminus and C-amide (blue) or N-acetyl and C-amide (green) at different temperatures. The average diffusion distances, l , of the boundaries were predicted by the Lifson-Roig theory using only the shortest average distance from one boundary to the helix center. The different plots of $\langle l^2 \rangle$ vs. $1/k_u$ are linear, indicating that boundary diffusion can be described by a diffusion process. The solid lines represent fits of equation 4.16 to the data.

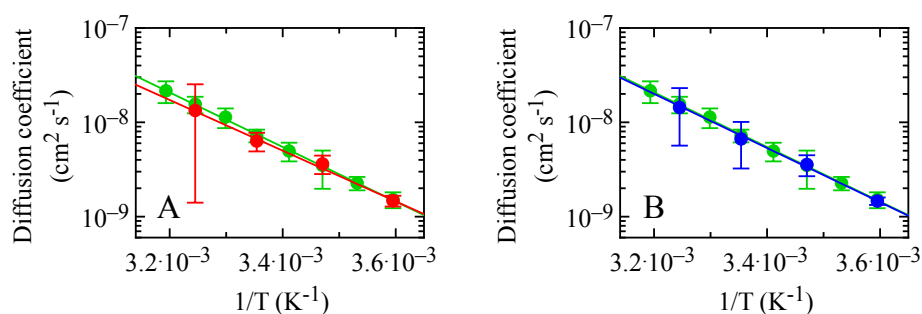


Figure A13: Temperature dependence of the diffusion coefficient for helix-coil boundary diffusion for different capping motifs. Effect of stabilizing (A) and destabilizing capping motif (B) on the diffusion coefficient for boundary diffusion at different temperatures. The average diffusion distance, l , was calculated by the Lifson-Roig theory using the average distance from one boundary (N- or C-terminal) to the helix center. The diffusion coefficients are viscosity-corrected using $\alpha = 0.5$ (Eq. 4.7). The solid line represents a fit of equation 4.8 and 4.10 to the data. The results are displayed in table A2.

Table A1: Diffusion distances of α -helical peptides for all capping motifs.

Peptide	$\langle l^2 \rangle$ (NH ₃ , NH ₂)	$\langle l^2 \rangle$ (Ac, NH ₂)	$\langle l^2 \rangle$ (Suc, Aea)
11aa	n. d.	9	25
15aa	n. d.	16	49
21aa	30	81	100
25aa	64	121	144
27aa	81	144	169
29aa	100	169	196
31aa	144	196	n. d.
41aa	n. d.	361	n. d.

The average position of the helix-coil boundary was assumed at positions 5 (NH₃, NH₂), 2 and n-1 (Ac, NH₂) or 1 and n (Suc, Aea) (with n number of aa). The average diffusion distance $\langle l^2 \rangle$ was considered from the average position of the boundary to the first TTET label. **NH₃** = free N-terminus, **NH₂** = amide, **Ac** = acetyl, **Suc** = succinyl, **Aea** = 2-aminoethylamide.

Table A2: Effect of capping motifs on the activation energy for boundary diffusion obtained by different approaches.

N-cap	C-cap	Zwanzig (kJ mol ⁻¹)	Arrhenius (kJ mol ⁻¹)	Zwanzig (LR) (kJ mol ⁻¹)	Arrhenius (LR) (kJ mol ⁻¹)
NH ₃	NH ₂	23.9 ± 3.7	47.7 ± 7.4	27.5 ± 4.8	54.9 ± 9.7
Ac	NH ₂	23.9 ± 1.6	47.7 ± 3.3	27.7 ± 2.3	55.4 ± 4.7
Suc	Aea	24.1 ± 1.9	48.2 ± 3.7	25.7 ± 4.0	51.5 ± 8.0

The activation energies were determined by either assumed diffusion distance or predicted diffusion distances using Lifson-Roig (LR) theory. The average position of the helix-coil boundary was the weighted mean of all probabilities and the shortest average distance from one boundary (N- or C-terminal) to the helix center was considered (Eq. 3.6). The activation energy was determined according to Arrhenius (Eq. 4.8) and Zwanzig (Eq. 4.10). **NH₃** = free N-terminus, **NH₂** = amide, **Ac** = acetyl, **Suc** = succinyl, **Aea** = 2-aminoethylamide.

7 References

1. Walsh CT, Garneau-Tsodikova S, & Gatto GJ, Jr. (2005) Protein posttranslational modifications: the chemistry of proteome diversifications. *Angew Chem Int Ed Engl* 44:7342-7372.
2. Anfinsen CB (1973) Principles that govern the folding of protein chains. *Science* 181:223-230.
3. Lang K, Schmid FX, & Fischer G (1987) Catalysis of protein folding by prolyl isomerase. *Nature* 329:268-270.
4. Young JC, Agashe VR, Siegers K, & Hartl FU (2004) Pathways of chaperone-mediated protein folding in the cytosol. *Nat Rev Mol Cell Biol* 5:781-791.
5. Messens J & Collet JF (2006) Pathways of disulfide bond formation in *Escherichia coli*. *Int J Biochem Cell Biol* 38:1050-1062.
6. Tompa P (2002) Intrinsically unstructured proteins. *Trends Biochem Sci* 27:527-533.
7. Fink AL (2005) Natively unfolded proteins. *Curr Opin Struct Biol* 15:35-41.
8. Goedert M (2015) NEURODEGENERATION. Alzheimer's and Parkinson's diseases: The prion concept in relation to assembled A β , tau, and alpha-synuclein. *Science* 349:1255555.
9. Jucker M & Walker LC (2013) Self-propagation of pathogenic protein aggregates in neurodegenerative diseases. *Nature* 501:45-51.
10. Pace CN (1986) Determination and analysis of urea and guanidine hydrochloride denaturation curves. *Methods Enzymol* 131:266-280.
11. Shortle D (1996) The denatured state (the other half of the folding equation) and its role in protein stability. *Faseb J* 10:27-34.
12. Tanford C, Pain RH, & Otchin NS (1966) Equilibrium and kinetics of the unfolding of lysozyme (muramidase) by guanidine hydrochloride. *J Mol Biol* 15:489-504.
13. Bieri O, Wirz J, Hellrung B, Schutkowski M, Drewello M, & Kiefhaber T (1999) The speed limit for protein folding measured by triplet-triplet energy transfer. *Proc Natl Acad Sci U S A* 96:9597-9601.
14. Krieger F, Fierz B, Bieri O, Drewello M, & Kiefhaber T (2003) Dynamics of unfolded polypeptide chains as model for the earliest steps in protein folding. *J Mol Biol* 332:265-274.
15. Tanford C (1968) Protein denaturation. *Adv Protein Chem* 23:121-282.

16. Flory PJ (1969) Statistical mechanics of chain molecules. *Hanser Publishers, Munich*.
17. Tanford C (1970) Protein denaturation. C. Theoretical models for the mechanism of denaturation. *Adv Protein Chem* 24:1-95.
18. Fierz B & Kiefhaber T (2005) Dynamics of unfolded polypeptide chains. Protein Folding Handbook (Buchner, J. and Kiefhaber, T. eds.). *Wiley-VCH, Weinheim* 1:809-855.
19. Fleming PJ & Rose GD (2005) Conformational properties of unfolded proteins. Protein Folding Handbook (Buchner, J. and Kiefhaber, T. eds.). *Wiley-VCH, Weinheim* 1:710-736.
20. Levinthal C (1968) Are There Pathways for Protein Folding. *J Chim Phys Pcb* 65:44-+.
21. Ramachandran GN & Sasisekharan V (1968) Conformation of polypeptides and proteins. *Adv Protein Chem* 23:283-438.
22. Ramachandran GN, Ramakrishnan C, & Sasisekharan V (1963) Stereochemistry of polypeptide chain configurations. *J Mol Biol* 7:95-99.
23. Pappu RV, Srinivasan R, & Rose GD (2000) The Flory isolated-pair hypothesis is not valid for polypeptide chains: Implications for protein folding. *Proc Natl Acad Sci U S A* 97:12565-12570.
24. Porter LL & Rose GD (2011) Redrawing the Ramachandran plot after inclusion of hydrogen-bonding constraints. *Proc Natl Acad Sci U S A* 108:109-113.
25. Evans PA, Topping KD, Woolfson DN, & Dobson CM (1991) Hydrophobic clustering in nonnative states of a protein: interpretation of chemical shifts in NMR spectra of denatured states of lysozyme. *Proteins* 9:248-266.
26. Neri D, Billeter M, Wider G, & Wuthrich K (1992) NMR determination of residual structure in a urea-denatured protein, the 434-repressor. *Science* 257:1559-1563.
27. Yi Q, Scalley-Kim ML, Alm EJ, & Baker D (2000) NMR characterization of residual structure in the denatured state of protein L. *J Mol Biol* 299:1341-1351.
28. Dyson HJ & Wright PE (2002) Insights into the structure and dynamics of unfolded proteins from nuclear magnetic resonance. *Adv Protein Chem* 62:311-340.

29. Sanchez IE & Kiefhaber T (2003) Hammond behavior versus ground state effects in protein folding: evidence for narrow free energy barriers and residual structure in unfolded states. *J Mol Biol* 327:867-884.
30. Holzwarth G & Doty P (1965) The Ultraviolet Circular Dichroism of Polypeptides. *J Am Chem Soc* 87:218-228.
31. Tiffany ML & Krimm S (1968) New chain conformations of poly(glutamic acid) and polylysine. *Biopolymers* 6:1379-1382.
32. Smyth E, Syme CD, Blanch EW, Hecht L, Vasak M, & Barron LD (2001) Solution structure of native proteins with irregular folds from Raman optical activity. *Biopolymers* 58:138-151.
33. Pappu RV & Rose GD (2002) A simple model for polyproline II structure in unfolded states of alanine-based peptides. *Protein Sci* 11:2437-2455.
34. Shi Z, Olson CA, Rose GD, Baldwin RL, & Kallenbach NR (2002) Polyproline II structure in a sequence of seven alanine residues. *Proc Natl Acad Sci U S A* 99:9190-9195.
35. Shi Z, Woody RW, & Kallenbach NR (2002) Is polyproline II a major backbone conformation in unfolded proteins? *Adv Protein Chem* 62:163-240.
36. Zwanzig R, Szabo A, & Bagchi B (1992) Levinthal's paradox. *Proc Natl Acad Sci U S A* 89:20-22.
37. Wright PE & Dyson HJ (1999) Intrinsically unstructured proteins: re-assessing the protein structure-function paradigm. *J Mol Biol* 293:321-331.
38. Uversky VN, Gillespie JR, & Fink AL (2000) Why are "natively unfolded" proteins unstructured under physiologic conditions? *Proteins* 41:415-427.
39. Dunker AK, Lawson JD, Brown CJ, Williams RM, Romero P, Oh JS, Oldfield CJ, Campen AM, Ratliff CM, Hipps KW, Ausio J, Nissen MS, Reeves R, Kang C, Kissinger CR, Bailey RW, Griswold MD, Chiu W, Garner EC, & Obradovic Z (2001) Intrinsically disordered protein. *J Mol Graph Model* 19:26-59.
40. Dyson HJ & Wright PE (2005) Intrinsically unstructured proteins and their functions. *Nat Rev Mol Cell Biol* 6:197-208.
41. Yankeelov JA, Jr. & Koshland DE, Jr. (1965) Evidence for Conformation Changes Induced by Substrates of Phosphoglucomutase. *J Biol Chem* 240:1593-1602.

42. Zettlmeissl G, Teschner W, Rudolph R, Jaenicke R, & Gade G (1984) Isolation, physicochemical properties, and folding of octopine dehydrogenase from *Pecten jacobaeus*. *Eur J Biochem* 143:401-407.
43. Kiefhaber T, Quaas R, Hahn U, & Schmid FX (1990) Folding of ribonuclease T1. 2. Kinetic models for the folding and unfolding reactions. *Biochemistry* 29:3061-3070.
44. Frauenfelder H, Sligar SG, & Wolynes PG (1991) The energy landscapes and motions of proteins. *Science* 254:1598-1603.
45. Modig K, Liepinsh E, Otting G, & Halle B (2004) Dynamics of protein and peptide hydration. *J Am Chem Soc* 126:102-114.
46. Bierzynski A, Kim PS, & Baldwin RL (1982) A salt bridge stabilizes the helix formed by isolated C-peptide of RNase A. *Proc Natl Acad Sci U S A* 79:2470-2474.
47. Pauling L, Corey RB, & Branson HR (1951) The structure of proteins; two hydrogen-bonded helical configurations of the polypeptide chain. *Proc Natl Acad Sci U S A* 37:205-211.
48. Pauling L & Corey RB (1951) The pleated sheet, a new layer configuration of polypeptide chains. *Proc Natl Acad Sci U S A* 37:251-256.
49. Kauzmann W (1959) Some factors in the interpretation of protein denaturation. *Adv Protein Chem* 14:1-63.
50. Anderson DE, Becktel WJ, & Dahlquist FW (1990) pH-induced denaturation of proteins: a single salt bridge contributes 3-5 kcal/mol to the free energy of folding of T4 lysozyme. *Biochemistry* 29:2403-2408.
51. Baldwin RL (2007) Energetics of protein folding. *J Mol Biol* 371:283-301.
52. Baldwin RL & Rose GD (2016) How the hydrophobic factor drives protein folding. *Proc Natl Acad Sci U S A* 113:12462-12466.
53. Ekman D, Bjorklund AK, Frey-Skott J, & Elofsson A (2005) Multi-domain proteins in the three kingdoms of life: orphan domains and other unassigned regions. *J Mol Biol* 348:231-243.
54. Privalov PL (1979) Stability of proteins: small globular proteins. *Adv Protein Chem* 33:167-241.
55. Creighton TE (1988) Toward a better understanding of protein folding pathways. *Proc Natl Acad Sci U S A* 85:5082-5086.

56. Zwanzig R (1997) Two-state models of protein folding kinetics. *Proc Natl Acad Sci U S A* 94:148-150.
57. Jackson SE (1998) How do small single-domain proteins fold? *Fold Des* 3:R81-91.
58. Privalov PL & Makhatadze GI (1992) Contribution of hydration and non-covalent interactions to the heat capacity effect on protein unfolding. *J Mol Biol* 224:715-723.
59. Nozaki Y & Tanford C (1963) The Solubility of Amino Acids and Related Compounds in Aqueous Urea Solutions. *J Biol Chem* 238:4074-4081.
60. Tanford C (1964) Isothermal unfolding of globular proteins in aqueous urea solutions. *J Am Chem Soc* 86:2050-2059.
61. Aune KC & Tanford C (1969) Thermodynamics of the denaturation of lysozyme by guanidine hydrochloride. II. Dependence on denaturant concentration at 25 degrees. *Biochemistry* 8:4586-4590.
62. Schellman JA (1987) Selective binding and solvent denaturation. *Biopolymers* 26:549-559.
63. Auton M & Bolen DW (2005) Predicting the energetics of osmolyte-induced protein folding/unfolding. *Proc Natl Acad Sci U S A* 102:15065-15068.
64. Moglich A, Krieger F, & Kiefhaber T (2005) Molecular basis for the effect of urea and guanidinium chloride on the dynamics of unfolded polypeptide chains. *J Mol Biol* 345:153-162.
65. Gekko K & Timasheff SN (1981) Mechanism of protein stabilization by glycerol: preferential hydration in glycerol-water mixtures. *Biochemistry* 20:4667-4676.
66. Timasheff SN (2002) Protein-solvent preferential interactions, protein hydration, and the modulation of biochemical reactions by solvent components. *Proc Natl Acad Sci U S A* 99:9721-9726.
67. Greene RF, Jr. & Pace CN (1974) Urea and guanidine hydrochloride denaturation of ribonuclease, lysozyme, alpha-chymotrypsin, and beta-lactoglobulin. *J Biol Chem* 249:5388-5393.
68. Santoro MM & Bolen DW (1988) Unfolding free energy changes determined by the linear extrapolation method. 1. Unfolding of phenylmethanesulfonyl alpha-chymotrypsin using different denaturants. *Biochemistry* 27:8063-8068.

69. Myers JK, Pace CN, & Scholtz JM (1995) Denaturant m values and heat capacity changes: relation to changes in accessible surface areas of protein unfolding. *Protein Sci* 4:2138-2148.
70. Kiefhaber T, Sanchez IE, & Bachmann A (2005) Characterization of protein folding barriers with rate equilibrium free energy relationships. Protein Folding Handbook (Buchner, J. and Kiefhaber, T. eds.). *Wiley-VCH, Weinheim* 1:411-444.
71. Sanchez IE & Kiefhaber T (2003) Evidence for sequential barriers and obligatory intermediates in apparent two-state protein folding. *J Mol Biol* 325:367-376.
72. Bachmann A & Kiefhaber T (2001) Apparent two-state tendamistat folding is a sequential process along a defined route. *J Mol Biol* 306:375-386.
73. Wagner C & Kiefhaber T (1999) Intermediates can accelerate protein folding. *Proc Natl Acad Sci U S A* 96:6716-6721.
74. Jaenicke R (1987) Folding and association of proteins. *Prog Biophys Mol Biol* 49:117-237.
75. Kubelka J, Chiu TK, Davies DR, Eaton WA, & Hofrichter J (2006) Sub-microsecond protein folding. *J Mol Biol* 359:546-553.
76. Dyer RB (2007) Ultrafast and downhill protein folding. *Curr Opin Struct Biol* 17:38-47.
77. Jaenicke R (1999) Stability and folding of domain proteins. *Prog Biophys Mol Biol* 71:155-241.
78. Fierz B & Kiefhaber T (2007) End-to-end vs interior loop formation kinetics in unfolded polypeptide chains. *J Am Chem Soc* 129:672-679.
79. Fierz B, Satzger H, Root C, Gilch P, Zinth W, & Kiefhaber T (2007) Loop formation in unfolded polypeptide chains on the picoseconds to microseconds time scale. *Proc Natl Acad Sci U S A* 104:2163-2168.
80. Garel JR & Baldwin RL (1973) Both the fast and slow refolding reactions of ribonuclease A yield native enzyme. *Proc Natl Acad Sci U S A* 70:3347-3351.
81. Creighton TE (1997) Protein folding coupled to disulphide bond formation. *Biol Chem* 378:731-744.
82. Bachmann A & Kiefhaber T (2005) Kinetic mechanisms in protein folding. Protein Folding Handbook (Buchner, J. and Kiefhaber, T. eds.). *Wiley-VCH, Weinheim* 1:379-410.

83. Evans MG & Polanyi M (1935) Some applications of the transition state method to the calculation of reaction velocities, especially in solution. *Trans Faraday Soc* 31:875-894.
84. Eyring H (1935) The activated complex in chemical reactions. *J Chem Phys* 3:107-115.
85. Krieger F, Moglich A, & Kiefhaber T (2005) Effect of proline and glycine residues on dynamics and barriers of loop formation in polypeptide chains. *J Am Chem Soc* 127:3346-3352.
86. Smoluchowski M (1917) Versuch einer mathematischen Theorie der Koagulationskinetik kolloider Lösungen. *Z Fur Phys Chem* 92:129-168.
87. Leffler JE (1953) Parameters for the Description of Transition States. *Science* 117:340-341.
88. Vendruscolo M, Paci E, Dobson CM, & Karplus M (2001) Three key residues form a critical contact network in a protein folding transition state. *Nature* 409:641-645.
89. Sanchez IE & Kiefhaber T (2003) Origin of unusual phi-values in protein folding: evidence against specific nucleation sites. *J Mol Biol* 334:1077-1085.
90. Wetlaufer DB (1973) Nucleation, rapid folding, and globular intrachain regions in proteins. *Proc Natl Acad Sci U S A* 70:697-701.
91. Kim PS & Baldwin RL (1982) Specific intermediates in the folding reactions of small proteins and the mechanism of protein folding. *Annu Rev Biochem* 51:459-489.
92. Schmid FX & Baldwin RL (1979) Detection of an early intermediate in the folding of ribonuclease A by protection of amide protons against exchange. *J Mol Biol* 135:199-215.
93. Karplus M & Weaver DL (1976) Protein-folding dynamics. *Nature* 260:404-406.
94. Karplus M & Weaver DL (1994) Protein folding dynamics: the diffusion-collision model and experimental data. *Protein Sci* 3:650-668.
95. Tanford C (1962) Contribution of Hydrophobic Interactions to Stability of Globular Conformation of Proteins. *J Am Chem Soc* 84:4240-&.
96. Baldwin RL (1989) How does protein folding get started? *Trends Biochem Sci* 14:291-294.

97. Fersht AR (1995) Optimization of rates of protein folding: the nucleation-condensation mechanism and its implications. *Proc Natl Acad Sci U S A* 92:10869-10873.
98. Fersht AR (1997) Nucleation mechanisms in protein folding. *Curr Opin Struct Biol* 7:3-9.
99. Dill KA, Ozkan SB, Shell MS, & Weikl TR (2008) The protein folding problem. *Annu Rev Biophys* 37:289-316.
100. Jacob M, Schindler T, Balbach J, & Schmid FX (1997) Diffusion control in an elementary protein folding reaction. *Proc Natl Acad Sci U S A* 94:5622-5627.
101. Jacob M, Geeves M, Holtermann G, & Schmid FX (1999) Diffusional barrier crossing in a two-state protein folding reaction. *Nat Struct Biol* 6:923-926.
102. Jacob M & Schmid FX (1999) Protein folding as a diffusional process. *Biochemistry* 38:13773-13779.
103. Kramers HA (1940) Brownian motion in a field of force and the diffusion model of chemical reactions. *Physica* 7:284-304.
104. Plaxco KW & Baker D (1998) Limited internal friction in the rate-limiting step of a two-state protein folding reaction. *Proc Natl Acad Sci U S A* 95:13591-13596.
105. Ramos CH, Weisbuch S, & Jamin M (2007) Diffusive motions control the folding and unfolding kinetics of the apomyoglobin pH 4 molten globule intermediate. *Biochemistry* 46:4379-4389.
106. Beece D, Eisenstein L, Frauenfelder H, Good D, Marden MC, Reinisch L, Reynolds AH, Sorensen LB, & Yue KT (1980) Solvent viscosity and protein dynamics. *Biochemistry* 19:5147-5157.
107. Yedgar S, Tetreau C, Gavish B, & Lavalette D (1995) Viscosity dependence of O₂ escape from respiratory proteins as a function of cosolvent molecular weight. *Biophys J* 68:665-670.
108. Kleinert T, Doster W, Leyser H, Petry W, Schwarz V, & Settles M (1998) Solvent composition and viscosity effects on the kinetics of CO binding to horse myoglobin. *Biochemistry* 37:717-733.
109. Jas GS, Eaton WA, & Hofrichter J (2001) Effect of viscosity on the kinetics of alpha-helix and beta-hairpin formation. *J Phys Chem B* 105:261-272.
110. Grote RF & Hynes JT (1980) The stable states picture of chemical reactions. II. rate constants for condensed and gas phase reaction models. *J Chem Phys* 73:2715-2732.

111. de Sancho D, Sirur A, & Best RB (2014) Molecular origins of internal friction effects on protein-folding rates. *Nat Commun* 5:4307.
112. Ansari A, Jones CM, Henry ER, Hofrichter J, & Eaton WA (1992) The role of solvent viscosity in the dynamics of protein conformational changes. *Science* 256:1796-1798.
113. Schulz JC, Schmidt L, Best RB, Dzubiella J, & Netz RR (2012) Peptide chain dynamics in light and heavy water: zooming in on internal friction. *J Am Chem Soc* 134:6273-6279.
114. Zheng W, de Sancho D, & Best RB (2016) Modulation of Folding Internal Friction by Local and Global Barrier Heights. *J Phys Chem Lett* 7:1028-1034.
115. Velsko SP & Fleming GR (1982) Solvent Influence on Photochemical Isomerizations - Photophysics of Dodci. *Chem Phys* 65:59-70.
116. Velsko SP & Fleming GR (1982) Photochemical Isomerization in Solution - Photophysics of Diphenyl Butadiene. *J Chem Phys* 76:3553-3562.
117. Velsko SP, Waldeck DH, & Fleming GR (1983) Breakdown of Kramer Theory Description of Photochemical Isomerization and the Possible Involvement of Frequency-Dependent Friction. *J Chem Phys* 78:249-258.
118. Bagchi B & Oxtoby DW (1983) The Effect of Frequency-Dependent Friction on Isomerization Dynamics in Solution. *J Chem Phys* 78:2735-2741.
119. Kuhn W & Kuhn H (1945) Die Abhängigkeit der Viskosität vom Strömungsgefälle bei hochverdünnten Suspensionen und Lösungen. *Helv Chim Acta* 28:97-127.
120. Kuhn W & Kuhn H (1946) Bedeutung beschränkt freier Drehbarkeit für die Viskosität und Strömungsdoppelberechnung von Fadenmolekülelösungen II. *Helv Chim Acta* 29:71-94.
121. Cerf R (1958) Mecanique Statistique Des Macromolecules En Chaines Dans Un Champ De Vitesses. *J Phys-Paris* 19:122-134.
122. Peterlin J (1972) Origin of internal viscosity in linear macromolecules. *J Polym Sc* 10:101-105.
123. Gennes PG (1977) Origin of internal viscosities in dilute polymer solutions. *J Chem Phys* 66:5825-5826.
124. Pabit SA, Roder H, & Hagen SJ (2004) Internal friction controls the speed of protein folding from a compact configuration. *Biochemistry* 43:12532-12538.

125. Qiu L & Hagen SJ (2004) A limiting speed for protein folding at low solvent viscosity. *J Am Chem Soc* 126:3398-3399.
126. Cellmer T, Henry ER, Hofrichter J, & Eaton WA (2008) Measuring internal friction of an ultrafast-folding protein. *Proc Natl Acad Sci U S A* 105:18320-18325.
127. Wensley BG, Batey S, Bone FA, Chan ZM, Tumelty NR, Steward A, Kwa LG, Borgia A, & Clarke J (2010) Experimental evidence for a frustrated energy landscape in a three-helix-bundle protein family. *Nature* 463:685-688.
128. Borgia A, Wensley BG, Soranno A, Nettels D, Borgia MB, Hoffmann A, Pfeil SH, Lipman EA, Clarke J, & Schuler B (2012) Localizing internal friction along the reaction coordinate of protein folding by combining ensemble and single-molecule fluorescence spectroscopy. *Nat Commun* 3:1195.
129. Soranno A, Buchli B, Nettels D, Cheng RR, Muller-Spath S, Pfeil SH, Hoffmann A, Lipman EA, Makarov DE, & Schuler B (2012) Quantifying internal friction in unfolded and intrinsically disordered proteins with single-molecule spectroscopy. *Proc Natl Acad Sci U S A* 109:17800-17806.
130. Chung HS & Eaton WA (2013) Single-molecule fluorescence probes dynamics of barrier crossing. *Nature* 502:685-688.
131. Kabsch W & Sander C (1983) Dictionary of protein secondary structure: pattern recognition of hydrogen-bonded and geometrical features. *Biopolymers* 22:2577-2637.
132. Barlow DJ & Thornton JM (1988) Helix geometry in proteins. *J Mol Biol* 201:601-619.
133. Kendrew JC, Dickerson RE, Strandberg BE, Hart RG, Davies DR, Phillips DC, & Shore VC (1960) Structure of myoglobin: A three-dimensional Fourier synthesis at 2 Å resolution. *Nature* 185:422-427.
134. Schellman JA (1955) The stability of hydrogen-bonded peptide structures in aqueous solution. *C R Trav Lab Carlsberg Chim* 29:230-259.
135. Brown JE & Klee WA (1971) Helix-coil transition of the isolated amino terminus of ribonuclease. *Biochemistry* 10:470-476.
136. Kim PS & Baldwin RL (1984) A helix stop signal in the isolated S-peptide of ribonuclease A. *Nature* 307:329-334.

137. Shoemaker KR, Fairman R, Kim PS, York EJ, Stewart JM, & Baldwin RL (1987) The C-peptide helix from ribonuclease A considered as an autonomous folding unit. *Cold Spring Harb Symp Quant Biol* 52:391-398.
138. Jennings PA & Wright PE (1993) Formation of a molten globule intermediate early in the kinetic folding pathway of apomyoglobin. *Science* 262:892-896.
139. Raschke TM & Marqusee S (1997) The kinetic folding intermediate of ribonuclease H resembles the acid molten globule and partially unfolded molecules detected under native conditions. *Nat Struct Biol* 4:298-304.
140. Doig A, Errington N, & Iqbalsyah T (2005) Stability and design of alpha-helices. Protein Folding Handbook (Buchner, J. and Kiefhaber, T. eds.). *Wiley-VCH, Weinheim* 1:247-313.
141. Epanand RM & Scheraga HA (1968) The influence of long-range interactions on the structure of myoglobin. *Biochemistry* 7:2864-2872.
142. Taniuchi H & Anfinsen CB (1969) An experimental approach to the study of the folding of staphylococcal nuclease. *J Biol Chem* 244:3864-3875.
143. Shoemaker KR, Kim PS, Brems DN, Marqusee S, York EJ, Chaiken IM, Stewart JM, & Baldwin RL (1985) Nature of the charged-group effect on the stability of the C-peptide helix. *Proc Natl Acad Sci U S A* 82:2349-2353.
144. Shoemaker KR, Kim PS, York EJ, Stewart JM, & Baldwin RL (1987) Tests of the helix dipole model for stabilization of alpha-helices. *Nature* 326:563-567.
145. Fairman R, Shoemaker KR, York EJ, Stewart JM, & Baldwin RL (1990) The Glu 2- ... Arg 10+ side-chain interaction in the C-peptide helix of ribonuclease A. *Biophys Chem* 37:107-119.
146. Shoemaker KR, Fairman R, Schultz DA, Robertson AD, York EJ, Stewart JM, & Baldwin RL (1990) Side-chain interactions in the C-peptide helix: Phe 8 ... His 12+. *Biopolymers* 29:1-11.
147. Marqusee S, Robbins VH, & Baldwin RL (1989) Unusually stable helix formation in short alanine-based peptides. *Proc Natl Acad Sci U S A* 86:5286-5290.
148. Armstrong KM, Fairman R, & Baldwin RL (1993) The (i, i + 4) Phe-His interaction studied in an alanine-based alpha-helix. *J Mol Biol* 230:284-291.
149. Padmanabhan S & Baldwin RL (1994) Tests for helix-stabilizing interactions between various nonpolar side chains in alanine-based peptides. *Protein Sci* 3:1992-1997.

150. Padmanabhan S & Baldwin RL (1994) Helix-stabilizing interaction between tyrosine and leucine or valine when the spacing is $i, i + 4$. *J Mol Biol* 241:706-713.
151. Huyghues-Despointes BM, Klingler TM, & Baldwin RL (1995) Measuring the strength of side-chain hydrogen bonds in peptide helices: the Gln.Asp ($i, i + 4$) interaction. *Biochemistry* 34:13267-13271.
152. Huyghues-Despointes BM & Baldwin RL (1997) Ion-pair and charged hydrogen-bond interactions between histidine and aspartate in a peptide helix. *Biochemistry* 36:1965-1970.
153. Stapley BJ & Doig AJ (1997) Hydrogen bonding interactions between glutamine and asparagine in alpha-helical peptides. *J Mol Biol* 272:465-473.
154. Andrew CD, Penel S, Jones GR, & Doig AJ (2001) Stabilizing nonpolar/polar side-chain interactions in the alpha-helix. *Proteins* 45:449-455.
155. Shi Z, Olson CA, Bell AJ, Jr., & Kallenbach NR (2001) Stabilization of alpha-helix structure by polar side-chain interactions: complex salt bridges, cation-pi interactions, and C-H...O H-bonds. *Biopolymers* 60:366-380.
156. Andrew CD, Bhattacharjee S, Kokkoni N, Hirst JD, Jones GR, & Doig AJ (2002) Stabilizing interactions between aromatic and basic side chains in alpha-helical peptides and proteins. Tyrosine effects on helix circular dichroism. *J Am Chem Soc* 124:12706-12714.
157. Tsou LK, Tatko CD, & Waters ML (2002) Simple cation-pi interaction between a phenyl ring and a protonated amine stabilizes an alpha-helix in water. *J Am Chem Soc* 124:14917-14921.
158. Errington N, Iqbalsyah T, & Doig A (2006) Structure and stability of the alpha-helix: lessons for design. *Methods Mol Biol* 340:3-26.
159. Andrew CD, Warwicker J, Jones GR, & Doig AJ (2002) Effect of phosphorylation on alpha-helix stability as a function of position. *Biochemistry* 41:1897-1905.
160. Scholtz JM, Marqusee S, Baldwin RL, York EJ, Stewart JM, Santoro M, & Bolen DW (1991) Calorimetric determination of the enthalpy change for the alpha-helix to coil transition of an alanine peptide in water. *Proc Natl Acad Sci U S A* 88:2854-2858.
161. Lopez MM, Chin DH, Baldwin RL, & Makhatadze GI (2002) The enthalpy of the alanine peptide helix measured by isothermal titration calorimetry using metal-binding to induce helix formation. *Proc Natl Acad Sci U S A* 99:1298-1302.

162. Rohl CA, Chakrabartty A, & Baldwin RL (1996) Helix propagation and N-cap propensities of the amino acids measured in alanine-based peptides in 40 volume percent trifluoroethanol. *Protein Sci* 5:2623-2637.
163. Argos P & Palau J (1982) Amino acid distribution in protein secondary structures. *Int J Pept Protein Res* 19:380-393.
164. Presta LG & Rose GD (1988) Helix signals in proteins. *Science* 240:1632-1641.
165. Richardson JS & Richardson DC (1988) Amino acid preferences for specific locations at the ends of alpha helices. *Science* 240:1648-1652.
166. Forood B, Feliciano EJ, & Nambiar KP (1993) Stabilization of alpha-helical structures in short peptides via end capping. *Proc Natl Acad Sci U S A* 90:838-842.
167. Aurora R & Rose GD (1998) Helix capping. *Protein Sci* 7:21-38.
168. Chakrabartty A, Schellman JA, & Baldwin RL (1991) Large differences in the helix propensities of alanine and glycine. *Nature* 351:586-588.
169. Rohl CA & Baldwin RL (1994) Exchange kinetics of individual amide protons in ¹⁵N-labeled helical peptides measured by isotope-edited NMR. *Biochemistry* 33:7760-7767.
170. Fierz B, Reiner A, & Kiefhaber T (2009) Local conformational dynamics in alpha-helices measured by fast triplet transfer. *Proc Natl Acad Sci U S A* 106:1057-1062.
171. Liff MI, Lyu PC, & Kallenbach NR (1991) Analysis of asymmetry in the distribution of helical residues in peptides by ¹H nuclear magnetic resonance. *J Am Chem Soc* 113:1014-1019.
172. Wada A (1976) The alpha-helix as an electric macro-dipole. *Adv Biophys*:1-63.
173. Huyghues-Despointes BM, Scholtz JM, & Baldwin RL (1993) Effect of a single aspartate on helix stability at different positions in a neutral alanine-based peptide. *Protein Sci* 2:1604-1611.
174. Hol WG, van Duijnen PT, & Berendsen HJ (1978) The alpha-helix dipole and the properties of proteins. *Nature* 273:443-446.
175. Sali D, Bycroft M, & Fersht AR (1988) Stabilization of protein structure by interaction of alpha-helix dipole with a charged side chain. *Nature* 335:740-743.
176. Doig AJ & Baldwin RL (1995) N- and C-capping preferences for all 20 amino acids in alpha-helical peptides. *Protein Sci* 4:1325-1336.
177. Chakrabartty A, Doig AJ, & Baldwin RL (1993) Helix capping propensities in peptides parallel those in proteins. *Proc Natl Acad Sci U S A* 90:11332-11336.

178. Doig AJ, Chakrabartty A, Klingler TM, & Baldwin RL (1994) Determination of free energies of N-capping in alpha-helices by modification of the Lifson-Roig helix-coil theory to include N- and C-capping. *Biochemistry* 33:3396-3403.
179. Doig AJ, MacArthur MW, Stapley BJ, & Thornton JM (1997) Structures of N-termini of helices in proteins. *Protein Sci* 6:147-155.
180. Prieto J & Serrano L (1997) C-capping and helix stability: the Pro C-capping motif. *J Mol Biol* 274:276-288.
181. Nicholson H, Anderson DE, Dao-pin S, & Matthews BW (1991) Analysis of the interaction between charged side chains and the alpha-helix dipole using designed thermostable mutants of phage T4 lysozyme. *Biochemistry* 30:9816-9828.
182. Penel S, Hughes E, & Doig AJ (1999) Side-chain structures in the first turn of the alpha-helix. *J Mol Biol* 287:127-143.
183. Cochran DA & Doig AJ (2001) Effect of the N2 residue on the stability of the alpha-helix for all 20 amino acids. *Protein Sci* 10:1305-1311.
184. Cochran DA, Penel S, & Doig AJ (2001) Effect of the N1 residue on the stability of the alpha-helix for all 20 amino acids. *Protein Sci* 10:463-470.
185. Miranda JJ (2003) Position-dependent interactions between cysteine residues and the helix dipole. *Protein Sci* 12:73-81.
186. Neumaier S, Reiner A, Buttner M, Fierz B, & Kiefhaber T (2013) Testing the diffusing boundary model for the helix-coil transition in peptides. *Proc Natl Acad Sci U S A* 110:12905-12910.
187. Zimm BH & Bragg JK (1959) Theory of the phase transition between helix and random coil in polypeptide chains. *J Chem Phys* 31:526-535.
188. Lifson S & Roig A (1961) On the theory of helix-coil transition in polypeptides. *J Chem Phys* 34:1963-1974.
189. Qian H & Schellman JA (1992) Helix-Coil Theories: A comparative study for finite length polypeptides. *J Phys Chem* 96:3987-3994.
190. Ising E (1925) Beitrag zur Theorie des Ferromagnetismus. *Z Fur Phys* 31:253-258.
191. Scholtz JM, Qian H, Robbins VH, & Baldwin RL (1993) The energetics of ion-pair and hydrogen-bonding interactions in a helical peptide. *Biochemistry* 32:9668-9676.

192. Sun JK, Penel S, & Doig AJ (2000) Determination of alpha-helix N1 energies after addition of N1, N2, and N3 preferences to helix/coil theory. *Protein Sci* 9:750-754.
193. Chakrabarty A, Kortemme T, Padmanabhan S, & Baldwin RL (1993) Aromatic side-chain contribution to far-ultraviolet circular dichroism of helical peptides and its effect on measurement of helix propensities. *Biochemistry* 32:5560-5565.
194. Schwarz G (1965) On the Kinetics of the Helix-Coil Transition of Polypeptides in Solution. *J Mol Biol* 11:64-77.
195. Schwarz G & Seelig J (1968) Kinetic properties and the electric field effect of the helix-coil transition of poly(gamma-benzyl L-glutamate) determined from dielectric relaxation measurements. *Biopolymers* 6:1263-1277.
196. Gruenewald B, Nicola CU, Lustig A, Schwarz G, & Klump H (1979) Kinetics of the helix-coil transition of a polypeptide with non-ionic side groups, derived from ultrasonic relaxation measurements. *Biophys Chem* 9:137-147.
197. Williams S, Causgrove TP, Gilmanshin R, Fang KS, Callender RH, Woodruff WH, & Dyer RB (1996) Fast events in protein folding: helix melting and formation in a small peptide. *Biochemistry* 35:691-697.
198. Thompson PA, Eaton WA, & Hofrichter J (1997) Laser temperature jump study of the helix \rightleftharpoons coil kinetics of an alanine peptide interpreted with a 'kinetic zipper' model. *Biochemistry* 36:9200-9210.
199. Lednev IK, Karnoup AS, Sparrow MC, & Asher SA (1999) alpha-helix peptide folding and unfolding activation barriers: A nanosecond UV resonance raman study. *J Am Chem Soc* 121:8074-8086.
200. Thompson PA, Munoz V, Jas GS, Henry ER, Eaton WA, & Hofrichter J (2000) The helix-coil kinetics of a heteropeptide. *J Phys Chem B* 104:378-389.
201. Huang CY, Getahun Z, Wang T, DeGrado WF, & Gai F (2001) Time-resolved infrared study of the helix-coil transition using ^{13}C -labeled helical peptides. *J Am Chem Soc* 123:12111-12112.
202. Huang CY, Klemke JW, Getahun Z, DeGrado WF, & Gai F (2001) Temperature-dependent helix-coil transition of an alanine based peptide. *J Am Chem Soc* 123:9235-9238.
203. Huang CY, Getahun Z, Zhu Y, Klemke JW, DeGrado WF, & Gai F (2002) Helix formation via conformation diffusion search. *Proc Natl Acad Sci U S A* 99:2788-2793.

204. Dexter DL (1953) A Theory of Sensitized Luminescence in Solids. *J Chem Phys* 21:836-850.
205. Forster T (1948) *Zwischenmolekulare Energiewanderung Und Fluoreszenz. *Ann Phys-Berlin* 2:55-75.
206. Satzger H, Schmidt B, Root C, Zinth W, Fierz B, Krieger F, Kiefhaber T, & Gilch P (2004) Ultrafast quenching of the xanthone triplet by energy transfer: New insight into the intersystem crossing kinetics. *J Phys Chem A* 108:10072-10079.
207. Heinz B, Schmidt B, Root C, Satzger H, Milota F, Fierz B, Kiefhaber T, Zinth W, & Gilch P (2006) On the unusual fluorescence properties of xanthone in water. *Phys Chem Chem Phys* 8:3432-3439.
208. Moglich A, Joder K, & Kiefhaber T (2006) End-to-end distance distributions and intrachain diffusion constants in unfolded polypeptide chains indicate intramolecular hydrogen bond formation. *Proc Natl Acad Sci U S A* 103:12394-12399.
209. Szabo A, Schulten K, & Schulten Z (1980) First passage time approach to diffusion controlled reactions. *J Chem Phys* 72:4350-4357.
210. Krieger F, Fierz B, Axthelm F, Joder K, Meyer D, & Kiefhaber T (2004) Intrachain diffusion in a protein loop fragment from carp parvalbumin. *Chem Phys* 307:209-215.
211. Krieger F (2004) Dynamics in unfolded polypeptide chains as model for elementary steps in protein folding. *PhD thesis, Universität Basel*.
212. Joder K (2011) Intramolecular and intermolecular diffusion processes in protein folding and assembly. *PhD thesis, Technische Universität München*.
213. Reiner A, Henklein P, & Kiefhaber T (2010) An unlocking/relocking barrier in conformational fluctuations of villin headpiece subdomain. *Proc Natl Acad Sci U S A* 107:4955-4960.
214. Einstein A (1905) Über die von der molekularkinetischen Theorie der Wärme geforderte Bewegung von in ruhenden Flüssigkeiten suspendierten Teilchen. *Ann d Phys* 322:549-560.
215. Smoluchowski M (1906) Zur kinetischen Theorie der Brownschen Molekularbewegung und der Suspension. *Ann d Phys* 326:756-780.
216. Stokes GG (1851) On the effect of internal friction of fluids on the motion of pendulums. *Trans Camb Philos Soc* 9:8-106.

217. Scholtz JM & Baldwin RL (1992) The mechanism of alpha-helix formation by peptides. *Annu Rev Biophys Biomol Struct* 21:95-118.
218. Graham R & Lewis JR (1978) Synthesis of 9-Oxoxanthen-2-Carboxylic Acids. *J Chem Soc Perk T 1*:876-881.
219. Kiefhaber T, Kohler HH, & Schmid FX (1992) Kinetic coupling between protein folding and prolyl isomerization. I. Theoretical models. *J Mol Biol* 224:217-229.
220. Scholtz JM, Barrick D, York EJ, Stewart JM, & Baldwin RL (1995) Urea unfolding of peptide helices as a model for interpreting protein unfolding. *Proc Natl Acad Sci U S A* 92:185-189.
221. Adler AJ, Hoving R, Potter J, Wells M, & Fasman GD (1968) Circular dichroism of polypeptides. Poly(hydroxyethyl-L-glutamine) compared to poly(L-glutamic acid). *J Am Chem Soc* 90:4736-4738.
222. van Holde KE (1971) Biophysical Chemistry. *Prentice-Hall, London*.
223. Fenimore PW, Frauenfelder H, McMahon BH, & Young RD (2004) Bulk-solvent and hydration-shell fluctuations, similar to alpha- and beta-fluctuations in glasses, control protein motions and functions. *Proc Natl Acad Sci U S A* 101:14408-14413.
224. Neumaier S, Buttner M, Bachmann A, & Kiefhaber T (2013) Transition state and ground state properties of the helix-coil transition in peptides deduced from high-pressure studies. *Proc Natl Acad Sci U S A* 110:20988-20993.
225. Reiner A (2007) Conformational dynamics and stability of structured peptides and small proteins. *PhD thesis, Universität Basel*.
226. Arrhenius SA (1889) Über die Dissociationswärme und den Einfluss der Temperatur auf den Dissociationsgrad der Elektrolyse. *Z Phys Chem* 4:96-116.
227. Bryngelson JD, Onuchic JN, Socci ND, & Wolynes PG (1995) Funnels, pathways, and the energy landscape of protein folding: a synthesis. *Proteins* 21:167-195.
228. Zwanzig R (1988) Diffusion in a rough potential. *Proc Natl Acad Sci U S A* 85:2029-2030.
229. Fersht AR, Shi JP, Knill-Jones J, Lowe DM, Wilkinson AJ, Blow DM, Brick P, Carter P, Waye MM, & Winter G (1985) Hydrogen bonding and biological specificity analysed by protein engineering. *Nature* 314:235-238.
230. Sheu SY, Yang DY, Selzle HL, & Schlag EW (2003) Energetics of hydrogen bonds in peptides. *Proc Natl Acad Sci U S A* 100:12683-12687.

231. Reiner A, Wildemann D, Fischer G, & Kiefhaber T (2008) Effect of thiopeptide bonds on alpha-helix structure and stability. *J Am Chem Soc* 130:8079-8084.
232. Glowinkowski S, Gisser DJ, & Ediger MD (1990) C-13 Nuclear-Magnetic-Resonance Measurements of Local Segmental Dynamics of Polyisoprene in Dilute-Solution - Nonlinear Viscosity Dependence. *Macromolecules* 23:3520-3530.
233. Zhu W & Ediger MD (1995) Deuterium Nmr Characterization of 1,2-Polybutadiene Local Dynamics in Dilute-Solution. *Macromolecules* 28:7549-7557.
234. Zhu W & Ediger MD (1997) Viscosity dependence of polystyrene local dynamics in dilute solution. *Macromolecules* 30:1205-1210.
235. Schiene-Fischer C & Fischer G (2001) Direct measurement indicates a slow cis/trans isomerization at the secondary amide peptide bond of glycylglycine. *J Am Chem Soc* 123:6227-6231.
236. Scheraga HA (1968) Calculations of conformations of polypeptides. *Adv Phys Org Chem* 6:103-184.
237. Mitchell JBO & Price SL (1991) On the Relative Strengths of Amide ... Amide and Amide ... Water Hydrogen-Bonds. *Chem Phys Lett* 180:517-523.
238. Avbelj F, Luo P, & Baldwin RL (2000) Energetics of the interaction between water and the helical peptide group and its role in determining helix propensities. *Proc Natl Acad Sci U S A* 97:10786-10791.
239. Pauling L (1960) The nature of the chemical bond. *Cornell University Press, Ithaca, NY*:468-472.
240. Zinth UG (2014) End-to-end distance distribution and intra-chain diffusion in unfolded polypeptide chains determined by time-resolved FRET measurements. *PhD thesis, Technische Universität München*.
241. Merk ND (2015) Dynamics in folded and unfolded peptides and proteins measured by triplet-triplet energy transfer. *PhD thesis, Technische Universität München*.
242. Zagrovic B, Jayachandran G, Millett IS, Doniach S, & Pande VS (2005) How large is an alpha-helix? Studies of the radii of gyration of helical peptides by small-angle X-ray scattering and molecular dynamics. *J Mol Biol* 353:232-241.

243. Matouschek A, Kellis JT, Jr., Serrano L, & Fersht AR (1989) Mapping the transition state and pathway of protein folding by protein engineering. *Nature* 340:122-126.
244. Northey JG, Maxwell KL, & Davidson AR (2002) Protein folding kinetics beyond the phi value: using multiple amino acid substitutions to investigate the structure of the SH3 domain folding transition state. *J Mol Biol* 320:389-402.
245. Chakrabartty A, Kortemme T, & Baldwin RL (1994) Helix propensities of the amino acids measured in alanine-based peptides without helix-stabilizing side-chain interactions. *Protein Sci* 3:843-852.
246. Fairman R, Shoemaker KR, York EJ, Stewart JM, & Baldwin RL (1989) Further studies of the helix dipole model: effects of a free alpha-NH₃⁺ or alpha-COO- group on helix stability. *Proteins* 5:1-7.
247. Takahashi S, Kim EH, Hibino T, & Ooi T (1989) Comparison of alpha-helix stability in peptides having a negatively or positively charged residue block attached either to the N- or C-terminus of an alpha-helix: the electrostatic contribution and anisotropic stability of the alpha-helix. *Biopolymers* 28:995-1009.

8 Acknowledgement

I would like to thank all the people who were involved in this thesis and supported me during that time. It would not have been possible without your commitment.

In particular, I want to thank Prof. Dr. Thomas Kiefhaber for his supervision, ideas and valuable discussions throughout my thesis. I am also grateful for the well-balanced ratio of guidance and independence he offered me. I really enjoyed working on this versatile project.

Furthermore, I am grateful to PD Dr. Hauke Lilie, who enabled a good start at Halle and supported us while moving from Munich to Halle. In addition, I want to thank him for proofreading my thesis and solving daily problems at the institute.

I am also thankful to Jun.-Prof. Dr. Andreas Reiner for his introduction into MATLAB and motivating discussions about the Lifson-Roig model and helix-coil dynamics.

Many thanks to Dr. Marat Meleshin for introducing me into solid phase peptide synthesis, for your help in designing some of the capping motifs and for sharing some nice discussions in the “Tierstall” at the beginning of my PhD.

Moreover, I want to acknowledge the suggestions and advices by Dr. Thomas Michael inside and outside of the doctoral students seminar.

I am thankful to the whole Department of Biophysical Chemistry at the TUM. In particular, I want to thank Maren Büttner and Sabine Neumaier for their introduction into MC-simulations and the helix project. Moreover, I want to thank Annett Bachmann, Peter Kämmerer, Sabine Kullick, Natalie Merk, Lena Schwarzer, Jeremy Sloan, Karin and Matthias Stecher and Ursula Zinth for the nice time in Munich!

I explicitly want to thank all former and current members of the Department of Protein Biochemistry (Matthias Binder, Peter Enke, Uwe Fandrich, Martin Himmelreich, Malte and Sarah Neudorf, Nadja Reiter, Jakob Ruickoldt, Michael Schleegeer, Frank Ullmann, Martin Voigtmann and Philipp Zimmermann) for the nice atmosphere in the lab, BBQs, coffee breaks, annoying and funny discussions and lunch times at 11.30 am \pm 10 minutes. It was nice working with you even in bad times!

I am also grateful to my family and friends who contributed to this thesis directly or indirectly. Especially I want to thank Opher, Konrad and Helena for proofreading and sharing so many moments in Leipzig.

Finally, I am thankful to my parents for their financial support, their interest in my work and the support in my life.

This thesis is dedicated to the most important persons in my life: Heni and Charlotte!

9 Curriculum Vitae

Personal Data

Name: Stefan Wicht
Address: Aurelienstrasse 35, 04177 Leipzig
Date of birth: 08 August 1985 in Berlin
E-Mail: stefan.wicht@biochemtech.uni-halle.de

Education

- 09/2013 – 09/2018 **PhD in Biochemistry**
Department of Protein Biochemistry – Prof. Dr. T. Kiefhaber
Martin-Luther-Universität Halle-Wittenberg

Thesis: Characterization of the Boundary Diffusion Mechanism for the Helix-Coil Transition in Peptides by Triplet-Triplet Energy Transfer.
- 10/2010 – 11/2012 **Master of Science in Microbiology and Biochemistry**
Georg-August-Universität Göttingen

Master Thesis: Sterical Strain and Conformational Flexibility as a Prerequisite for Driving Catalysis in ThDP-Dependent Enzymes. (AG Tittmann)
- 10/2007 – 09/2010 **Bachelor of Science in Biology**
Georg-August-Universität Göttingen

Bachelor Thesis: The role of YmdB in Biofilm Formation in *Bacillus subtilis*. (AG Stülke)
- 1998 – 2006 **Abitur**
Flatow – Oberschule (Berlin-Köpenick)

Work Experiences

- 11 – 12/2012 **Research Assistant**
Department of Molecular Enzymology – Prof. Dr. K. Tittmann
Georg-August-Universität Göttingen
- 03/2011 – 12/2012 **Student Assistant**
SeqLab - Sequence Laboratories Göttingen GmbH
- 08 – 10/2011 **Student Assistant**
Department of Physical Biochemistry – Prof. Dr. M. V. Rodnina
Max-Planck-Institute for Biophysical Chemistry, Göttingen

Skills

- Scientific skills **Protein and nucleic acid chemistry**
- restriction, ligation, transformation, DNA isolation, PCR, Western Blotting, SDS-PAGE
 - protein expression and purification
 - solid phase peptide synthesis and chemical modifications of peptides
- Chromatography**
- Äkta FPLC (affinity, ion-exchange and size exclusion chromatography)
 - analytical und preparative HPLC
 - LC-MS
- Spectroscopy**
- UV/Vis, fluorescence, circular dichroism
- Calorimetry**
- ITC, DSC
- Kinetics**
- stopped-flow, quenched-flow, laser flash photolysis
- Language skills German (native tongue)
English (fluent)
- IT skills Microsoft Office
Adobe Photoshop, CorelDraw, PyMOL
SigmaPlot, proFit, GraphPad PRISM
ChemDraw, ChemSketch

Scholarships

- 12/2010 **Landesstipendium Niedersachsen 2010**
Award for the bachelor degree

10 Eidesstattliche Erklärung

Hiermit versichere ich, dass ich die Arbeit selbstständig und ohne fremde Hilfe verfasst und keine anderen als die von mir angegebenen Quellen und Hilfsmittel benutzt habe. Die den benutzten Werken wörtlich oder inhaltlich entnommenen Stellen habe ich als solche kenntlich gemacht.

Ich erkläre, keine anderweitigen Promotionsversuche unternommen und die vorliegende Dissertation weder in der jetzigen noch in einer anderen Fassung einer anderen wissenschaftlichen Einrichtung vorgelegt zu haben.

Halle (Saale), 03. Juli 2018

Stefan Wicht